

Thermo-mechanical Modelling and Simulation of Magnesium Alloys during Extrusion Process

Dissertation

**Zur Erlangung des akademischen Grades
Doktor der Ingenieurwissenschaften
(Dr.-Ing.)
der Technischen Fakultät
der Christian-Albrechts-Universität zu Kiel**

Serkan ERTÜRK

Geesthacht

2009

1. Gutachter : Prof. Dr. –Ing. Wolfgang Brocks
2. Gutachter : Prof. Dr. –Ing. Jörn Mosler
Datum der mündlichen Prüfung: 28.09.09

Table of Contents

1. Introduction.....	1
2. Phenomenological Modelling.....	3
2.1. Basic concepts.....	3
2.2. Isotropic yield criteria.....	5
2.2.1. Tresca yield criterion	5
2.2.2. von Mises yield criterion	6
2.3. Anisotropic yield criteria.....	7
2.3.1. Hill's yield criterion of 1948.....	8
2.3.2. Cazacu and Barlat yield criterion.....	8
2.3.3. Modified Cazacu and Barlat yield criterion.....	13
3. Parameter Identification of Yield Loci.....	17
3.1. Introduction.....	17
3.2. Genetic algorithm.....	18
3.3. Constraints on yield loci	18
3.3.1. Mathematical existence.....	18
3.3.2. Convexity.....	19
3.3.3. Evolution.....	20
3.4. Objective function	21
4. Thermomechanical Coupling.....	23
4.1. Introduction.....	23
4.2. Fully coupled temperature-displacement analysis.....	24
4.3. Adiabatic analysis	25
5. Implementation of User Defined Materials-VUMATs	27
5.1. Introduction.....	27
5.2. General characteristics of VUMAT	28
5.3. Implementation of VUMATs	29
5.3.1. VUMAT for adiabatic analysis.....	31
5.3.2. VUMAT for fully coupled analysis	32
5.4. Verifications of VUMATs.....	34
6. Characterisation of Billets: Rate-dependent Yielding	35
6.1. Introduction.....	35
6.2. Experiments.....	35
6.2.1. Temperature measurements	39
6.3. Simulations	41
6.3.1. Material model.....	42
6.3.2. Friction.....	42
6.3.3. Temperature predictions	44
6.3.4. Parameter identifications	50

7. Characterisation of Billets: Anisotropy & Asymmetry	53
7.1. Introduction	53
7.2. Experiments	54
7.2.1. Tensile tests	54
7.2.2. Compression tests	55
7.3. Parameter identifications	56
7.3.1. CaBaPoly4	56
7.3.2. CaBaExpo4ten	57
7.3.3. CaBaExpo2	58
7.3.4. CaBaExpo4	59
7.4. Simulations	62
7.4.1. Tensile tests	62
7.4.2. Compression tests	64
8. Extrusion: Experiments & Simulations	65
8.1. Introduction	65
8.2. Experiments	66
8.3. Simulations	71
8.3.1. Parameter identifications	72
8.3.2. Prediction results.....	74
9. Summary & Conclusion	83
References	87
Appendix	91
A.1. Header of VUMAT interface	91
A.2. Variables used in VUMAT and their descriptions	92
Acknowledgments	93
Curriculum Vitae	95

Table of Figures

Figure 2.1: Yield loci of Tresca and von Mises yield criterion in plane stress.....	6
Figure 2.2: Yield loci with variations of a_k (plane stress condition assumed).....	10
Figure 2.3: Yield loci with variations of b_j (plane stress condition assumed).....	11
Figure 2.4: Yield loci with variation of b_j together with von Mises yield criterion.....	12
Figure 3.1: Examples of wrong (left) and correct (right) evolution of the yield loci.....	21
Figure 5.1: Flowchart of implementation of VUMAT.....	29
Figure 6.1: Experimental matrix performed for each alloy.....	37
Figure 6.2: Experimental results of ZE10 and ZEK100 with variation of strain rates at different temperatures (see Figure 6.1 for the legend).....	38
Figure 6.3: Micrographs of cast billets: left ZE10, right ZEK100.....	39
Figure 6.4: Surface qualities of specimens after compression tests: left ZE10, right ZEK100.....	39
Figure 6.5: Temperature measurements during the experiments (see Figure 6.1 for the legend).....	40
Figure 6.6: FE deformed mesh with superimposed initial geometry.....	41
Figure 6.7: Elastoplastic material inputs used in the simulations.....	42
Figure 6.8: Effect of friction coefficient on barrelling of specimen.....	43
Figure 6.9: Qualitative comparison of barrelling of specimen with deformed mesh.....	43
Figure 6.10: Effect of inelastic heat fraction under adiabatic assumption.....	44
Figure 6.11: Temperature predictions under the assumption of adiabatic heating.....	45
Figure 6.12: Effect of film coefficient used in fully coupled analysis.....	46
Figure 6.13: Temperature predictions with film coefficients defined as a function of time in fully coupled analysis.....	47
Figure 6.14: Temperature predictions with fully coupled analysis.....	47
Figure 6.15: Comparison of temperature predicted by two different approaches.....	48
Figure 6.16: Temperature distributions within the specimens at the end of simulation (adiabatic analysis).....	49
Figure 6.17: Temperature distributions within the specimens at the end of simulation (fully coupled analysis).....	49
Figure 6.18: Comparison of reaction forces obtained by two different approaches.....	50
Figure 6.19: Comparison of simulation results under adiabatic assumption with experiments.....	51
Figure 6.20: Power law parameters in dependence on temperature.....	52
Figure 7.1: Tensile test results: left ZE10, right ZEK100.....	55
Figure 7.2: Compression test results: left ZE10, right ZEK100.....	55
Figure 7.3: Optimised yield loci with parameters labelled as <i>CaBaPoly4</i> for ZEK100.....	57
Figure 7.4: Comparison of the evolution functions: polynomial (left) and exponential functions (right).....	57
Figure 7.5: Optimised yield loci with parameters labelled as <i>CaBaExpo4ten</i> for ZEK100.....	58
Figure 7.6: Optimised yield loci with parameters labelled as <i>CaBaExpo2</i> for ZEK100.....	59
Figure 7.7: Optimised yield loci with parameters labelled as <i>CaBaExpo4</i> for ZE10 (top) and ZEK100 (bottom).....	60
Figure 7.8: Evolution of the parameters: <i>CaBaExpo4</i> for ZE10 (left) and ZEK100 (right).....	61
Figure 7.9: Simulation results of tensile tests performed with <i>CaBaExpo4</i> for ZE10 (top) and ZEK100 (bottom).....	63
Figure 7.10: Simulation results of compression tests performed with <i>CaBaExpo4</i> for ZE10 (top) and ZEK100 (bottom).....	64
Figure 8.1: Experimental results of ZE10 and ZEK100 at different ram speeds.....	67

Figure 8.2: Summary of experimental extrusions for both alloys.....	68
Figure 8.3: Micrographs of profiles obtained by different profile speeds	69
Figure 8.4: Average grain size of profiles obtained by different ram speeds	70
Figure 8.5: Longitudinal section of the extrusion remainder (ZE10) at ram speed of 5 mm/s.....	70
Figure 8.6: FE mesh used in the simulations	71
Figure 8.7: Effect of inelastic heat fractions under adiabatic assumption	73
Figure 8.8: Effect of film coefficients used in fully coupled analysis	74
Figure 8.9: Simulation results with <i>von Mises & CaBaExpo4</i> in comparison with experiments	75
Figure 8.10: Temperature [°C] distributions with <i>CaBaExpo4</i> at profile speeds of 1, 10 and 20 m/min	77
Figure 8.11: von Mises equivalent stress [MPa] distributions ZE10 with <i>CaBaExpo4</i> at profile speeds of 1, 10 and 20 m/min	78
Figure 8.12: Velocity [mm/s] distributions ZEK100 with <i>CaBaExpo4</i> at profile speeds of 1, 10 and 20 m/min	79
Figure 8.13: Flow predictions of ZE10 with <i>CaBaExpo4</i> at profile speed of 20 m/min with the corresponding metallographic examination	80
Figure 8.14: Flow predictions ZEK100 by tracer particles with <i>CaBaExpo4</i> at profile speed of 10 m/min	80
Figure 8.15: Temperature predictions of tracer particles of ZEK100 with <i>CaBaExpo4</i> at profile speed of 10 m/min.....	81

Chapter 1

Introduction

Magnesium alloys have become promising materials saving structural weight and consequently reducing fuel consumption for transportation industry due to being the lightest metal for structural applications (Polmear, 2006). Having various advantages (e.g. homogenous microstructure and higher yield strength) over exclusively used as-cast parts (Kainer, 2003), wrought alloys are more preferable in industry (Bettles and Gibson, 2005). Extrusion is one of the manufacturing methods for semi-finished products supplying this demand. However, wrought magnesium alloys show unusual mechanical properties like deformation anisotropy and different yielding behaviour in tension and compression because of having hexagonal closed packed (hcp) crystal structure (Kaiser et al., 2003) and (Bohlen et al., 2007). This complex plastic behaviour is caused by strong basal texture and presence of deformation twinning (Hosford, 1993), (Barnett, 2007a) and (Barnett, 2007b). Deformation twinning is significant for metals with low-symmetry crystal structures like hcp, in which five independent slip systems necessary for deformation are not easily activated at room temperature. Therefore, ductility and formability of hcp metals are considerably influenced by operable twinning modes (Yoo, 1981). In order to exploit these characteristics in metal forming, an

efficient modelling would be helpful. These phenomena are studied microscopically by crystal plasticity based models (Graff et al., 2007). Models with crystal plasticity such as (Peirce et al., 1983) and (Lebensohn and Tomè, 1993) require detailed information about the deformation mechanisms and texture taking into account the crystallographic orientation of individual grains, thus needing unreasonable computational time for simulations at structural level. To this end, phenomenological modelling suitable for finite element (FE) method was chosen to study the metal flow during extrusion. Unfortunately, commercial FE programmes cannot provide suitable built-in models to capture the phenomena observed in extrusion of magnesium alloys. As a result, user-defined materials, i.e. VUMAT, for commercial FE programme ABAQUS/Explicit, (Abaqus, 2006b), were implemented in this study in order to define proper constitutive equations required for simulations of extrusion of magnesium alloys.

Since extrusion involves complex thermo-mechanical and multiaxial loading conditions resulting in large strains, high strain rates and an increase in temperature due to deformation, a proper yield criterion and hardening law for the description of these processes are needed. The yield criterion proposed by Cazacu and Barlat (Cazacu and Barlat, 2004) captures the phenomena mentioned above. However, the ability of this model is limited because of being derived within the framework of rate-independent plasticity. The effects of strain rate and temperature are pronounced in extrusion and therefore can not be neglected. To this end, Cazacu and Barlat model was modified based on Cowper-Symonds overstress power law (Cowper and Symonds, 1957) and temperature.

The determination of the metal flow in extrusion process for magnesium alloys was aimed with the help of a hybrid method of experiment and simulation. The mechanical tests and extrusion trials were executed in Extrusion Research and Development Centre, TU Berlin. Identification of the model parameters regarding for anisotropy and asymmetry in tension-compression was realised by performing a number of tensile and compression tests on specimens prepared at different orientations with respect to extrusion and transverse directions. In order to describe rate dependent yielding, compression tests were executed at different punch velocities and test temperatures. Simulations of compression tests were performed to fit model parameters by comparing with the corresponding experimental results and then to use as input data for simulations of indirect extrusion trials of cylindrical billets. Although Al-free magnesium alloys, namely ZE10 (Mg+1%Zn+1%Ce) and ZEK100 (Mg+1%Zn+1%Ce+0.3%Zr), were selected in this study, the method discussed here for describing the material behaviour during extrusion process may be extended to be applicable to other magnesium alloys or even other metals with hcp crystal structure.

Chapter 2

Phenomenological Modelling

2.1. Basic concepts

For a uniaxial stress state it is easy to define the limit above which the material undergoes irreversible (plastic) deformation. The respective quantity, known as yield stress in tension, is usually determined by means of a (uniaxial) tensile test. However, this can not be extended to the case of arbitrary (multiaxial) loading occurring during manufacturing or in service. To this end, a yield criterion is needed to define the transition from elastic to plastic states of deformation. The mathematical expression of a yield criterion is called yield function, f , which defines a surface in the stress space. This surface separating elastic and plastic deformations is called yield surface. Stress states with $f < 0$ represent elastic behaviour. As described in Drucker's stability postulates (Drucker, 1964), any yield surface is assumed as convex since any straight path between two elastic states must not result in plastic deformation. Stress states satisfying $f = 0$ may cause plastic deformation. In the framework of rate-independent plasticity, stress states with

$f > 0$ are inadmissible. On the other hand, the condition, $f > 0$, exists in the case of rate-dependent plasticity resulting in the stress states which may lie outside the yield surface.

The yield function must be invariant with respect to the choice of the reference frame. As a result, yield functions are generally formulated as a function of the stress invariants. Most metals including magnesium and its alloys are insensitive to the hydrostatic stress, σ_h , defined as

$$\sigma_h = \frac{1}{3} I_1, \quad (2.1)$$

where I_1 is the first invariant of the Cauchy stress tensor calculated as trace of the stress tensor, i.e. $I_1 = \sigma_{xx} + \sigma_{yy} + \sigma_{zz}$. Since yielding is independent of the hydrostatic stress for such materials, the yield function of pressure insensitive materials is written as a function of deviatoric stresses defined as

$$\underline{\sigma}' = \underline{\sigma} - \sigma_h \underline{I}, \quad (2.2)$$

with the unit tensor, \underline{I} .

The trace of the deviatoric stress tensor, i.e. J_1 , is zero. J_2 , namely the second invariant of deviatoric stress, is defined in terms of stress components as

$$J_2 = \frac{1}{6} [(\sigma_{xx} - \sigma_{yy})^2 + (\sigma_{yy} - \sigma_{zz})^2 + (\sigma_{zz} - \sigma_{xx})^2] + \sigma_{xy}^2 + \sigma_{yz}^2 + \sigma_{xz}^2, \quad (2.3)$$

and the third invariant, J_3 , is the determinant of the deviatoric stress tensor.

In order to complete the description of plastic behaviour of a material, a flow rule linking stress and plastic strain components is essential. This constitutive law of plastic deformation is commonly for most metals associated, which means that the yield function is taken as plastic potential. The flow rule is then expressed as

$$\dot{\varepsilon}_{ij}^p = \dot{\lambda} \frac{\partial f}{\partial \sigma_{ij}}, \quad (2.4)$$

where $\dot{\varepsilon}_{ij}^p$ is the plastic strain rate tensor and $\dot{\lambda}$ is a scalar plastic multiplier. Since all the plastic strain rate components are normal to the yield surface, this flow rule is also called normality rule, which is another consequence of Drucker's stability postulate.

A hardening law describes changes of the yield function during deformation. Therefore, the yield function is defined by scalar or tensorial internal variables to capture proper evolution of the yield surface during deformation. For perfectly plastic materials, which present no hardening behaviour, the initial yield function is unchanged in the stress space during plastic deformation. Nevertheless, metals in most cases harden as plastic strain increases (i.e. strain hardening). The strain hardening observed in metals is generally categorised as isotropic, kinematic, or a combination of both (mixed hardening). Isotropic hardening assumes uniform expansion without translation of the yield surface in the stress space, unlike kinematic hardening in which translation without expansion is assumed during plastic deformation. However, the shape of yield surfaces remains unchanged in both isotropic and kinematic hardening.

2.2. Isotropic yield criteria

Isotropic materials show uniformity of mechanical characteristics in all directions. Any isotropic yield criterion is, consequently, defined as a function of stress tensor invariants. Yield criteria for isotropic metals derived by (Tresca, 1864), (von Mises, 1928) and (Hosford, 1972) are the examples found in literature. In this section, two commonly used yield criteria for isotropic metals, namely Tresca and von Mises yield criteria, are presented.

2.2.1. Tresca yield criterion

The first formulated yield condition was proposed by Tresca assuming that the plastic deformation will occur when the maximum shear stress reaches a critical value, τ_y . This criterion is written as a function of principal stresses, σ_1 , σ_2 and σ_3 , as

$$\max\left(\left|\frac{\sigma_1 - \sigma_2}{2}\right|, \left|\frac{\sigma_2 - \sigma_3}{2}\right|, \left|\frac{\sigma_3 - \sigma_1}{2}\right|\right) - \tau_y = 0, \quad (2.5)$$

where τ_y is the yield stress obtained from a simple shear test. According to Tresca's yield criterion, the shear strength in pure shear is half of that in uniaxial tension, σ_y .

The Tresca yield criterion is proper for isotropic material because of the presence of maximum and absolute functions in its formulation as seen in Equation (2.5). The Tresca yield surface is a hexagonal cylinder in the principal stress space, whereas it is a hexagon in plane stress (see Figure 2.1).

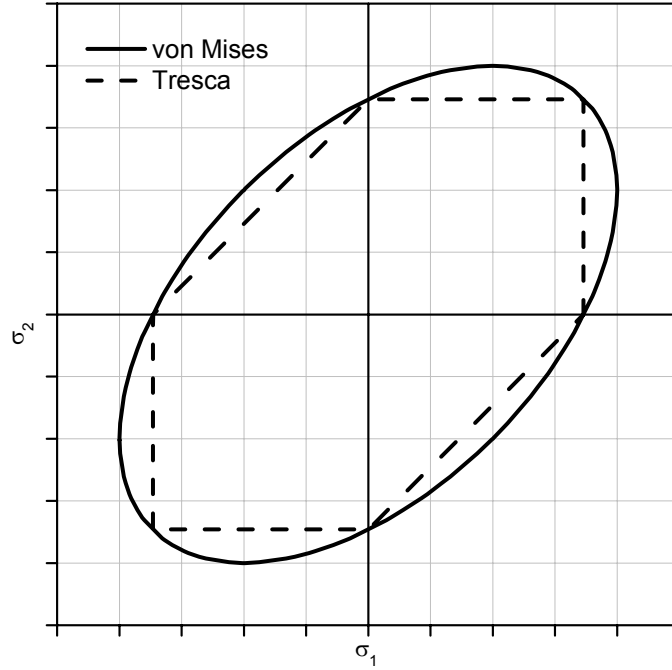


Figure 2.1: Yield loci of Tresca and von Mises yield criterion in plane stress

Besides the expression in terms of principal stresses, this yield criterion is also written in terms of second and third invariants (Burth and Brocks, 1992) as

$$4J_2^3 - 27J_3^2 - 9\sigma_y^2 J_2^2 + 6\sigma_y^4 J_2^2 - \sigma_y^6 = 0. \quad (2.6)$$

As seen in Equation (2.6), the yield function does not depend on the trace of stress tensor, I_1 , so it is insensitive to hydrostatic pressure.

2.2.2. von Mises yield criterion

Close fit to experimental data for most metals with face-centred cubic and body-centred cubic structures can often be obtained with von Mises yield criterion, in which the second invariant of the deviatoric stress tensor, J_2 , is assumed to solely determine yielding as

$$3J_2 - \sigma_y^2 = 0, \quad (2.7)$$

where σ_y is the uniaxial yield stress.

The von Mises yield criterion is also expressed as

$$\bar{\sigma}^2 - \sigma_y^2 = 0, \quad (2.8)$$

with the von Mises equivalent stress, $\bar{\sigma} = \sqrt{3J_2}$. The principle of equivalence of plastic work (or dissipation) rate, i.e. $\dot{W}^p = \sigma_{ij}\dot{\epsilon}_{ij}^{pl} = \bar{\sigma}\dot{\bar{\epsilon}}^{pl}$, provides the definition of the equivalent plastic strain rate as

$$\dot{\bar{\epsilon}}^{pl} = \sqrt{\frac{2}{3}\dot{\epsilon}_{ij}^{pl}\dot{\epsilon}_{ij}^{pl}}. \quad (2.9)$$

As Tresca's yield criterion, the von Mises yield criterion implies for isotropic behaviour by giving equal weight to the three principal stresses, namely σ_1 , σ_2 and σ_3 . When plotted in the three dimensional space of the principal stresses, the von Mises yield surface appears as a cylinder oriented collinear to the hydrostatic axis, i.e. $\sigma_1 = \sigma_2 = \sigma_3$, due to the rotational symmetry. The section $\sigma_3 = 0$ of the von Mises yield locus gives an ellipse centred in the origin with major axes inclined at 45° to the σ_1 axis as seen Figure 2.1.

2.3. Anisotropic yield criteria

Unlike isotropic yield criteria for which the choice of a reference frame is arbitrary, anisotropic yield criteria must be expressed in a fixed system since anisotropy means the dependence of material properties on the testing direction.

Anisotropic criteria such as (Hill, 1948), (Hill, 1990), (Barlat et al., 1991), (Barlat et al., 1997), (Bron and Besson, 2004) and (Karafillis and Boyce, 1993) exist in the literature. However, these criteria are represented by even functions of stress and thus cannot capture tension/compression asymmetry. Therefore, they intended to model cubic metals. The third invariant, J_3 , characterises deviations from rotational symmetry. The most popular of yield criteria including the third invariant is Tresca's yield criterion which holds only for isotropic materials with tension/compression symmetry due to its dependency on J_3 quadratically as seen in Equation (2.6). The yield criterion proposed by Cazacu and Barlat (Cazacu and Barlat, 2004) captures tension/compression asymmetry observed in hcp metals. It modifies the von Mises yield potential by introducing the third invariant of the stress tensor within the framework of rate-independent plasticity. Drucker's yield condition (Drucker, 1949), which lies between the bounds defined by the von Mises and Tresca yield criteria having a structure of $J_2^3 - cJ_3^2$, is extended in their study by using the generalisation of invariants to orthotropy. Since (Hill, 1948) as a pioneer study

exploited the generalisation, it is presented here firstly, and then, Cazacu and Barlat model is discussed.

However, the yield criteria mentioned above were derived without any consideration of rate effects. In order to include effects of the loading rate into the modelling, rate-dependent yielding was considered due to its importance in metal forming. A large number of formulations in literature can be found such as Johnson-Cook models (Johnson and Cook, 1983; Johnson and Cook, 1985) and Steinberg`s models (Steinberg et al., 1980; Steinberg and Lund, 1989). Cowper-Symonds overstress power law (Cowper and Symonds, 1957) was chosen due to being available in ABAQUS (Abaqus, 2006a) in combination with the von Mises yield criterion. Besides this easiness in verification, it has reasonable model parameters unlike other rate-dependent yielding models. A modified version of the Cazacu and Barlat model with respect to strain rate and temperature dependency of plastic deformation is proposed and described.

2.3.1. Hill`s yield criterion of 1948

The yield criterion proposed by von Mises is extended by using the generalisation of invariants to orthotropy. Hill proposed the following quadratic yield criterion, as given in Equation (2.8),

$$\bar{\sigma}^2 - \sigma_y^2 = 0, \quad (2.10)$$

for orthotropic materials with an equivalent stress defined as:

$$\bar{\sigma}^2 = 3J_2^\circ = \frac{1}{2}[a_1(\sigma_{xx} - \sigma_{yy})^2 + a_2(\sigma_{yy} - \sigma_{zz})^2 + a_3(\sigma_{zz} - \sigma_{xx})^2] + 3(a_4\sigma_{xy} + a_5\sigma_{yz} + a_6\sigma_{xz}), \quad (2.11)$$

where (x, y, z) are the orthotropy axes.

2.3.2. Cazacu and Barlat yield criterion

The phenomenological model proposed by Cazacu and Barlat captures asymmetry in yielding in pressure-insensitive metals. Cazacu and Barlat considered generalisations of the second and third deviator invariants, J_2 and J_3 . The proposed anisotropic and asymmetric yield criterion is given by

$$f = (\sqrt{J_2^\circ})^3 - J_3^\circ - \tau_y^3, \quad (2.12)$$

where τ_y is the yield strength in shear.

The generalisation of J_2 to orthotropy, denoted by J_2° is expressed in the reference frame associated to the material symmetry as

$$J_2^\circ = \frac{a_1}{6}(\sigma_{xx} - \sigma_{yy})^2 + \frac{a_2}{6}(\sigma_{yy} - \sigma_{zz})^2 + \frac{a_3}{6}(\sigma_{zz} - \sigma_{xx})^2 + a_4\sigma_{xy}^2 + a_5\sigma_{xz}^2 + a_6\sigma_{yz}^2, \quad (2.13)$$

which is the same formulation derived by Hill as in Equation (2.11).

If all the coefficients a_k are set to unity, J_2° reduces to J_2 ,

$$a_k (k = 1, \dots, 6) = 1 \quad \rightarrow \quad J_2^\circ = J_2. \quad (2.14)$$

The generalisation with respect to orthotropy of J_3 , denoted by J_3° , is expressed as

$$\begin{aligned} J_3^\circ = & \frac{1}{27}(b_1 + b_2)\sigma_{xx}^3 + \frac{1}{27}(b_3 + b_4)\sigma_{yy}^3 + \frac{1}{27}[2(b_1 + b_4) - b_2 - b_3]\sigma_{zz}^3 \\ & + 2b_{11}\sigma_{xy}\sigma_{xz}\sigma_{yz} + \frac{2}{9}(b_1 + b_4)\sigma_{xx}\sigma_{yy}\sigma_{zz} - \frac{1}{9}(b_1\sigma_{yy} + b_2\sigma_{zz})\sigma_{xx}^2 \\ & - \frac{1}{9}(b_3\sigma_{zz} + b_4\sigma_{xx})\sigma_{yy}^2 - \frac{1}{9}[(b_1 - b_2 + b_4)\sigma_{xx} + (b_1 - b_3 + b_4)\sigma_{yy}]\sigma_{zz}^2 \\ & - \frac{\sigma_{yz}^2}{3}[(b_6 + b_7)\sigma_{xx} - b_6\sigma_{yy} - b_7\sigma_{zz}] \\ & - \frac{\sigma_{xz}^2}{3}[2b_9\sigma_{yy} - b_8\sigma_{zz} - (2b_9 - b_8)\sigma_{xx}] \\ & - \frac{\sigma_{xy}^2}{3}[2b_{10}\sigma_{zz} - b_5\sigma_{yy} - (2b_{10} - b_5)\sigma_{xx}], \end{aligned} \quad (2.15)$$

where all the coefficients b_j reduce to unity for isotropic conditions,

$$b_j (j = 1, \dots, 11) = 1 \quad \rightarrow \quad J_3^\circ = J_3. \quad (2.16)$$

In the case of plane stress, the corresponding yield function contains 10 parameters. The generalised stress invariants are written as

$$J_2^\circ = \frac{1}{6}(a_1 + a_3)\sigma_{xx}^2 - \frac{a_1}{3}\sigma_{xx}\sigma_{yy} + \frac{1}{6}(a_1 + a_2)\sigma_{yy}^2 + a_4\sigma_{xy}^2 \quad (2.17)$$

and

$$\begin{aligned} J_3^\circ = & \frac{1}{27}(b_1 + b_2)\sigma_{xx}^3 + \frac{1}{27}(b_3 + b_4)\sigma_{yy}^3 \\ & - \frac{1}{9}(b_1\sigma_{xx} + b_4\sigma_{yy})\sigma_{xx}\sigma_{yy} - \frac{\sigma_{xy}^2}{3}[-b_5\sigma_{yy} - (2b_{10} - b_5)\sigma_{xx}] \end{aligned} \quad (2.18)$$

By neglecting the effect of shear component, i.e. σ_{xy} , the number of parameters is reduced further to 7 consisting of $a_1, a_2, a_3, b_1, b_2, b_3$ and b_4 , namely. The shape of the yield surface is determined by the parameters. The effect of a_k and b_j on the yield loci can be captured from Figure 2.2 and Figure 2.3, respectively.

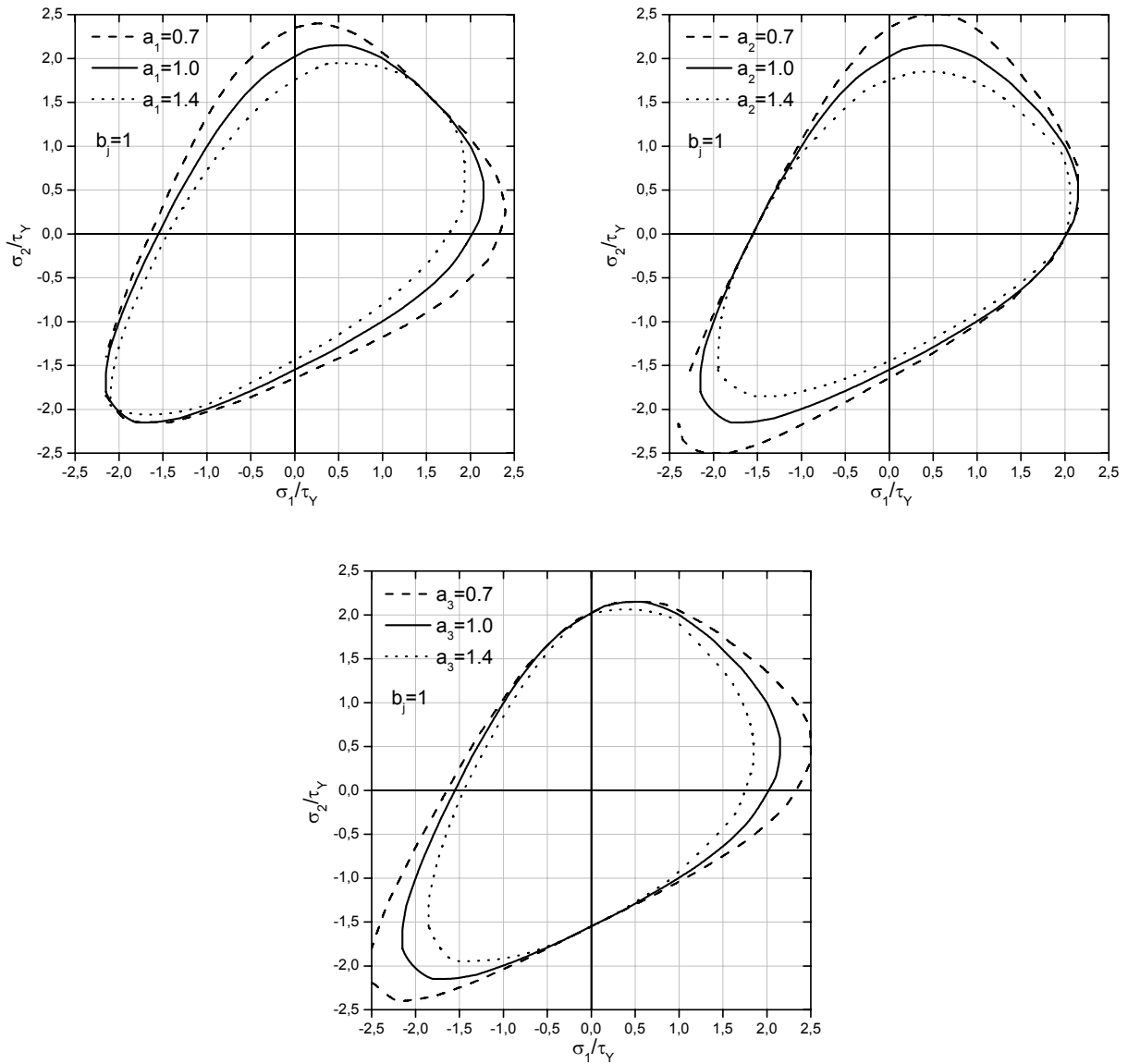


Figure 2.2: Yield loci with variations of a_k (plane stress condition assumed)

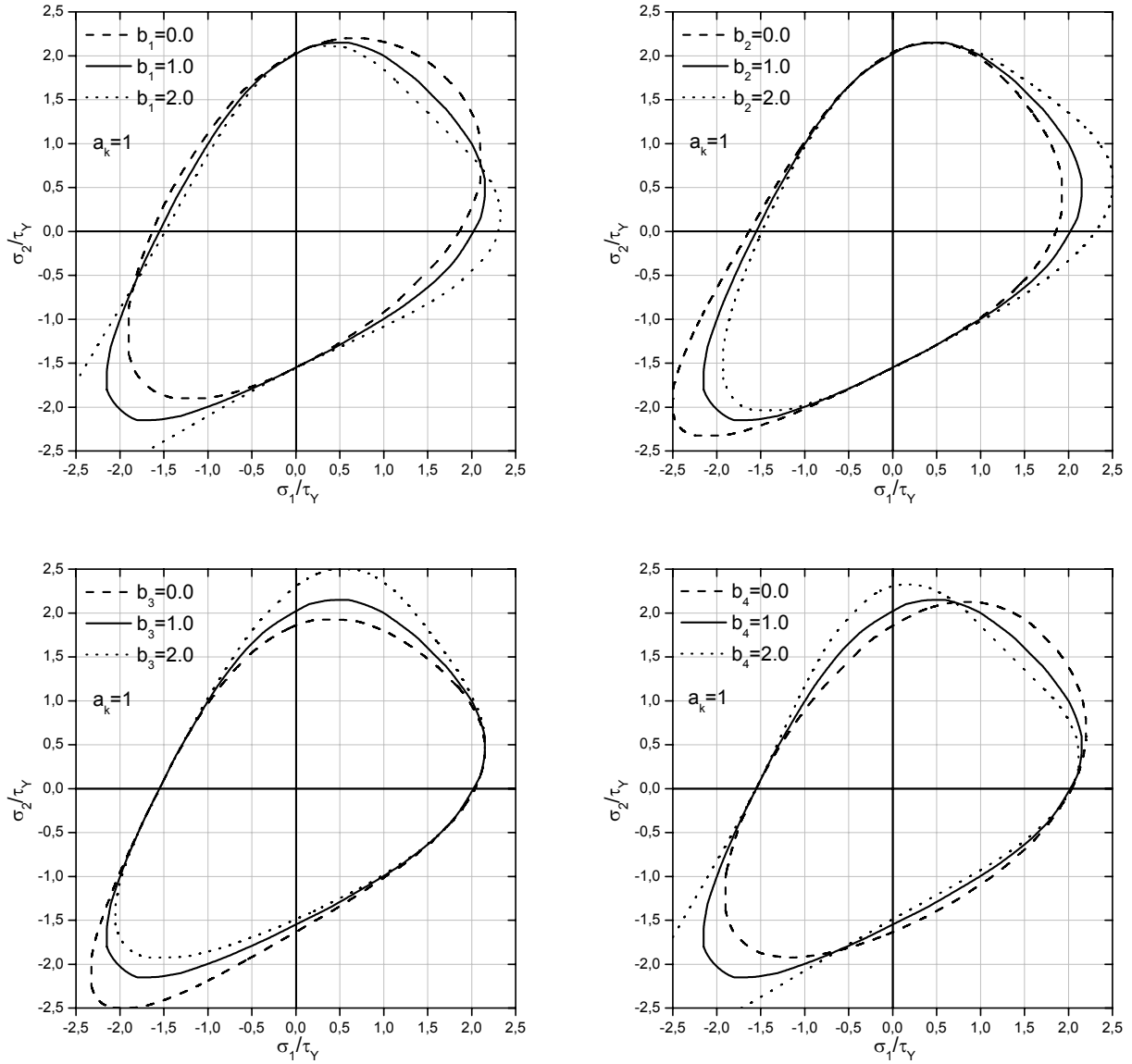


Figure 2.3: Yield loci with variations of b_j (plane stress condition assumed)

Since the Cazacu and Barlat yield criterion is an extension of von Mises yield criterion, one can mimic conventional von Mises plasticity by choosing the model parameters as:

$$\begin{aligned}
 a_k (k = 1, \dots, 6) &= 1, \\
 b_j (j = 1, \dots, 11) &= 0.
 \end{aligned}
 \tag{2.19}$$

Figure 2.4 illustrates the comparison of yield loci with different set of b_j and von Mises yield locus.

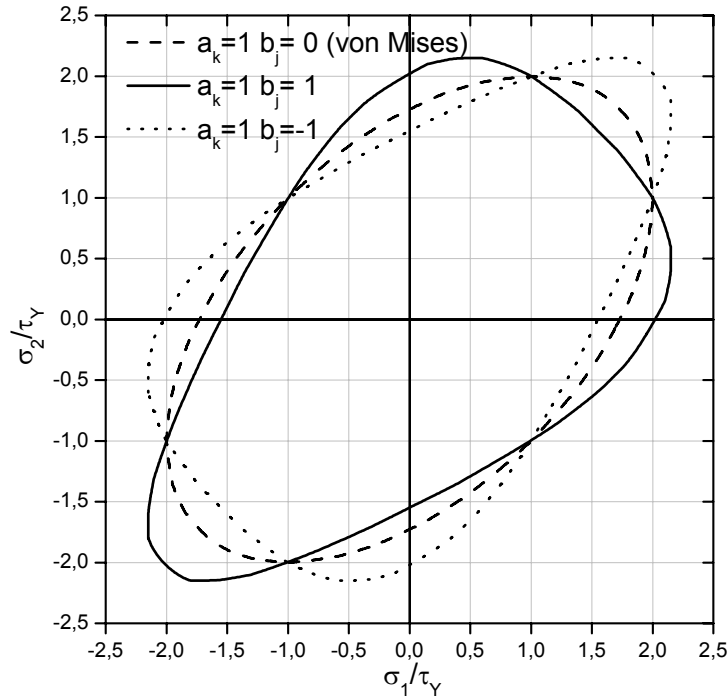


Figure 2.4: Yield loci with variation of b_j together with von Mises yield criterion

A special class of orthotropic materials are those that have the same properties in one plane and different properties in the direction normal to this plane. Such materials are called transverse isotropic and they are described by an axisymmetric formulation. The generalised stress invariant is written as

$$J_2^\circ = \frac{a_1}{6} [(\sigma_{xx} - \sigma_{yy})^2 + (\sigma_{yy} - \sigma_{zz})^2] + \frac{a_3}{6} (\sigma_{zz} - \sigma_{xx})^2 + a_4 (\sigma_{xy}^2 + \sigma_{yz}^2) + a_6 \sigma_{xz}^2 \quad (2.20)$$

with the conditions:

$$a_1 = a_2$$

and

$$(2.21)$$

$$a_4 = a_5.$$

The third invariant is written as

$$\begin{aligned} J_3^\circ = & \frac{1}{27} (b_1 + b_2) (\sigma_{xx}^3 + \sigma_{zz}^3) + \frac{2}{27} (2b_2 - b_1) \sigma_{yy}^3 + \frac{4}{9} b_1 \sigma_{xx} \sigma_{yy} \sigma_{zz} \\ & - \frac{1}{9} b_1 \sigma_{yy} (\sigma_{xx}^2 + \sigma_{zz}^2) + \frac{1}{9} b_2 (\sigma_{zz} \sigma_{xx}^2 + \sigma_{xx} \sigma_{zz}^2) - \frac{1}{9} (2b_2 - b_1) (\sigma_{xx} + \sigma_{zz}) \sigma_{yy}^2 \\ & + \left[\left(-\frac{1}{6} b_5 (\sigma_{xy}^2 + \sigma_{yz}^2) + \frac{1}{3} b_8 \right) \sigma_{xz}^2 \right] (\sigma_{xx} - 2\sigma_{yy} + \sigma_{zz}) + 2b_{11} \sigma_{xy} \sigma_{yz} \sigma_{xz} \quad , \end{aligned} \quad (2.22)$$

by applying the conditions:

$$\begin{aligned}
b_3 &= b_4 = 2b_2 - b_1, \\
b_5 &= b_6, \\
b_7 &= -b_5 / 2, \\
b_8 &= b_9
\end{aligned} \tag{2.23}$$

and

$$b_{10} = b_5 / 4 = (b_5 + b_7) / 2.$$

Since the conditions, $\sigma_{xz} = 0$ and $\sigma_{xy} = \sigma_{yz}$, are applicable to the axisymmetric formulation, the invariants become

$$J_2^\circ = \frac{a_1}{6} [(\sigma_{xx} - \sigma_{yy})^2 + (\sigma_{yy} - \sigma_{zz})^2] + \frac{a_3}{6} (\sigma_{zz} - \sigma_{xx})^2 + 2a_4 \sigma_{xy}^2 \tag{2.24}$$

and

$$\begin{aligned}
J_3^\circ &= \frac{1}{27} (b_1 + b_2) (\sigma_{xx}^3 + \sigma_{zz}^3) + \frac{2}{27} (2b_2 - b_1) \sigma_{yy}^3 + \frac{4}{9} b_1 \sigma_{xx} \sigma_{yy} \sigma_{zz} \\
&- \frac{1}{9} b_1 \sigma_{yy} (\sigma_{xx}^2 + \sigma_{zz}^2) + \frac{1}{9} b_2 (\sigma_{zz} \sigma_{xx}^2 + \sigma_{xx} \sigma_{zz}^2) - \frac{1}{9} (2b_2 - b_1) (\sigma_{xx} + \sigma_{zz}) \sigma_{yy}^2 \\
&- \frac{1}{3} b_5 \sigma_{xy}^2 (\sigma_{xx} - 2\sigma_{yy} + \sigma_{zz}) .
\end{aligned} \tag{2.25}$$

As a result, the corresponding yield function for axisymmetric formulation contains 6 parameters, namely a_1, a_3, a_4, b_1, b_2 and b_5 .

2.3.3. Modified Cazacu and Barlat yield criterion

As mentioned before, in the original work of Cazacu and Barlat, neither strain-rate dependency nor temperature dependency is considered. In order to capture these phenomena, the proposed modified version of the yield function is written as a function of three internal state variables, namely: equivalent plastic strain, $\bar{\varepsilon}^{pl}$, plastic strain rate, $\dot{\bar{\varepsilon}}^{pl}$, and temperature, θ , (Ertürk et al., 2008; Ertürk et al., 2009),

$$f = \left(J_2^\circ(\bar{\varepsilon}^{pl}) \right)^{3/2} - J_3^\circ(\bar{\varepsilon}^{pl}) - \tau_y^3(\bar{\varepsilon}^{pl}, \dot{\bar{\varepsilon}}^{pl}, \theta). \tag{2.26}$$

In order to capture proper hardening observed in magnesium alloys, the coefficients, a_k and b_j , are defined as functions of the equivalent plastic strain, $\bar{\varepsilon}^{pl}$. Since the associated flow rule (see Equation (2.4) for the general definition) of Cazacu and Barlat model is very complicated, the

definition of equivalent plastic strain in Equation (2.9) is assumed. The identification of the parameters for initial and subsequent yield surfaces are performed with the help of optimisation algorithm and the evolutions of the parameters is discussed in details later in *Chapter 3*.

As seen in Equation (2.27), the yield strength in shear, τ_y , is expressed by the yield strength, σ_y , as measured from the uniaxial tensile test,

$$\tau_y = \left(\left(\frac{1}{6}(a_1 + a_3) \right)^{3/2} - \frac{1}{27}(b_1 + b_2) \right)^{1/3} \sigma_y. \quad (2.27)$$

On the other hand, if the stress tensor is adapted to a uniaxial compression test, where only one non-zero component in compression exists, τ_y is obtained by the following expression:

$$\tau_y = \left(\left(\frac{1}{6}(a_1 + a_3) \right)^{3/2} + \frac{1}{27}(b_1 + b_2) \right)^{1/3} \sigma_y. \quad (2.28)$$

σ_y is defined multiplicatively by considering three phenomena, namely strain hardening, $\sigma_y(\bar{\varepsilon}^{pl})$, strain rate hardening via overstress, $f_{RD}(\dot{\bar{\varepsilon}}^{pl})$, and softening due to dissipation, $f_{TD}(\theta)$, as $\sigma_y = \sigma_y(\bar{\varepsilon}^{pl})f_{RD}(\dot{\bar{\varepsilon}}^{pl})f_{TD}(\theta)$.

The strain hardening part of the yield stress is defined as

$$\sigma_y(\bar{\varepsilon}^{pl}) = \sigma_o + H(\bar{\varepsilon}^{pl})\bar{\varepsilon}^{pl}, \quad (2.29)$$

where σ_o is initial yield strength and H is hardening modulus defined as

$$H = \frac{\partial \sigma_y}{\partial \bar{\varepsilon}^{pl}}. \quad (2.30)$$

The yield stress under quasi-static conditions is linked to a “dynamic” yield stress via 2 model parameters: D and n as described in Cowper-Symonds overstress power law (Cowper and Symonds, 1957). The model parameters, D and n , are defined with respect to temperature in order to take any influence of temperature on rate dependency into account:

$$f_{RD}(\dot{\bar{\varepsilon}}^{pl}) = \left[\left(\frac{\dot{\bar{\varepsilon}}^{pl}}{D(\theta)} \right)^{1/n(\theta)} + 1 \right]. \quad (2.31)$$

The pair of D and n at different temperatures is calculated by interpolation of the known values. This methodology is extended in the case of the yield stresses at different temperatures, as well in order to capture softening, i.e. $f_{TD}(\theta)$. The temperature calculation is handled in *Chapter 4*.

Chapter 3

Parameter Identification of Yield Loci

3.1. Introduction

In many industrial applications, empirical or physical models involving some unknown parameters are used for design or simulation purposes. The identification of the model parameters is obtained by using either Trial-and-Error method or an optimisation method being the act of obtaining the best result under the given circumstances. Trial-and-Error method is suitable when the model is simple and the number of unknown parameters is reasonable. Optimisation method is, however, used when the model is complex and a huge number of unknown parameters is concerned.

As described before, Cazacu and Barlat yield criterion contains 17 model parameters. With further assumptions described later, the number of parameters is reduced to 7. However, this reduction is not sufficient to handle the parameters with a Trial-and-Error method. To this end, an optimisation algorithm based on genetic algorithm described in (Hossain, 2007) was adopted and modified in this study. If the model parameters generated by genetic algorithm satisfy the constraints described

later, the set of model parameters is accepted and the objective function expressed later is then evaluated. The parameter set having the minimum value will be the optimised solution.

3.2. Genetic algorithm

Genetic algorithm, (Schwefel, 1977) (Holland, 1992) (Rechenberg, 1994), is well suited for solving adaptive problems because of the capacity to evolve and adjust to changing environments. Genetic algorithm performs a stochastic evolution process toward global optimisation through the use of crossover and mutation operators. The search space of the problem is represented as a collection of parameter sets, which are referred as chromosomes. The quality of a chromosome is measured by a fitness function that ranks the optimality of a solution in genetic algorithm. After initialisation, each generation produces new children based on the crossover and mutation operators. The process terminates when several consecutive generations do not produce noticeable population fitness improvement or reach the maximum number of prescribed generation.

3.3. Constraints on yield loci

A set of constraints, which allow the unknowns to take on certain values but exclude others, is presented here. Since the constraints limit the search space, they are essential to find the variables which minimise the objective function.

3.3.1. Mathematical existence

Due to the symmetry of profiles manufactured in extrusion trials, transverse isotropic material behaviour is assumed and the representative mesh is generated with axisymmetric continuum elements (see *Chapter 8*). The corresponding yield function is composed of the stress invariants expressed in Equations (2.20) and (2.22). However, it is not possible to identify the parameters with the help of experimental data from tensile and compression tests which do not provide any information about the conditions given in Equations (2.21) and (2.23). The experimental results and the corresponding parameter identifications are described later in *Chapter 7*. To this end, the generalised stress invariants expressed in Equations (2.17) and (2.18) are assumed and then rewritten as

$$J_2^o = \frac{1}{6}(a_1 + a_3)\sigma_L^2 - \frac{a_1}{3}\sigma_L\sigma_T + \frac{1}{6}(a_1 + a_2)\sigma_T^2 \quad (3.1)$$

and

$$J_3^\circ = \frac{1}{27}(b_1 + b_2)\sigma_L^3 + \frac{1}{27}(b_3 + b_4)\sigma_T^3 - \frac{1}{9}(b_1\sigma_L + b_4\sigma_T)\sigma_L\sigma_T, \quad (3.2)$$

where L and T refer the longitudinal and transverse directions, respectively.

The yield strength in shear, τ_y , is assumed as a positive function increasing with plastic strain. As a result, the following condition has to be satisfied for mathematical existence,

$$\tau_y = ((\sqrt{J_2^\circ})^3 - J_3^\circ)^{1/3} \geq 0, \quad (3.3)$$

and thus

$$(\sqrt{J_2^\circ})^3 - J_3^\circ \geq 0, \quad (3.4)$$

which requires

$$J_2^\circ = \frac{1}{6}(a_1 + a_3)\sigma_L^2 - \frac{a_1}{3}\sigma_L\sigma_T + \frac{1}{6}(a_1 + a_2)\sigma_T^2 \geq 0. \quad (3.5)$$

3.3.2. Convexity

In order to ensure convexity of the yield surface, the Hessian matrix of the yield function must be positive semi-definite with respect to the principal stresses (Rockafellar, 1972), which can be ensured by having non-negative eigenvalues. The Hessian, \underline{H} , of a function $g(x_1, x_2, \dots, x_n)$ is defined generally as the derivatives of the Jacobian matrix with respect to its components, x_1, x_2, \dots, x_n . The yield surface is a function of the principal stresses, σ_L and σ_T along longitudinal, L , and transverse, T , directions. Therefore, the Hessian matrix becomes

$$\underline{H} = \begin{pmatrix} \frac{\partial^2 f}{\partial \sigma_L^2} & \frac{\partial^2 f}{\partial \sigma_L \partial \sigma_T} \\ \frac{\partial^2 f}{\partial \sigma_T \partial \sigma_L} & \frac{\partial^2 f}{\partial \sigma_T^2} \end{pmatrix}. \quad (3.6)$$

The components of \underline{H} are calculated as following:

$$H_{11} = -\frac{2}{9}(b_1 + b_2)\sigma_L + \frac{2}{9}b_1\sigma_T + \frac{3\left(\frac{a_3}{3}\sigma_T + \frac{a_1}{3}(\sigma_L - \sigma_T)\right)^2}{4\sqrt{\frac{a_3}{6}\sigma_L^2 + \frac{a_1}{6}(\sigma_L - \sigma_T)^2 + \frac{a_2}{6}\sigma_T^2}}, \quad (3.7)$$

$$H_{22} = \frac{2}{9}b_4\sigma_L - \frac{2}{9}(b_3 + b_4)\sigma_T + \frac{3\left(\frac{a_3}{3}\sigma_T + \frac{a_1}{3}(\sigma_L - \sigma_T)\right)^2}{4\sqrt{\frac{a_3}{6}\sigma_L^2 + \frac{a_1}{6}(\sigma_L - \sigma_T)^2 + \frac{a_2}{6}\sigma_T^2}}, \quad (3.8)$$

$$+ \frac{1}{2}(a_1 + a_2)\sqrt{\frac{a_3}{6}\sigma_L^2 + \frac{a_1}{6}(\sigma_L - \sigma_T)^2 + \frac{a_2}{6}\sigma_T^2}$$

$$H_{12} = H_{21} = \frac{2}{9}b_1\sigma_L + \frac{2}{9}b_4\sigma_T + \frac{a_3 + \frac{a_1}{3}(\sigma_L - \sigma_T)\left(\frac{a_2}{3}\sigma_T - \frac{a_1}{3}(\sigma_L - \sigma_T)\right)}{4\sqrt{\frac{a_3}{6}\sigma_L^2 + \frac{a_1}{6}(\sigma_L - \sigma_T)^2 + \frac{a_2}{6}\sigma_T^2}}. \quad (3.9)$$

$$+ \frac{a_1}{2}\sqrt{\frac{a_3}{6}\sigma_L^2 + \frac{a_1}{6}(\sigma_L - \sigma_T)^2 + \frac{a_2}{6}\sigma_T^2}$$

To ensure the existence of each component of \underline{H} , the following condition must be fulfilled,

$$\frac{a_3}{6}\sigma_L^2 + \frac{a_1}{6}(\sigma_L - \sigma_T)^2 + \frac{a_2}{6}\sigma_T^2 \geq 0. \quad (3.10)$$

The eigenvalues $\lambda_{1,2}$ of \underline{H} are calculated as

$$\lambda_{1,2} = \frac{1}{2}\left((H_{11} + H_{22}) \pm \sqrt{(H_{11} + H_{22})^2 + 4(H_{11}H_{22} - H_{12}^2)}\right). \quad (3.11)$$

The existence of the real valued eigenvalues $\lambda_{1,2}$ is, hence, ensured by the following condition,

$$(H_{11} + H_{22})^2 + 4(H_{11}H_{22} - H_{12}^2) \geq 0. \quad (3.12)$$

3.3.3. Evolution

Yield loci of a hardening material are usually displayed as isocontours of the plastic equivalent strain or plastic work called as isostrain or isowork, respectively, which is expressed as the area under the stress-plastic strain curve. The yield loci at different plastic equivalent strains for all loading paths are supposed to evolve without intersecting themselves as seen in Figure 3.1. Therefore, an arbitrary yield locus defined for any given value of the equivalent plastic strain, $\bar{\epsilon}_n^{pl}$, must be entirely inside the yield locus defined for another value of the plastic strain, $\bar{\epsilon}_{n+1}^{pl}$, which is greater than $\bar{\epsilon}_n^{pl}$.

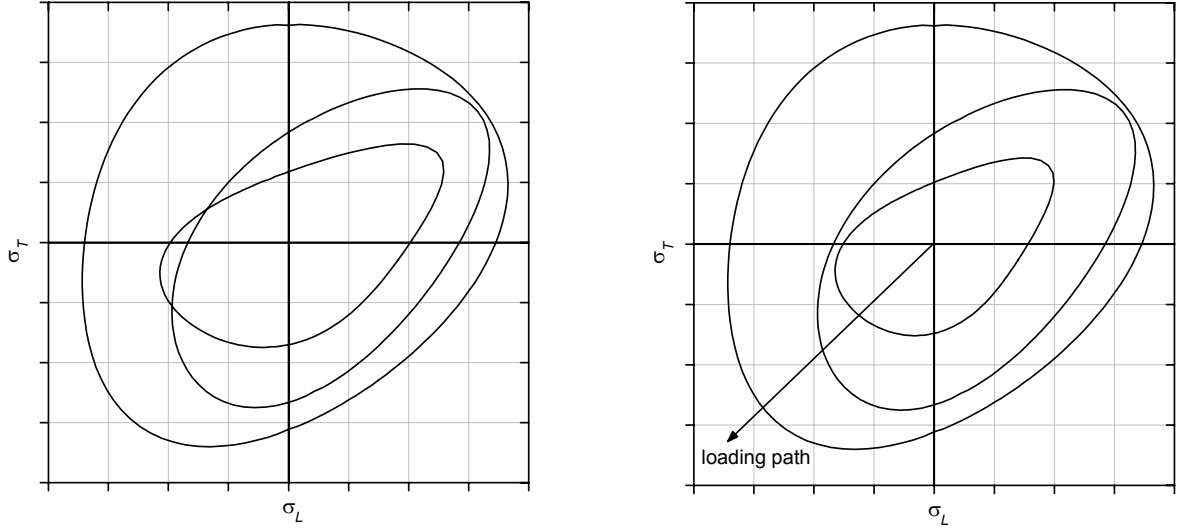


Figure 3.1: Examples of wrong (left) and correct (right) evolution of the yield loci

The following two functions, namely exponential and polynomial, were selected to capture the evolution of the parameters with respect to equivalent plastic strain. The evolution of coefficients is written as exponential function

$$a_i (i = 1, 2, 3) = A_i + B_i (1 - \exp(-C_i \bar{\epsilon}^{pl})), \quad (3.13)$$

$$b_i (i = 1, 2, 3, 4) = A_i + B_i (1 - \exp(-C_i \bar{\epsilon}^{pl}))$$

or as second-order polynomial function

$$a_i (i = 1, 2, 3) = A_i (\bar{\epsilon}^{pl})^2 + B_i \bar{\epsilon}^{pl} + C_i, \quad (3.14)$$

$$b_i (i = 1, 2, 3, 4) = A_i (\bar{\epsilon}^{pl})^2 + B_i \bar{\epsilon}^{pl} + C_i.$$

3.4. Objective function

As mentioned before, the identification problem is defined as the minimisation of an objective function (called also target function), Ψ . The objective function is expressed in terms of stress $\bar{\sigma}$ as

$$\Psi = \sum_j \sum_k ({}^{jk} \bar{\sigma}^{num} - {}^{jk} \bar{\sigma}^{ex})^2. \quad (3.15)$$

The superscript, *ex*, refers to the experimental results (see *Chapter 7*), whereas *num* refers to the optimised quantities. The stress values are defined as

$$\begin{aligned}
{}^{jk}\bar{\sigma}^{ex} &= \sqrt{({}^{jk}\sigma_L^{ex})^2 + ({}^{jk}\sigma_T^{ex})^2}, \\
{}^{jk}\bar{\sigma}^{num} &= \sqrt{({}^{jk}\sigma_L^{num})^2 + ({}^{jk}\sigma_T^{num})^2}.
\end{aligned}
\tag{3.16}$$

The letters in superscript, j and k , denote isocontour of the plastic equivalent strain and loading path, respectively.

Chapter 4

Thermomechanical Coupling

Adiabatic and Fully Coupled Analysis

4.1. Introduction

In metal forming, particularly in extrusion, the effect of temperature is very crucial, since a heterogeneous temperature field resulting from competition between heating and cooling of the work piece is produced (Wagoner and Chenot, 2001).

Cooling can result from

- contact with tools, which operate at relatively low temperature in order to avoid possible excessive deformation of the tools themselves,
- radiation and convection at free surfaces.

Heating occurs due to

- plastic deformation of the work piece,
- friction between the surfaces in contact.

To establish a better description of the material behaviour, isothermal analysis is not a proper choice at all due to the fact that temperature dependency of the material is simply ignored. An adiabatic mechanical analysis is used in cases where mechanical deformation causes heating, but the event is so rapid that this heat has no time to diffuse throughout the material so cooling is neglected. Temperature is considered as an internal state variable in adiabatic analysis. On the other hand, a fully coupled temperature-displacement procedure is used to solve simultaneously for the stress, displacement and temperature fields. Therefore, temperature is an additional degree of freedom. In both cases, the thermal energy balance equation is solved to calculate the temperature by considering all the heat flux, which is the amount of heat energy that crosses the unit surface per unit time. Finally, the corresponding update of material properties, e.g. yield stress, and/or model parameters which are given with respect to temperature have to be performed to capture temperature dependency.

4.2. Fully coupled temperature-displacement analysis

The thermal energy balance has to be satisfied. The summation of the rate of heat entering and the rate of energy generated within the body has to be equal to the rate of increase of internal energy, which means

$$\rho \dot{U} = - \frac{\partial}{\partial \underline{x}} \cdot \underline{q} + r, \quad (4.1)$$

where ρ is the material density.

The internal energy rate per unit mass, \dot{U} , is expressed by the help of heat capacity, c , and rate of temperature, $\dot{\theta}$, as

$$\dot{U} = c \dot{\theta}. \quad (4.2)$$

For the heat flux per unit volume generated within the body, r , it was assumed in this study that only plastic deformation has a contribution as

$$r = \eta \underline{\sigma} : \underline{\dot{\epsilon}}^{pl}, \quad (4.3)$$

η , called as the inelastic heat fraction, defines the amount of dissipation converted into heat.

The equations for heat propagation can be analysed similarly to the mechanical equation. A general law of heat conservation is first defined, then the material response to heat flux is determined which

is analogous to the constitutive equation and finally boundary conditions, i.e. convection and/or radiation, are examined.

In the case of coupled temperature-displacement analysis, conductivity of the points within the body is considered which means that heat exchange is possible. Heat conduction is assumed to be governed by the Fourier law as below

$$\underline{q} = -\underline{K} \cdot \frac{\partial \theta}{\partial x}, \quad (4.4)$$

where \underline{K} is the thermal conductivity matrix. The negative sign comes from the experimental evidence that heat always flows in the direction of decreasing temperature.

Heat convection as one of the boundary conditions applied normal to free surfaces with a surrounding temperature of θ_0 is written as

$$q_n = -h(\theta - \theta_0), \quad (4.5)$$

where h is called film coefficient.

Heat flux due to radiation to the environment is governed by

$$q = -A[(\theta - \theta_z)^4 - (\theta_0 - \theta_z)^4], \quad (4.6)$$

with A as radiation constant defined by emissivity of the surface, ε^S , and the Stefan-Boltzmann constant, σ^{S-B} , i.e. $A = \varepsilon^S \sigma^{S-B}$. Whereas θ_z denotes the absolute zero temperature, the ambient temperature is labelled as θ_0 in Equation (4.6). The effect of radiation on thermal energy balance is smaller than one obtained via convection.

4.3. Adiabatic analysis

The heat transfer between specimen and its environment is neglected in adiabatic analysis. The particles composing the material are assumed as isolated particles. Interactions between these isolated particles are not allowed with respect to temperature. Since there is no heat flux rather than heat generated due to plastic deformation available in adiabatic analysis, the heat equation solved at each integration point, i.e. Equation (4.1), becomes

$$\rho \dot{U} = r, \quad (4.7)$$

where r is as described in Equation (4.3).

Rise of temperature, $\dot{\theta}$, due to dissipation is, hence, calculated by combining Equation (4.2) and Equation (4.3) into Equation (4.7):

$$\dot{\theta} = \frac{\eta \underline{\sigma} : \underline{\dot{\epsilon}}^{pl}}{\rho c} . \quad (4.8)$$

Chapter 5

Implementation of User Defined Materials-VUMATs

5.1. Introduction

As discussed before, the proposed modified version of Cazacu and Barlat yield criterion (see Equation (2.26)) together with the associated flow rule is a non-standard constitutive model and thus not provided in commercial finite element (FE) programmes. Therefore, special techniques such as user defined material laws are required to perform simulations on the basis of this material model. The commercial FE software ABAQUS provides user interfaces linking to the main programme in order to allow the user to formulate and incorporate user defined material laws (Abaqus, 2006b). The user defined material applicable for ABAQUS/Standard is called UMAT. The equivalent version for ABAQUS/Explicit is called VUMAT. The choice of VUMAT was made since ABAQUS/Explicit provides more promising features such as reasonable computational time and better contact definitions especially in simulations of extrusion (Abaqus, 2006a).

The modified version of Cazacu and Barlat model has been implemented in this study as two VUMATs, since temperature dependency was captured by two different approaches as discussed in *Chapter 4*, namely adiabatic analysis and fully coupled temperature-displacement analysis. The implemented codes, however, have quite similar structures.

5.2. General characteristics of VUMAT

The stress tensor, user defined state variables, internal energy and plastic dissipation are defined by the user. That means these are used for Write purpose. The rest of the variables are used only for Read purpose. The variables used in the header of VUMAT and corresponding short descriptions are summarized in the *Appendix*.

Some significant characteristics of VUMAT are listed as below:

- VUMAT uses a two-state architecture consisting of “old” and “new”. The initial values at the beginning of each increment have to be assigned in the “old” arrays. “New” arrays have to be allocated for updated results at the end of each increment. ABAQUS performs automatically the conversion of “old” and “new” by setting the value of “new” arrays into “old” arrays for the next increments.
- The VUMAT interface is written to take advantage of vector processing. As a result, branching inside loops has to be avoided.
- In VUMAT, no information is provided about element numbers. Data are passed in and out in large blocks with “nblock” which typically is equal to 64 or 128. Each entry in an array of length, “nblock”, corresponds to a single material point. All material points in the same block have the same material name and belong to the same element type. All operations are done in vector mode with “nblock” vector length.
- The time increment can not be redefined in VUMAT. The time increment assumed in this study assures the linearisation of the state variables discussed later. In UMAT, “PNEWDT”, i.e. ratio of suggested new time increment to the time increment being used, can be updated.
- The stresses and strains are stored as vectors in both cases. However, for three dimensional elements, the storage scheme of VUMAT is different from that for ABAQUS/Standard with respect to the fifth and sixth components:

$$\text{UMAT: } \mathbf{S} = (\sigma_{11}, \sigma_{22}, \sigma_{33}, \sigma_{12}, \sigma_{13}, \sigma_{23})$$

$$\text{VUMAT: } \mathbf{S} = (\sigma_{11}, \sigma_{22}, \sigma_{33}, \sigma_{12}, \sigma_{23}, \sigma_{13})$$

- The shear strain components in user subroutine VUMAT are stored as tensor components and not as engineering components. However, UMAT uses engineering components.

$$\text{UMAT: } \gamma_{12} = 2\varepsilon_{12}$$

$$\text{VUMAT: } \varepsilon_{12} = \frac{1}{2}\gamma_{12}$$

- In ABAQUS/Explicit, all elements are of first-order (nodes only at their corners) except for the quadratic triangle and tetrahedron, which use a modified second-order interpolation. Instead of elements with full integration, users are forced to choose reduced integration elements in explicit solver. Hence, CAX4R, C3D8R, CPE4R are examples for elements to be used in VUMAT.

5.3. Implementation of VUMATs

The methodology adopted here is the so called operator-split method which divides the problem into elastic and plastic components. In the elastic predictor stage, the stress tensor is calculated with the assumption of a fully elastic strain increment provided by ABAQUS/Explicit. The return mapping algorithm (Ottosen and Ristinmaa, 2005; Simo and Hughes, 1998) is chosen to update the stress tensor when the yield condition is satisfied. The Newton-Raphson method (Ottosen and Ristinmaa, 2005; Simo and Hughes, 1998) is used to calculate the amount of the overstress caused by the applied deformation. The plastic equivalent strain rate and resulting overstress are calculated iteratively. The flowchart of a user defined material implemented can be seen in Figure 5.1.

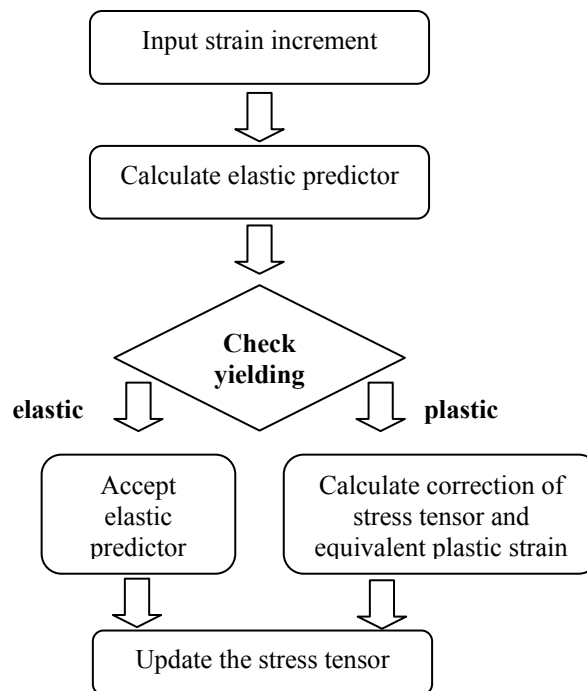


Figure 5.1: Flowchart of implementation of VUMAT

The first step is the elastic predictor where the total incremental strain is assumed to be fully elastic.

The elastic predictor is expressed as

$$\underline{\underline{\dot{\sigma}}}_{trial} = \underline{\underline{C}} : \underline{\underline{\dot{\varepsilon}}}. \quad (5.1)$$

The tensor of elastic moduli denoted by $\underline{\underline{C}}$ is calculated as below:

$$\underline{\underline{C}} = \lambda_L \underline{\underline{1}} \otimes \underline{\underline{1}} + 2\mu_L \underline{\underline{I}}, \quad (5.2)$$

where $\underline{\underline{1}}$ is the second-order identity tensor whereas $\underline{\underline{I}}$ is the fourth-order symmetric identity tensor.

Moreover, μ_L and λ_L are the Lamé constants, which can be expressed by Young's modulus, E , and

Possion's ratio, ν :

$$\begin{aligned} \mu_L &= \frac{E}{2(1+\nu)} \\ \lambda_L &= \nu \frac{E}{(1-2\nu)(1+\nu)}. \end{aligned} \quad (5.3)$$

After prediction of stresses, $\underline{\underline{\sigma}}_{trial}^{new} = \underline{\underline{\sigma}}^{old} + \underline{\underline{\dot{\sigma}}}_{trial}$, yielding is checked by the yield criterion described in Equation (2.26).

If the material point in the current time step remains elastic, i.e. $f < 0$, no correction is needed.

Thus, the prediction is saved so that the increment is finalised without correction of stress tensor resulting in

$$\underline{\underline{\sigma}}^{new} = \underline{\underline{\sigma}}_{trial}^{new}. \quad (5.4)$$

If the yield function indicates that plastic deformation takes place, the equivalent plastic strain has to be calculated and updated for the next increment. Moreover, the stress values have to be corrected because the prediction was done under the assumption of elasticity.

The plastic multiplier, $\dot{\gamma}$, is calculated as

$$\dot{\gamma} = \frac{f^{trial}}{2\mu_L \left[1 + \frac{H}{3\mu_L} \right]}, \quad (5.5)$$

where $f^{trial} = (\bar{\sigma} - \tau_y) / \bar{\sigma}$ and $\bar{\sigma}$ is equivalent stress defined as

$$\bar{\sigma} = \left[\left(\sqrt{J_2^\circ} \right)^3 - J_3^\circ \right]^{1/3}. \quad (5.6)$$

The yield stress in shear, τ_y , is expressed either in Equation (2.27) or Equation (2.28) depending on the test where the yield strength was measured. Whereas the hardening modulus, H , was already defined in Equation (2.30).

After that, stress tensor is updated for the next increment with the return mapping as

$$\underline{\sigma}^{new} = \underline{\sigma}^{trial} - \underline{\sigma}^{return}. \quad (5.7)$$

Plastic corrector, $\underline{\sigma}^{return}$, is calculated via plastic multiplier:

$$\underline{\sigma}^{return} = 2\mu_L \dot{\gamma} \frac{\partial f}{\partial \underline{\sigma}}. \quad (5.8)$$

The required derivatives are formulated as below,

$$\frac{\partial f}{\partial \underline{\sigma}} = \frac{\partial f}{\partial J_2^\circ} \frac{\partial J_2^\circ}{\partial \underline{\sigma}} - \frac{\partial f}{\partial J_3^\circ} \frac{\partial J_3^\circ}{\partial \underline{\sigma}}. \quad (5.9)$$

The equivalent plastic strain rate is calculated as,

$$\dot{\varepsilon}^{pl} = \sqrt{\frac{2}{3} \dot{\gamma} \frac{\partial f}{\partial \underline{\sigma}} : \dot{\gamma} \frac{\partial f}{\partial \underline{\sigma}}}. \quad (5.10)$$

After the stress update and state variable update were done, VUMAT is called for the next time increment till specified time is reached.

5.3.1. VUMAT for adiabatic analysis

The corresponding material and model parameters are input as described in Table 5.1. The temperature is considered as state variable and calculated as described in Equation (4.8). If the model parameters for strain rate dependency, i.e. D and n in power law, and/or stress-strain curve are provided as tables of temperature, then a subroutine inside VUMAT is called to calculate the resulting softening due to a rise in temperature by interpolation. If the temperature exceeds the limits of input data during the simulation, then there will be no modification.

Input variables	Explanations
Props(1)	Young`s modulus
Props(2)	Possion`s ratio
Props(3)	Initial temperature (θ_o)
Props(4)	Switch parameter for evolution of a_k & b_j (ε_{\max}^{pl})
Props(5)	Number of pairs of rate parameters in Cowper-Symonds model
Props(6-14)	List of reference strain rate (D), power (n) and corresponding temperatures of the pairs of D and n
Props(15)	Inelastic heat fraction (η)
Props(16)	Specific heat (c)
Props(17)	Number of stress-strain curves
Props(18-24)	List of number of stress-strain pairs and corresponding temperatures of the curves
Props(25-67)	Parameters for a_k in Cazacu&Barlat model (A_k, B_k, C_k)
Props(73-155)	Parameters for b_j in Cazacu&Barlat model (A_j, B_j, C_j)
Props(161,162)	First stress-strain pair as (initial yield strength, $\bar{\varepsilon}^{pl} = 0$)
Props(163-)	Further stress-strain pairs

Table 5.1: Input variables used in VUMAT for adiabatic analysis

The state variables which have to be updated for each increment are listed in Table 5.2.

State variables	Explanations
SDV 1	Equivalent plastic strain
SDV 2	Strain rate
SDV 3	Temperature
SDV 4	Yield strength

Table 5.2: State variables used in VUMAT for adiabatic analysis

5.3.2. VUMAT for fully coupled analysis

The input variables of VUMAT for fully coupled temperature-displacement analysis are almost the same as for adiabatic analysis (see Table 5.3).

Input variables	Explanations
Props(1)	Young`s modulus
Props(2)	Possion`s ratio
Props(3)	Initial temperature (θ_o)
Props(4)	Switch parameter for the evolution of a_k & b_j via either the exponential or polynomial functions
Props(5)	Switch parameter for the calculation of τ_y from the stress-strain pairs from either compression or tension tests
Props(6)	Number of pairs of rate parameters in Cowper-Symonds model
Props(7-15)	List of reference strain rate (D), power (n) and corresponding temperatures of the pairs of D and n
Props(17)	Number of stress-strain curves
Props(18-24)	List of number of stress-strain pairs and corresponding temperatures of the curves
Props(25-67)	Parameters for a_k in Cazacu&Barlat model (A_k, B_k, C_k)
Props(73-155)	Parameters for b_j in Cazacu&Barlat model (A_j, B_j, C_j)
Props(161,162)	First stress-strain pair as (initial yield strength, $\bar{\epsilon}^{pl} = 0$)
Props(163-)	Further stress-strain pairs

Table 5.3: Input variables used in VUMAT for fully coupled analysis

The state variables which have to be updated for each increment are listed in following table.

State variables	Explanations
SDV 1	Equivalent plastic strain
SDV 2	Strain rate
SDV 3	Yield strength

Table 5.4: State variables used in VUMAT for fully coupled analysis

Since the temperature field is calculated by ABAQUS/Explicit, there is no need to allocate an additional state variable for the temperature. The temperature field provided by ABAQUS/Explicit was read by this version of VUMAT so that the input variables, which were provided as tables with function of temperature, are updated by interpolation.

5.4. Verifications of VUMATs

The existing implementation of the original work of Cazacu and Barlat model for ABAQUS/Standard (UMAT) (Graff, 2007) was taken as a fundamental code and used as a verification tool for further implementation procedures. Rate dependency of the proposed version of the model was proven by built-in overstress law in ABAQUS. The verifications of the codes with representing various thermo-mechanical conditions with single-element and structures were performed via comparing the results obtained by ABAQUS.

Chapter 6

Characterisation of Billets: Rate-dependent Yielding

6.1. Introduction

The uniaxial compression or upset test (Dieter, 1988) of a short cylinder between flat parallel punches is a common test for measuring the flow stress for metal working applications. Compression tests of ZE10 and ZEK100 specimens were performed at different strain rates and test temperatures. With the help of finite element (FE) simulations, the experimental results of both alloys were regenerated with the model parameters accounting for rate dependency, i.e. D and n , which is later used as input for simulation of metal forming processes such as extrusion (Lapovok et al., 2004) and (Li et al., 2006).

6.2. Experiments

In compression tests, a cylinder of diameter, d_o , and initial height, h_o , is compressed in height, h , and spread out in diameter, d , according to the conservation of volume:

$$d_o^2 h_o = d^2 h . \quad (6.1)$$

The reaction force, P , is measured as a function of the punch displacement. Since there is no necking which limits uniform deformation as in the case of tensile tests, the compression test can be carried out to higher strains. However, the friction between specimen and punch can lead to inhomogeneous deformation giving rise to barrelling of the specimen. This variation of the cross section of the specimen results in a triaxial stress state and hence makes determination of flow stress complicated. The following relations are derived by neglecting the friction between specimen and punch. Total true strain can be calculated as

$$\varepsilon^{true} = -\ln\left(\frac{h}{h_o}\right), \quad (6.2)$$

which has 2 contributions, namely elastic and plastic strain,

$$\varepsilon^{true} = \varepsilon^{el} + \varepsilon^{pl}. \quad (6.3)$$

As a result, the plastic strain can be written as

$$\varepsilon^{pl} = \varepsilon^{true} - \sigma^{true} / E, \quad (6.4)$$

where E is Young's modulus.

The corresponding stress values are

$$\sigma^{true} = \frac{P}{A} = \frac{Ph}{A_o h_o}. \quad (6.5)$$

The compression tests on cylindrical specimens with $d_o = 10$ mm and $h_o = 15$ mm machined from as-cast ZE10 and ZEK100 billets were performed at three different strain rates, 0.1, 1 and 10 s⁻¹, and three different test temperatures, 300, 400 and 500°C, which form a 3x3 test matrix shown in Figure 6.1. The symbols indicated in Figure 6.1 characterise the respective curves of the following graphs (e.g. Figure 6.2) when necessary.

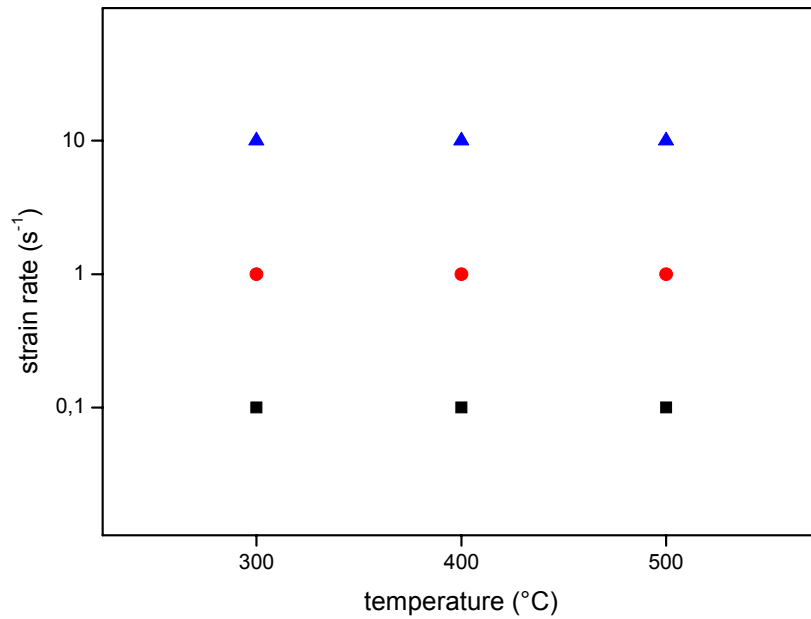


Figure 6.1: Experimental matrix performed for each alloy

Electrical current was used to heat up the specimens in the experiments. In order to adjust the required test temperatures, temperature was monitored via a thermocouple placed on the surface at the middle of the specimen height. After reaching the desired temperature, homogenous temperature throughout the specimen could be achieved by letting the system sufficient time. Finally, the upper punch was moved according to the desired strain rate toward the specimen.

Figure 6.2 illustrates the overall behaviour of specimens with respect to strain rate and temperature dependency of both alloys. First, an increase in test temperature by keeping the strain rate constant leads to a drop in force, which means thermal softening. Secondly, if strain rate is increased at any test temperature, the force is increased, which is called strain-rate hardening. Finally, another important result of Figure 6.2 is the difference in mechanical properties between the two alloys. ZEK100 shows a higher strength than ZE10 due to the presence of the grain refinement agent, i.e. zirconium (Zr).

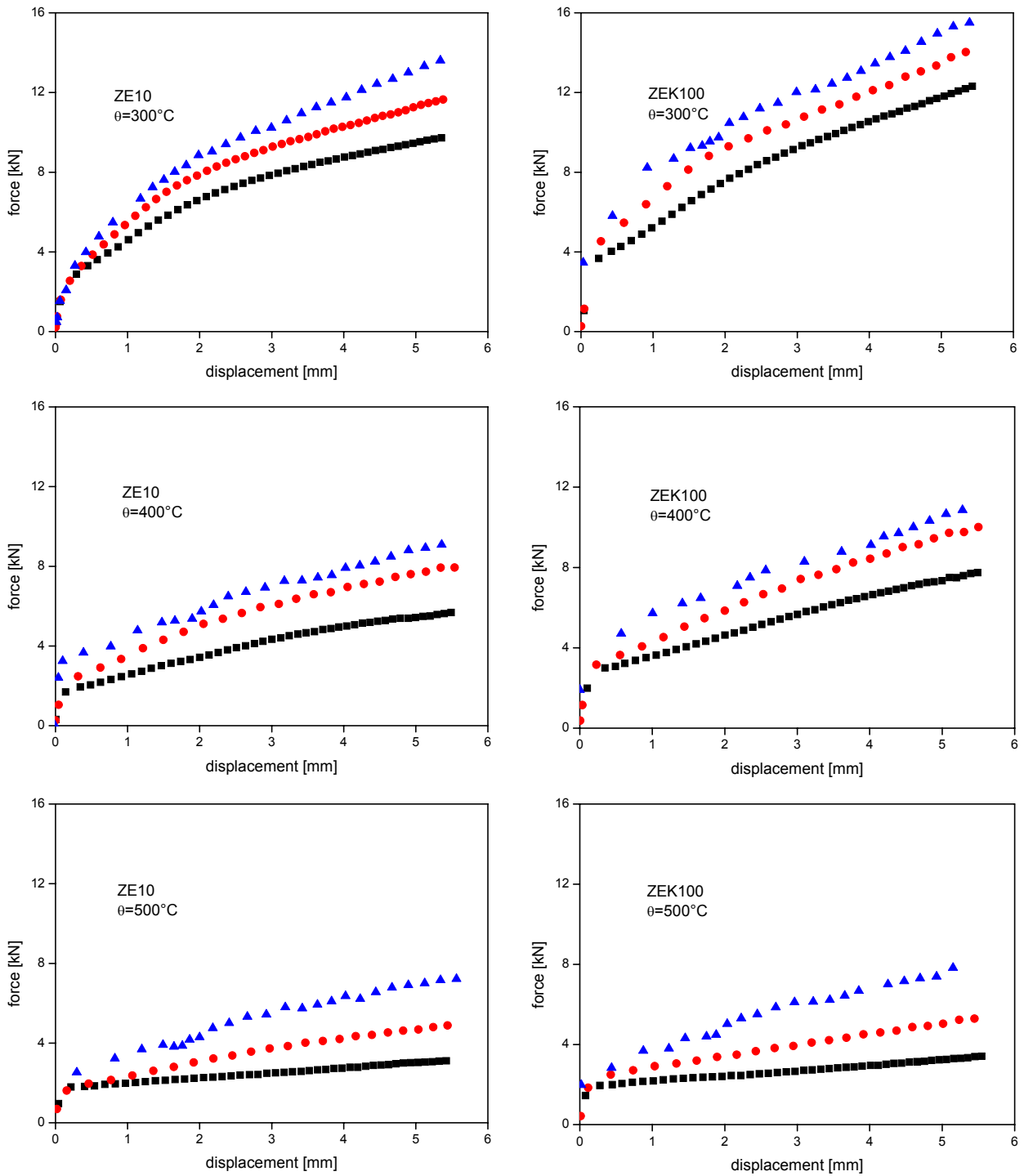


Figure 6.2: Experimental results of ZE10 and ZEK100 with variation of strain rates at different temperatures (see Figure 6.1 for the legend)

Figure 6.3 shows the micrographs taken from the cross sections of cast billets. The average grain size has been determined using a computer aided linear intercept method being $500\mu\text{m}$ for ZE10 and $150\mu\text{m}$ for ZEK100.

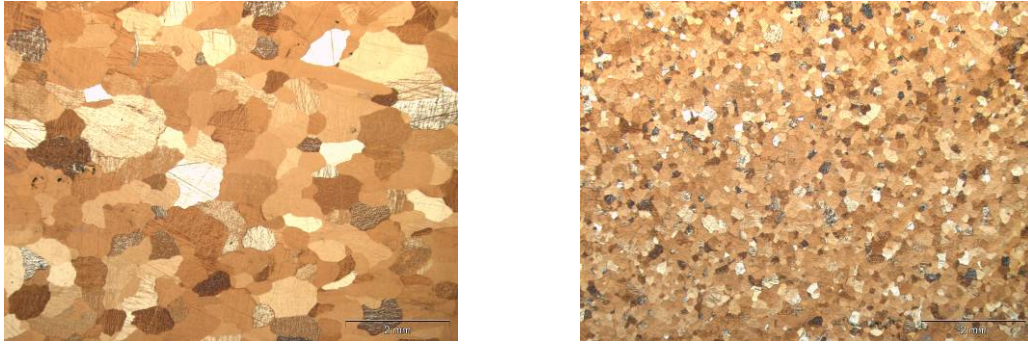


Figure 6.3: Micrographs of cast billets: left ZE10, right ZEK100

Moreover, the effect of Zr can be seen as well in Figure 6.4, where surfaces of the specimens after the compression tests are shown. The deformation results in higher roughness in the case of ZE10.

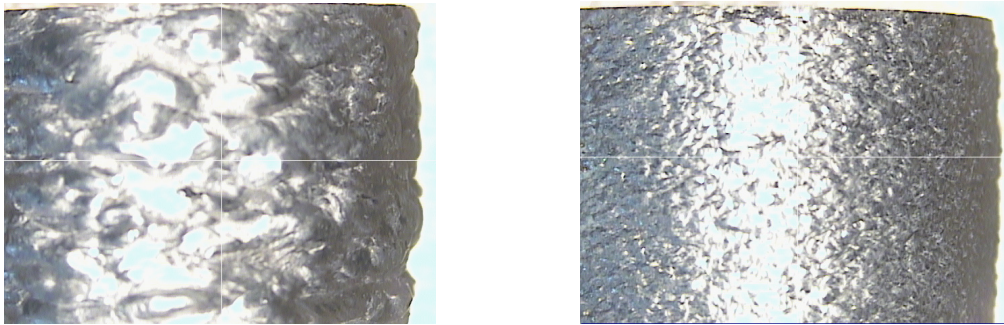


Figure 6.4: Surface qualities of specimens after compression tests: left ZE10, right ZEK100

Finally, the barrelling of the specimens after the compression tests can be seen in Figure 6.4. This provides a good possibility to determine the friction existing between punch and specimen as explained later.

6.2.1. Temperature measurements

As mentioned before, a thermocouple was placed on the surface at the middle of the specimen height in order to measure the temperature during the experiments. The measured temperature shown in the below figures is used later to fit the parameters required in FE simulations. In some experiments, i.e. those with a strain rate of 10 s^{-1} at 500°C , the measured temperature was incomplete due to the loss of contact after experiments were started.

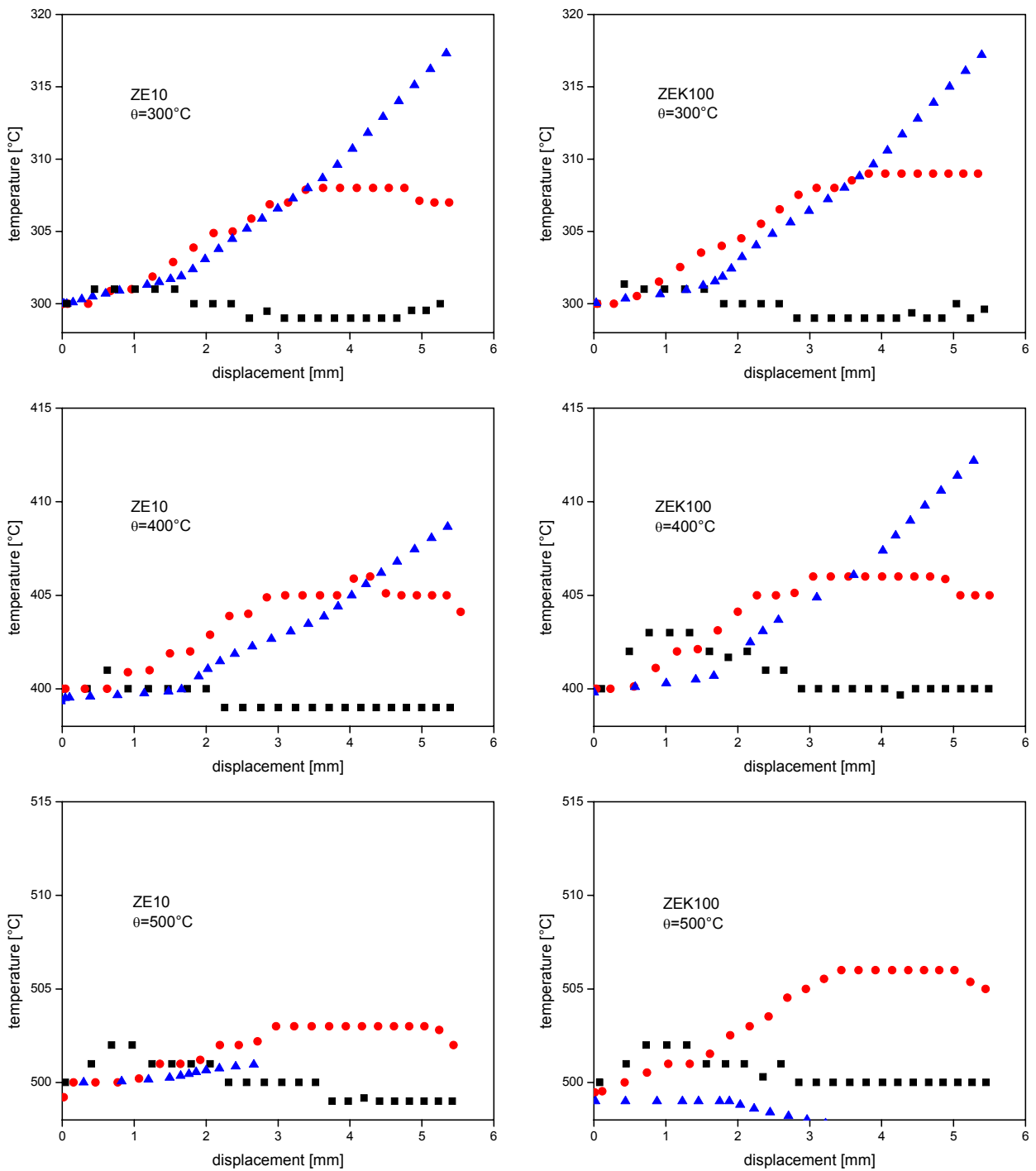


Figure 6.5: Temperature measurements during the experiments (see Figure 6.1 for the legend)

Figure 6.5 shows that the higher the strain rate, the higher is the final temperature as a result of deformation. Due to being fast enough, the experiments with a strain rate of 10 s^{-1} do not show any drop of the measured temperature. On the other hand, the heat generated within the specimen disappeared after some time in the case of strain rates of 1 and 0.1 s^{-1} . The temperature dropped after

a peak value in the case of strain rate of 1 s^{-1} . The temperature of the specimens compressed with a strain rate of 0.1 s^{-1} remains almost constant.

6.3. Simulations

Due to the symmetry of the specimens, a quarter of the specimen was meshed with axisymmetric continuum elements having 4 nodes, CAX4R and CAX4RT. The punch was defined as a rigid surface having a reference node which was assigned to have ramped displacement to provide compression as shown in Figure 6.6.

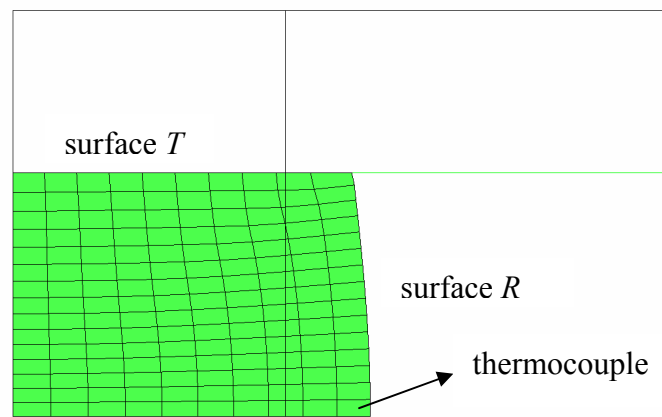


Figure 6.6: FE deformed mesh with superimposed initial geometry

The Coulomb friction between the rigid punch and the top layer elements of the FE mesh was defined as described in the next section.

The material properties used for the simulations can be seen in Table 6.1. It is assumed that these material properties do not depend on temperature.

Material properties	Values
Young modulus, E , [MPa]	45000
Possion`s ratio, ν , [-]	0.3
Specific heat, c , [J/kg K]	965
Density, ρ , [g/cm ³]	1.74
Conductivity, k , [W/m K]	146

Table 6.1: Material properties of ZE10 and ZEK100 used for the simulations

The experimental results for $\dot{\epsilon} = 0.1 \text{ s}^{-1}$ show good agreement with rate-independent simulations. As a result, temperature dependent flow curves were tabulated as pairs of stresses and plastic strains, which were calculated from the measured force and the displacement of the punch providing a strain rate 0.1 s^{-1} as described in Equation (6.4) and Equation (6.5), respectively. Figure 6.7 shows the elastoplastic behaviour of both alloys used as inputs for the simulations.

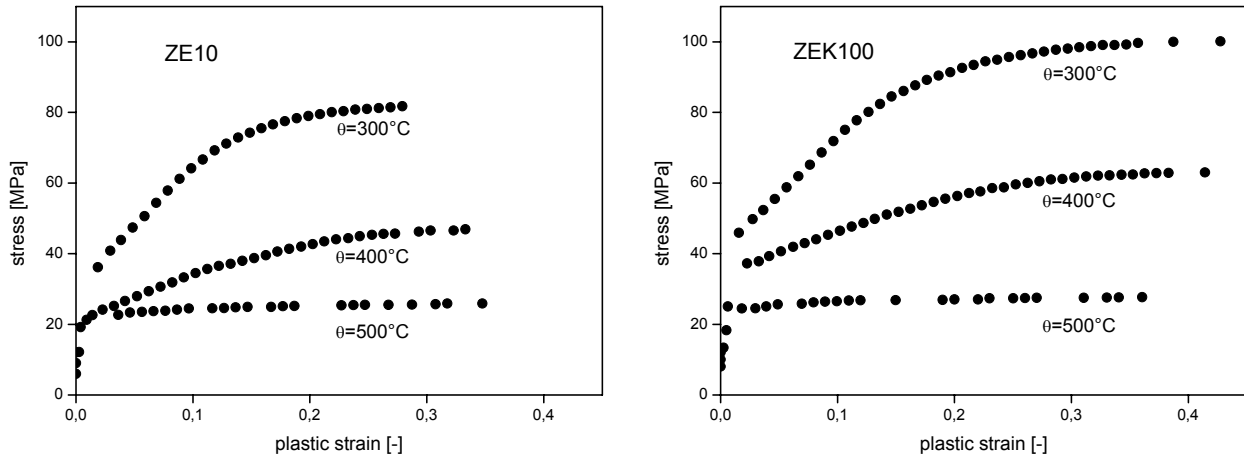


Figure 6.7: Elastoplastic material inputs used in the simulations

The yield stresses at temperatures which are different from the test temperatures are calculated by interpolating the isothermal flow curves.

6.3.1. Material model

Asymmetry in tension/compression is not crucial since tension is not pronounced in such experiments. To this end, the implemented codes (see *Chapter 5*) were adjusted so that conventional von Mises (von Mises, 1928) plasticity was used in the simulations. In order to mimic von Mises plasticity, the model parameters have to be selected as:

$$\begin{aligned} a_k (k = 1, \dots, 6) &= 1, \\ b_j (j = 1, \dots, 11) &= 0. \end{aligned} \tag{6.6}$$

6.3.2. Friction

During deformation, as the metal cylinder increases its diameter, frictional forces occur between the surfaces of the specimen being in contact with the punch while the other parts of specimen can flow radially undisturbed. This leads to a barrelled specimen profile as seen in Figure 6.4.

The standard Coulomb friction model provided by ABAQUS was used in the simulations. The frictional stress, τ_{fric} , is proportional to the contact pressure, p , as

$$\tau_{fric} = \mu p, \tag{6.7}$$

where μ is the friction coefficient.

The barrelling of the specimen depends on the friction coefficient. Simulations with varying friction coefficients, μ , were performed as shown in Figure 6.8. The curvatures of the barrelled specimens are increased with increasing the friction coefficient.

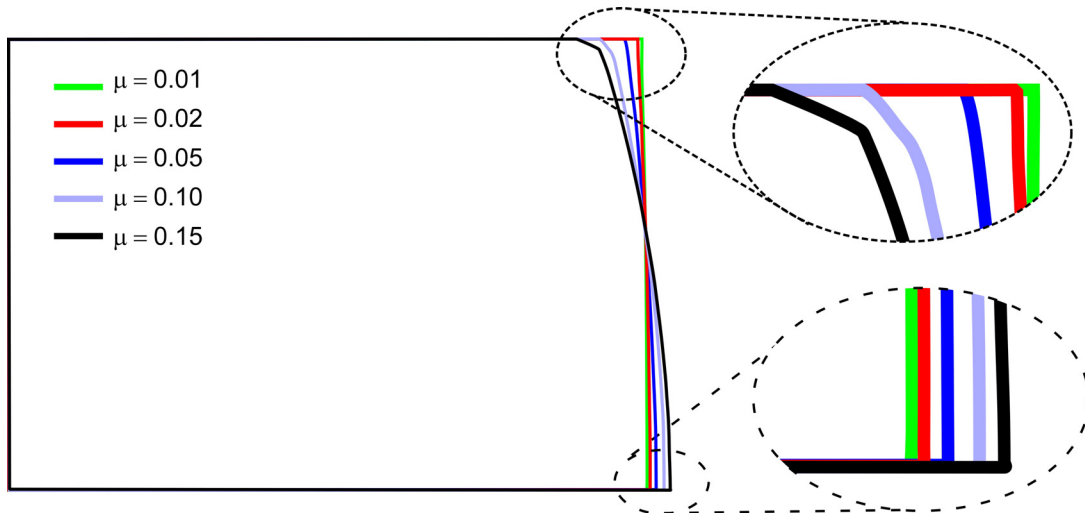


Figure 6.8: Effect of friction coefficient on barrelling of specimen

Since the deformed ZE10 specimen shown in Figure 6.4 has a very rough surface, it is almost impossible to get a reliable surface profile. Hence, the deformed ZEK100 specimen was used for calibrating the friction coefficient. The simulation result with $\mu = 0.05$ gave the best qualitative agreement with the experimental result as seen in Figure 6.9 so that this value is used for further simulations to fit the other model parameters.

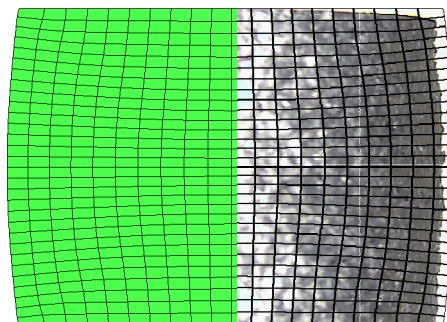


Figure 6.9: Qualitative comparison of barrelling of specimen with deformed mesh

6.3.3. Temperature predictions

As discussed in *Chapter 4*, calculations of temperature in two separately implemented VUMATs were handled with two different approaches, namely adiabatic and fully thermo-mechanically coupled analysis, respectively.

6.3.3.1. Adiabatic analysis

In order to determine the inelastic heat fraction parameter, η , (see Equation (4.8)) parametric studies with varying of η were performed and the results were compared with the temperature measurements during the experiments at 300°C as seen in Figure 6.10.

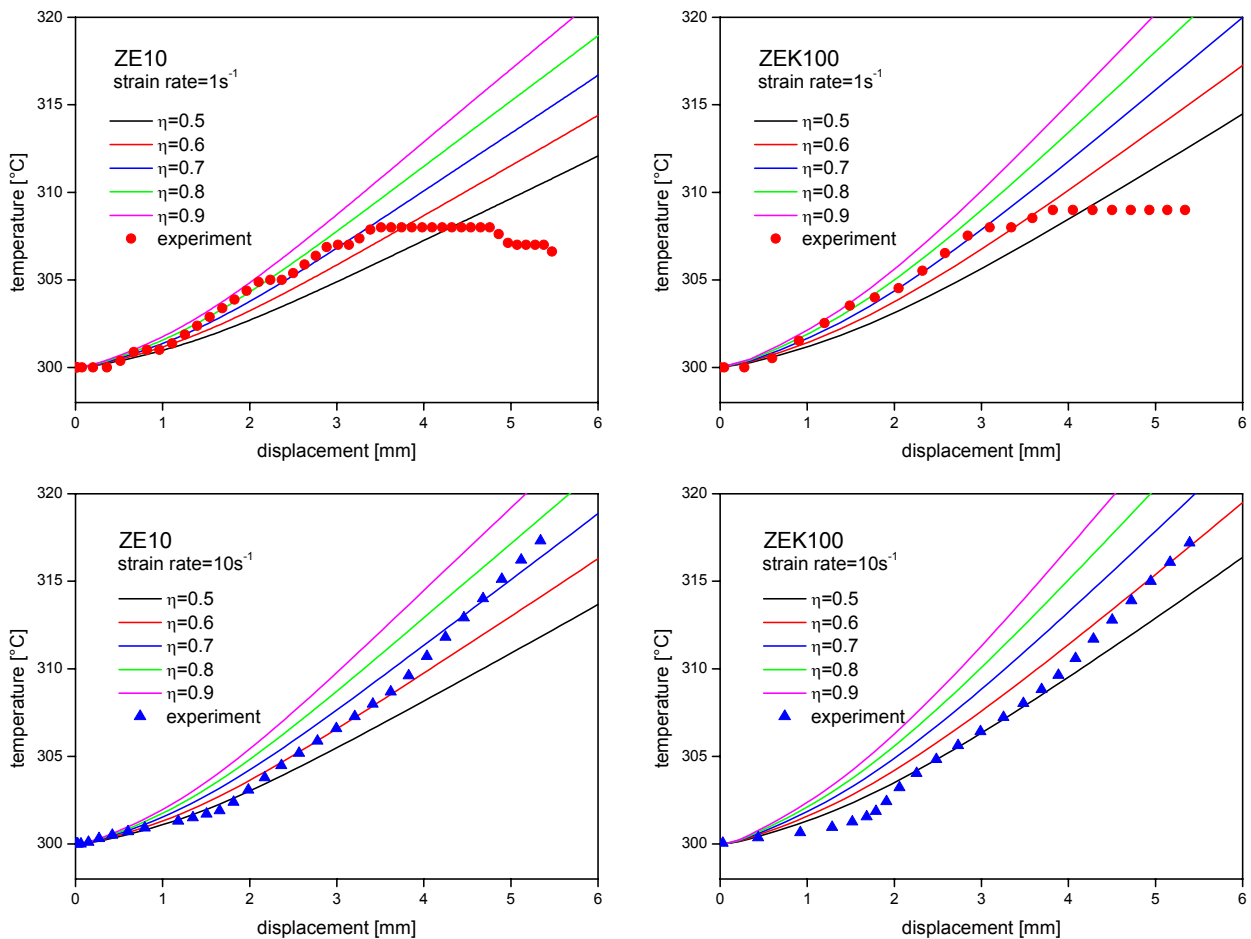


Figure 6.10: Effect of inelastic heat fraction under adiabatic assumption

According to Figure 6.10, the simulation with 70% of heat generation, i.e. $\eta = 0.70$, shows the best coincidence between the simulations and the experiments considering both strain rates. Therefore, this value is used for further simulations in adiabatic analysis.

Figure 6.11 shows the summary of the simulations obtained with $\eta = 0.70$. Increasing strain rate results in increasing temperature. Since ZEK100 shows a higher strength than ZE10, the amount of plastic deformation into heat is larger, which leads to higher temperature.

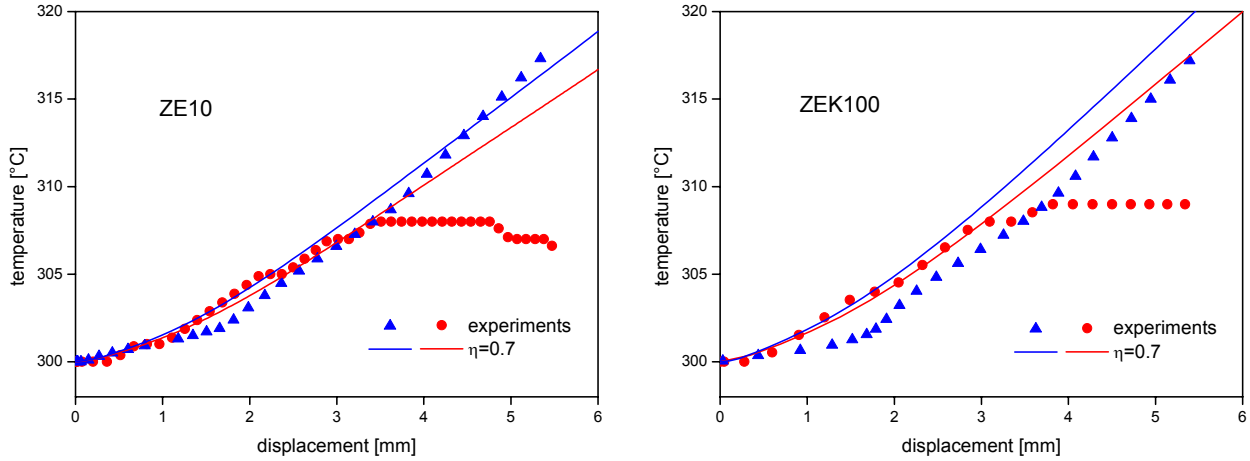


Figure 6.11: Temperature predictions under the assumption of adiabatic heating

6.3.3.2. Fully thermo-mechanically coupled analysis

As in the case of adiabatic analysis, heat generation due to plastic deformation was considered as well. Since unlike in adiabatic analysis heat transfer is possible, the common value of inelastic heat fraction, $\eta = 0.9$, was used in the simulations in fully coupled analysis. The heat generated via plastic deformation is transferred from hot to cold regions within the specimens by conduction.

The heat transfer between the specimen and its environment was handled via convection by considering two different surfaces, which are, namely, the contact surface between the top surface of the specimen and the punch, T , and the contact surface of the specimen subjected to the surrounding environment, R , i.e. the right surface in the mesh in Figure 6.6. The corresponding film coefficients are labelled as h_T and h_R , respectively, which were used to describe the heat transfer via convection as in Equation (4.5).

Figure 6.12 illustrates the results obtained from the simulations with different heat transfer properties.

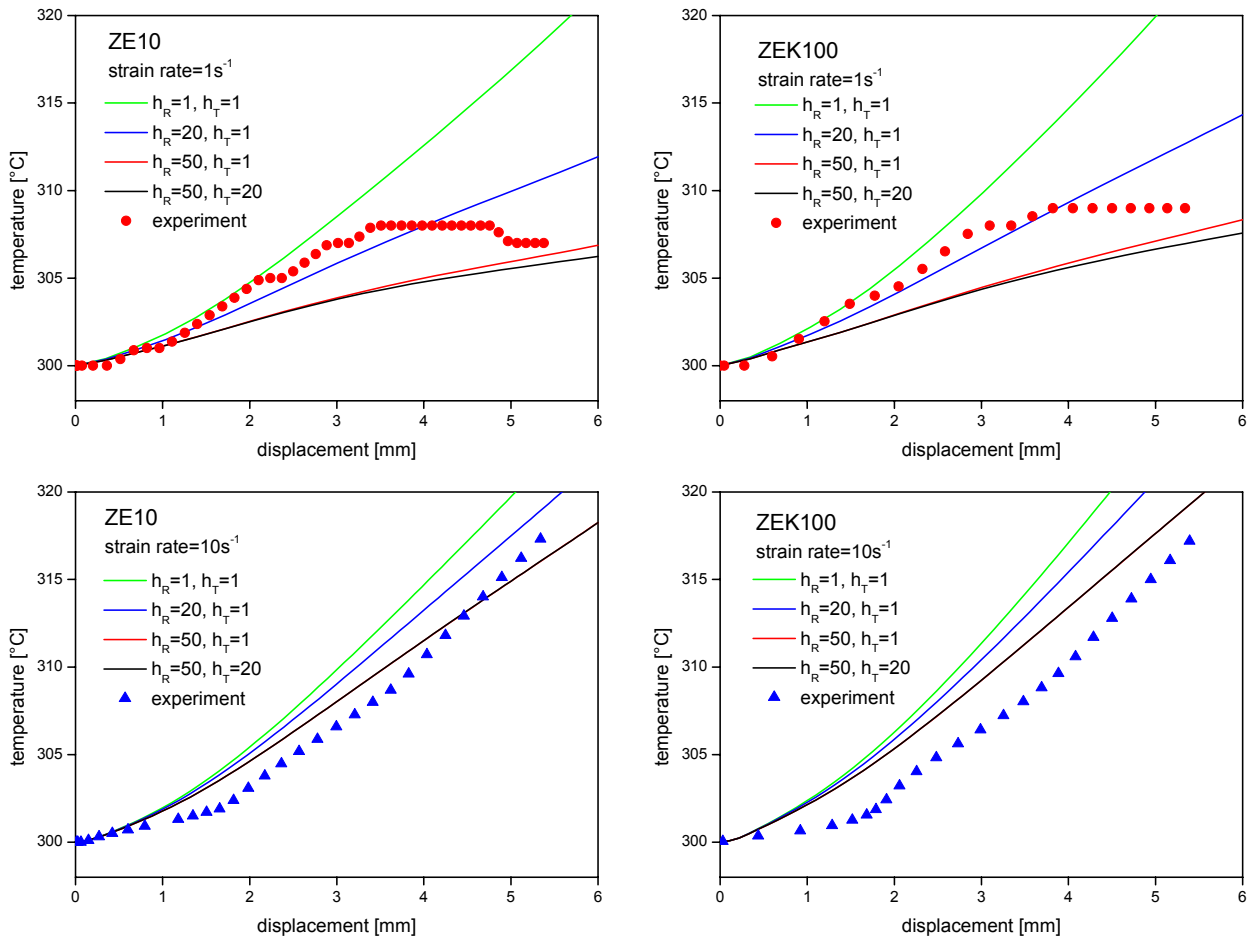


Figure 6.12: Effect of film coefficient used in fully coupled analysis

As seen in Figure 6.12, the effect of h_T is negligible because of the thermocouple location which is relatively far away from the contact between the punch and the specimen (see Figure 6.6). Therefore, the simulations with increasing h_T and keeping h_R constant give the same results in the case of strain rate of 10 s^{-1} and almost the same results with a strain rate of 1 s^{-1} . However, h_R affects the temperature predictions significantly. The higher the value of h_R is, the lower the temperature is.

It is very difficult to capture the measured temperature variations with constant film coefficients. This is especially the case for the experiments with a strain rate of 1 s^{-1} where the temperature drops after reaching a peak value. Therefore, the film coefficients were defined as a function of time. For example, the results obtained by a linear relation between the film coefficient and the simulation time are shown in Figure 6.13.

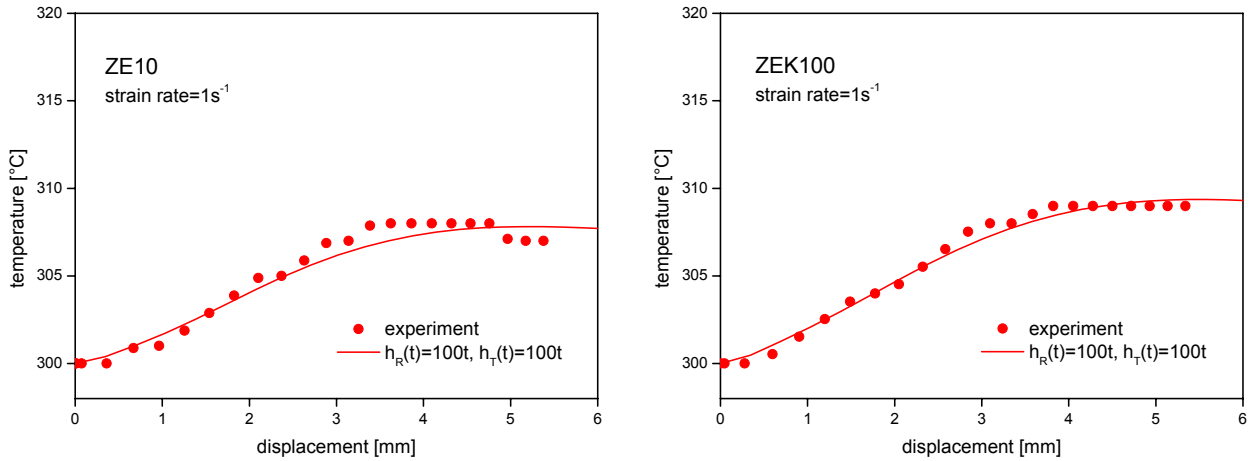


Figure 6.13: Temperature predictions with film coefficients defined as a function of time in fully coupled analysis

Although very good agreement was achieved by varying the film coefficients during the simulations, constant values of film coefficients were considered for simplicity. The pair of film coefficients, $h_R = 20$ and $h_T = 1$, was chosen as the best set considering both strain rates for further discussions. The results obtained by this set can be seen in Figure 6.14.

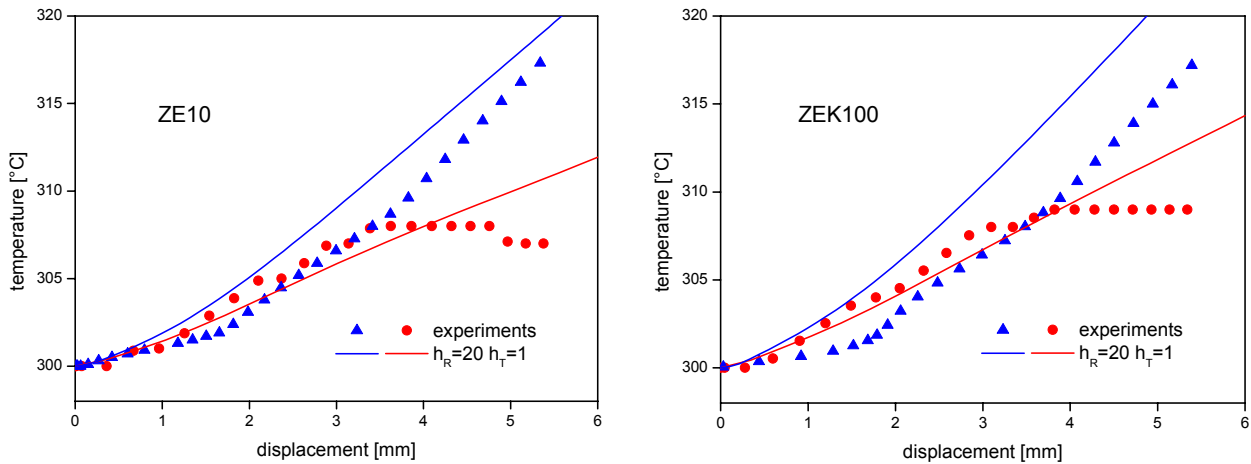


Figure 6.14: Temperature predictions with fully coupled analysis

6.3.3.3. Comparison of temperature predictions

The comparison of both analyses is demonstrated in Figure 6.15, where the results with the best parameters are plotted. The effect of strain rate was better captured in the fully coupled analysis. A larger amount of heat can disappear from the specimen subjected to deformation with $\dot{\epsilon} = 1 \text{ s}^{-1}$, because of being the slower process. Therefore, the difference between the temperatures of simulations with two different strain rates is remarkable. However, this cannot be captured in an adiabatic analysis where only plastic deformation has a contribution to the heat equation as

described before. The simulation with heat transfer at a strain rate = 10 s^{-1} predicts higher temperature than the corresponding one with adiabatic analysis. This is due to the fact that $\eta = 0.9$ was used in the simulations with heat transfer instead of $\eta = 0.7$, which was the optimum value used in the adiabatic analyses.

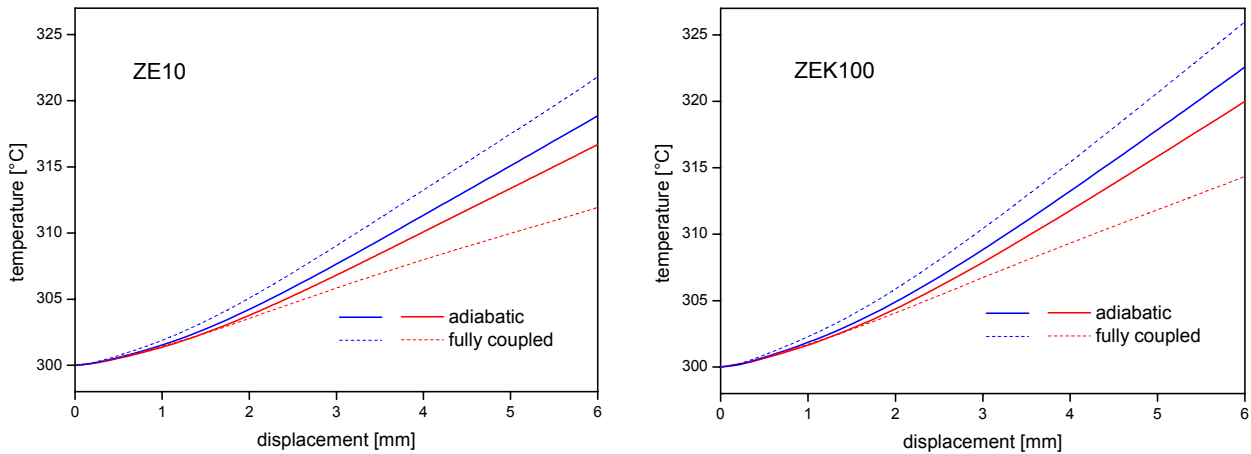
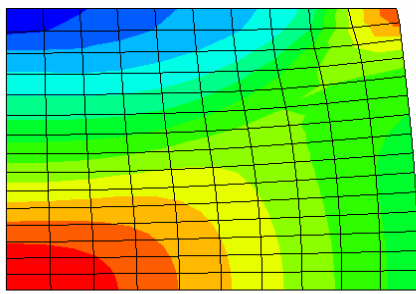
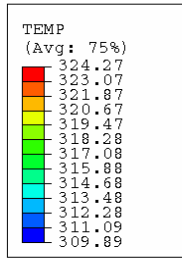


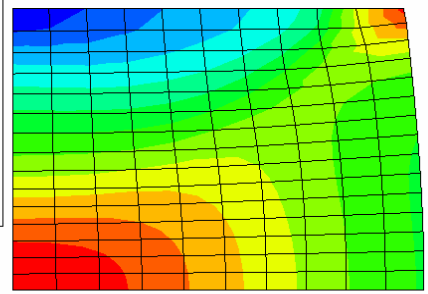
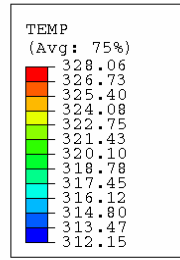
Figure 6.15: Comparison of temperature predicted by two different approaches

Figure 6.16 shows the temperature distributions of the specimen obtained by the simulations with adiabatic analysis. The temperature distributions within the specimens subjected to different strain rates appear almost the same. The hottest region for all cases is predicted in the centre of the specimens. On the other hand, the contact region between the specimen and the punch where the least deformation occurred is the coldest region within the specimens.

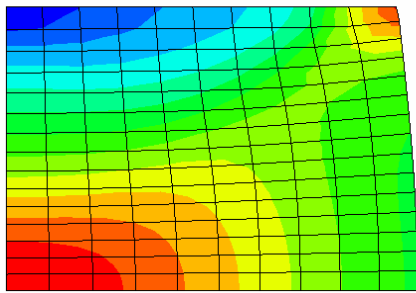
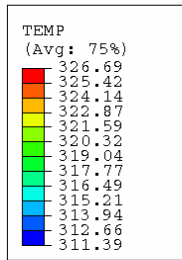
Figure 6.17 shows the results obtained by the fully coupled analysis. The temperature distributions for strain rate = 10 s^{-1} show the same tendency as in adiabatic analyses since it is a fast enough process so the effect of heat transfer is less. However, those for the slower strain rate show different distributions than the others. The contact surface of the specimen subjected to surrounding environment, i.e. the surface R , where the most heat disappears, was observed as colder than the other regions within the specimens.



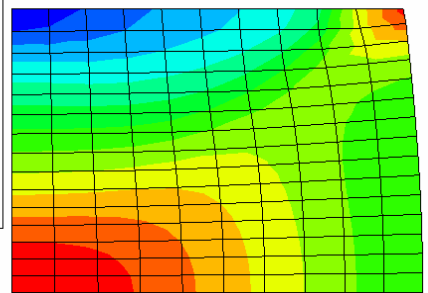
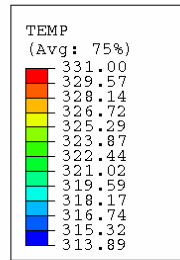
ZE10 with a strain rate of 1 s^{-1}



ZEK100 with a strain rate of 1 s^{-1}

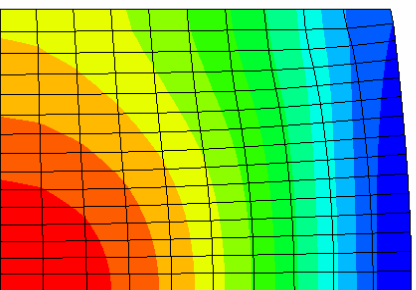
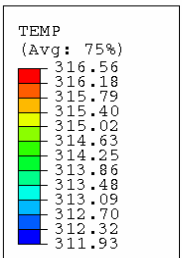


ZE10 with a strain rate of 10 s^{-1}

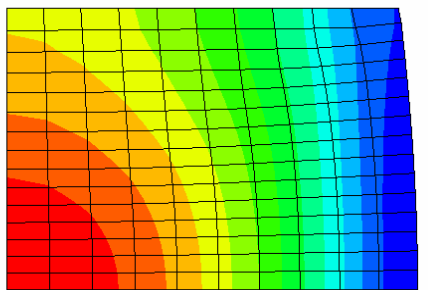
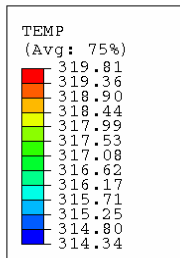


ZEK100 with strain rate of 10 s^{-1}

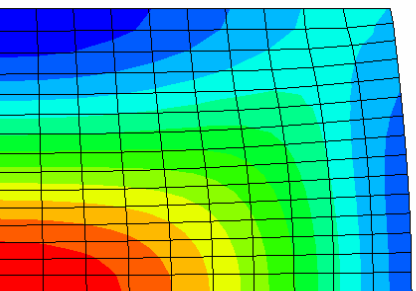
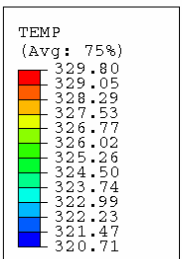
Figure 6.16: Temperature distributions within the specimens at the end of simulation (adiabatic analysis)



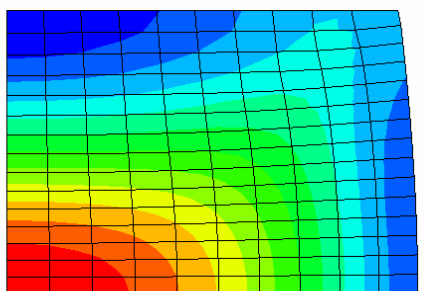
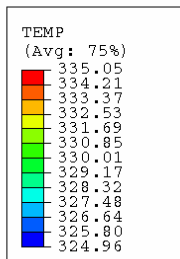
ZE10 with a strain rate of 1 s^{-1}



ZEK100 with a strain rate of 1 s^{-1}



ZE10 with a strain rate of 10 s^{-1}



ZEK100 with strain rate of 10 s^{-1}

Figure 6.17: Temperature distributions within the specimens at the end of simulation (fully coupled analysis)

The reaction forces at different strain rates are plotted in Figure 6.18. Since the temperature difference between the two analyses was not so significant, the reaction forces appear almost the same. As a result, the type of analysis is not important in this context. For further simulations to fit the rate dependent parameters, i.e. D and n , the adiabatic analysis is used.

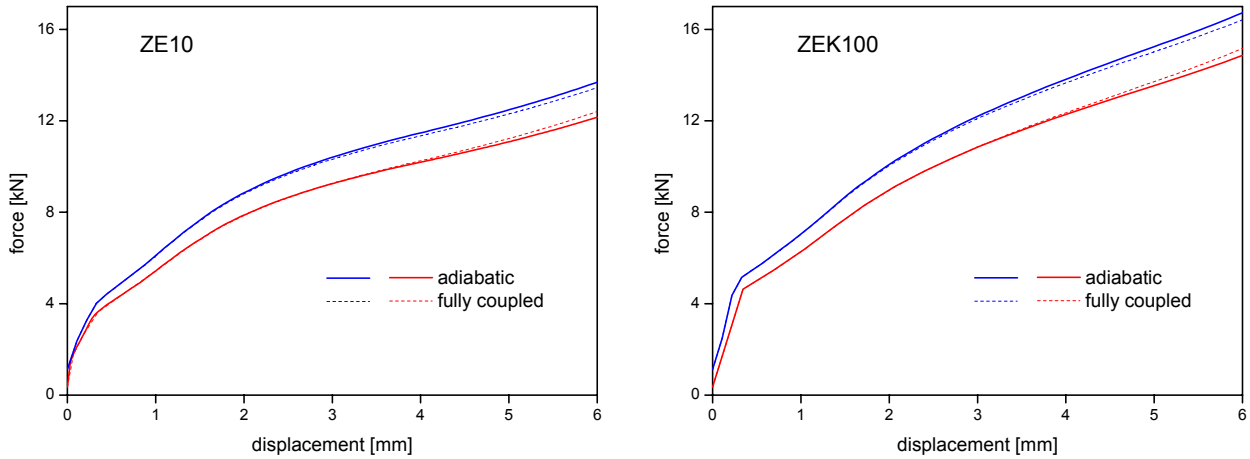


Figure 6.18: Comparison of reaction forces obtained by two different approaches

6.3.4. Parameter identifications

After setting parameters such as friction coefficient and inelastic heat fraction, simulations under adiabatic assumption were performed to regenerate the experimental results as seen in Figure 6.2. The pair of parameters, i.e. D and n , was identified for each test temperature. The Trial-and-Error method was adopted for parameter identification. As seen in Figure 6.19, quite good agreement between simulations and experimental results was obtained.

The experiments show that the rate dependencies of both alloys depend on the test temperatures. A single pair of model parameters is not sufficient to capture the complete rate dependency. As a result, the fitting procedure carried out at each test temperature results in a variation of the parameters with respect to temperature.

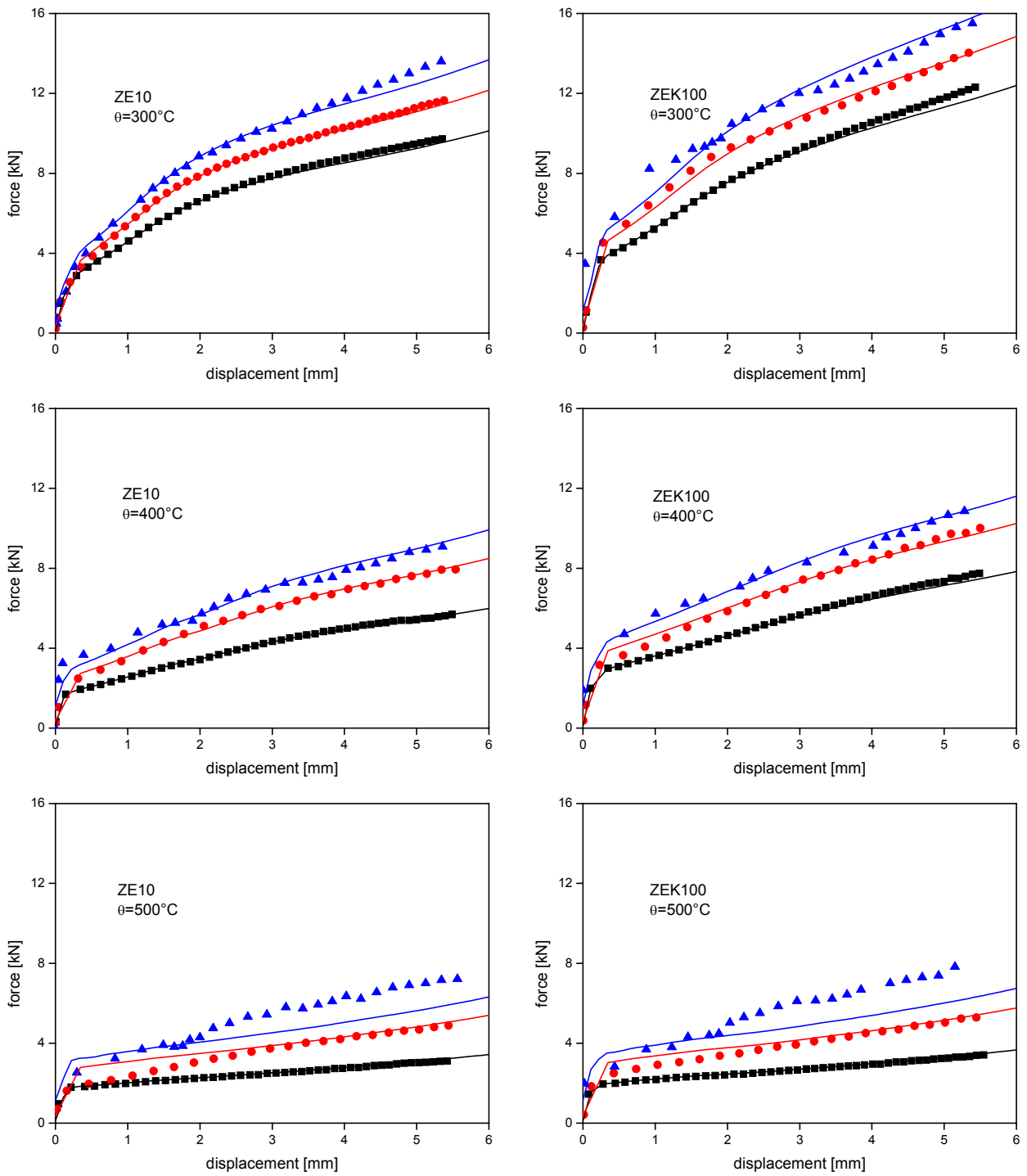


Figure 6.19: Comparison of simulation results under adiabatic assumption with experiments

Table 6.2 shows the fitted parameters for both alloys to get the results presented in Figure 6.19.

<i>ZE10</i>		
D (s^{-1})	n (-)	θ ($^{\circ}C$)
800	4	300
100	5	400
50	6	500

<i>ZEK100</i>		
D (s^{-1})	n (-)	θ ($^{\circ}C$)
800	4	300
400	5	400
50	6	500

Table 6.2: Fitted parameters of power law for both alloys

Table 6.2 can be represented graphically so that the dependency on temperature can be seen.

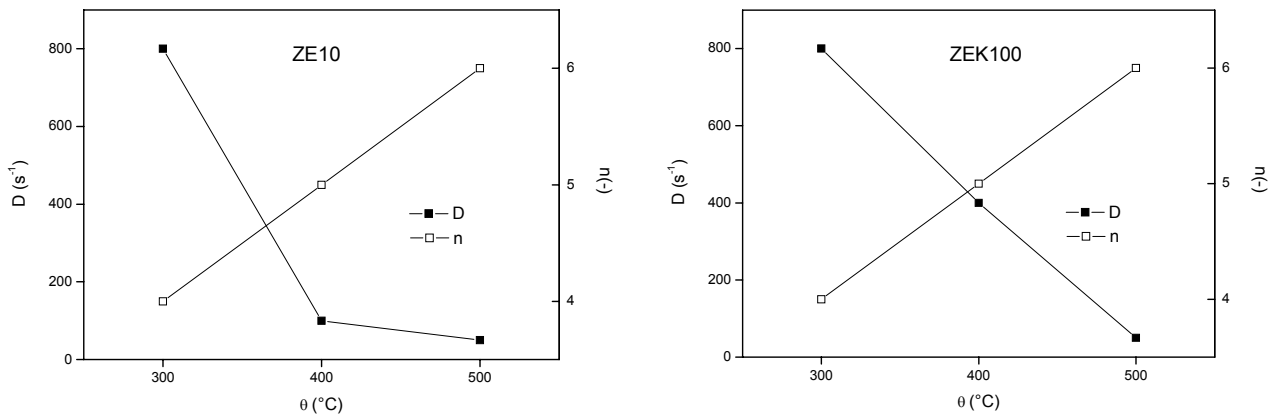


Figure 6.20: Power law parameters in dependence on temperature

The corresponding rate and temperature dependency are used for further predictions of the material behaviour during an extrusion process.

Chapter 7

Characterisation of Billets: Anisotropy & Asymmetry

7.1. Introduction

The model parameters related with anisotropy and/or asymmetry in tension/compression, i.e. a_k and b_j , are identified with the help of a genetic algorithm (see *Chapter 3*) minimising the difference between model predictions and the experimentally observed material behaviour. To this end, tensile and compression tests were performed on as-cast specimens of ZE10 and ZEK100. These experimental results were used as reference in the objective function given in Equation (3.15). The evolution of the parameters, a_k and b_j , (see Equation (3.13) and Equation (3.14)) was defined by the exponential and polynomial functions. Some examples of the parameter identifications with these evolution laws are presented. Finally, simulations of the experiments have been performed to check the generated parameters which are used later in extrusion simulations in *Chapter 8*.

7.2. Experiments

The tensile and compression tests were executed at 300°C and a strain rate of 0.1 s⁻¹ on as-cast specimens prepared at different orientations, namely cast and transverse directions (i.e. TD). Since the profile will be extruded in cast direction, the direction is labelled as extrusion direction, ED, for simplicity. The experiments were repeated for checking the reproducibility of the tests.

7.2.1. Tensile tests

The tensile test, also known as tension test, is widely used to provide basic information on the strength of materials (Dieter, 1988; Hosford, 2005). In this test, a specimen is subjected to a continually increasing uniaxial tensile force resulting in elongation of the specimen till fracture. Due to the necking resulting from localisation of deformation, the information about the mechanical behaviour of the material is limited.

Instead of Equation (6.2), the following analogous equation is used in tensile tests to calculate the total true strain as

$$\epsilon^{true} = \ln\left(\frac{l}{l_o}\right), \quad (7.1)$$

where l is the actual length and l_o is the initial length.

The round cylindrical specimens from ED were machined down to a diameter of 10 mm and a total length of 170 mm with a gauge length of 25 mm. On the other hand, the specimens from TD are round cylinders of 8 mm in diameter and 95 mm in total length with a gauge length of 10 mm. The difference between the two specimen geometries is due to the insufficient diameter (i.e. 100 mm) of the cast materials. The specimens were heated up by electrical current to 300°C to be subjected to a tensile load with a strain rate of 0.1 s⁻¹. The ends (also called shoulders) of the specimens were screwed into the threaded grips. Since both grips were water-cooled, a temperature gradient was established. This enables necking of the specimens within the gauge length without the necessity of any pre-made imperfection on the surface of the specimens. The homogeneity of the experimental temperature throughout the gauge length was monitored by three thermocouples. The locations of the thermocouples are the middle, 20 mm left and 20 mm right from the middle of the specimens.

The experimental results are plotted in Figure 7.1 which shows variation of yielding behaviour with respect to loading directions. The microstructure features such as grain size and grain morphology

significantly depend on the direction due to the nature of the casting process. The grains in casting direction, which corresponds to ED, are smaller and homogeneously distributed than the grains in TD. As a result, the specimens from ED show more strength than the specimens from TD. In comparison with ZE10, ZEK100 shows higher strength in both ED and TD due its finer microstructure (see Figure 6.3).

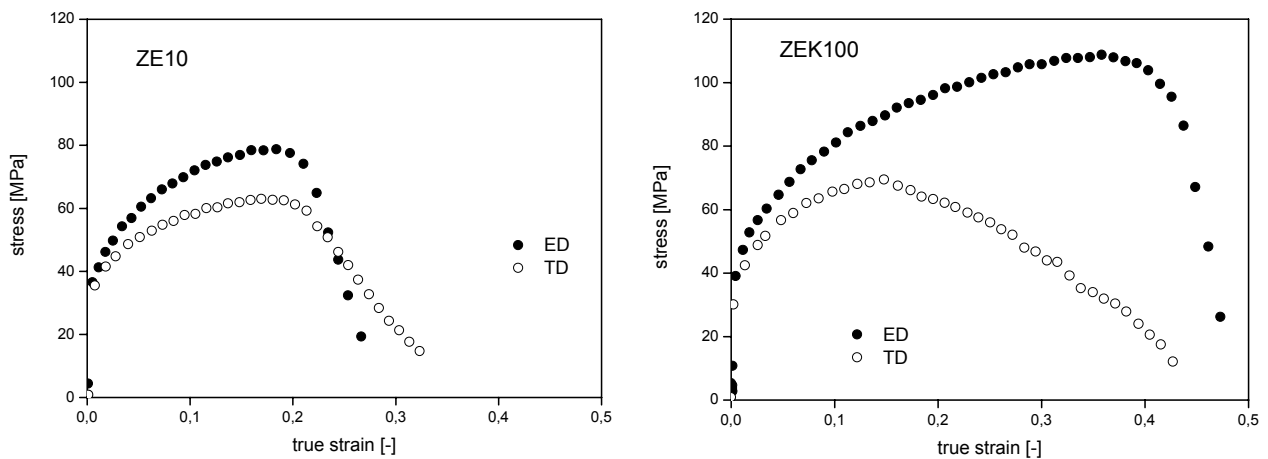


Figure 7.1: Tensile test results: left ZE10, right ZEK100

7.2.2. Compression tests

The compression tests were executed exactly as described in *Chapter 6* except the fact that two material orientations of the specimens, i.e. ED and TD, were selected. The test temperature was 300°C and the specimens were compressed with a strain rate of 0.1 s⁻¹. There exist minor differences in flow stress with respect to the loading directions as seen in Figure 7.2 in comparison with the tensile test results illustrated in Figure 7.1.

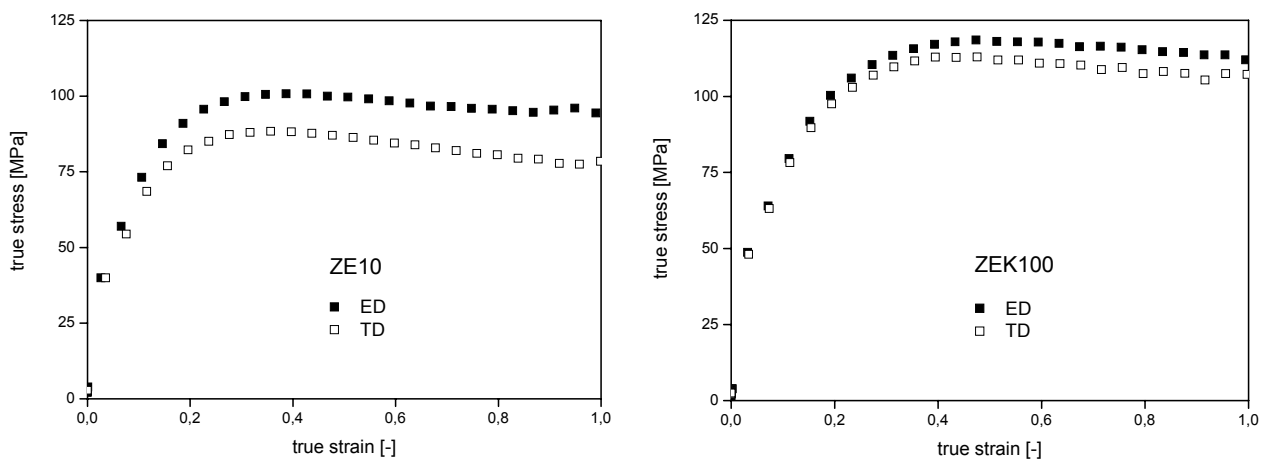


Figure 7.2: Compression test results: left ZE10, right ZEK100

After the peak stress, softening due to dynamic recrystallisation and recovery is observed as (Liu et al., 2007; Zhang et al., 2006) have reported. The variation of stress between ED and TD observed in ZE10 is more pronounced than the one for ZEK100 specimens. This is due to the fact that ZEK100 has a more homogeneous and finer microstructure.

7.3. Parameter identifications

The details of the parameter identification for the yield function were given in *Chapter 3*. Examples of the parameter identifications and the corresponding yield loci are presented here based on different assumptions. The nomenclature of the model parameters (i.e a_i and b_j), was adopted by considering these assumptions. Any acronym, for simplicity, starts with “CaBa”, indicating the parameters of Cazacu and Barlat yield criterion. As mentioned in *Chapter 3*, the evolution laws based on the exponential and polynomial functions were used. “Expo” stands for the exponential evolution, however, the polynomial evolution of the parameters are indicated by “Poly” in the nomenclature. The identification of model parameters was done with respect to the experimental results as mentioned before. The experimental results of the compression and tensile tests in ED and TD generate 4 main axes in the stress space. This quantity appears in the acronym representing the number of loading path. If the yield strength in shear obtained from the tensile test results is used in the parameter identifications, then it is mentioned with “ten” as an extension.

7.3.1. CaBaPoly4

Figure 7.3 shows the yield loci optimised with polynomial function labelled as *CaBaPoly4* together with the experimental results. The yield strength in shear was calculated from the yield stress obtained from the compression test in ED (see Equation (2.28)).

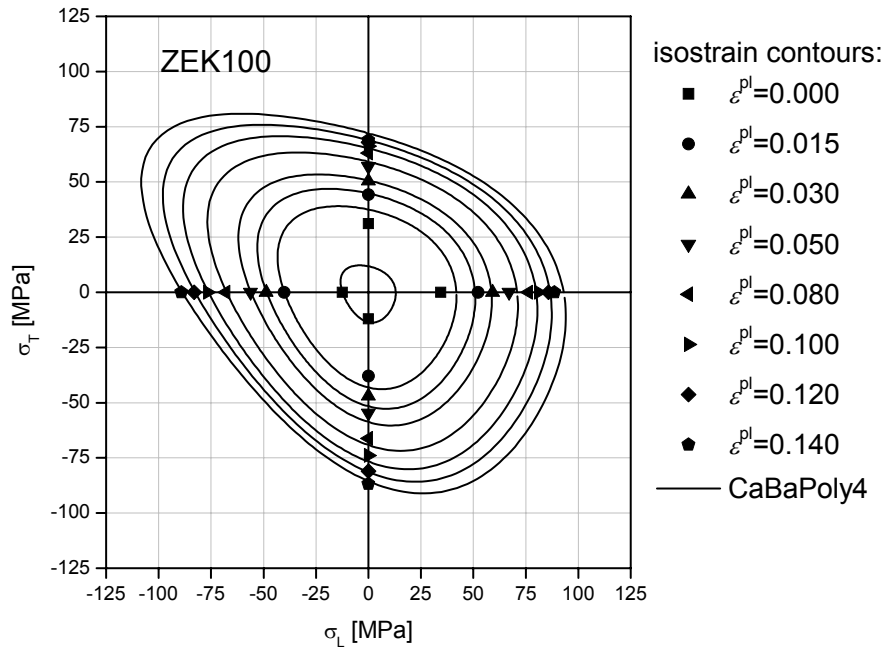


Figure 7.3: Optimised yield loci with parameters labelled as *CaBaPoly4* for ZEK100

The comparison of the functions for evolution of the yield surface during deformation which may occur in extrusion is plotted in Figure 7.4. Unlike the exponential functions, the polynomial functions do not saturate with respect to plastic strain. This does not allow for convergent extrusion simulations with the parameter set *CaBaPoly4*.

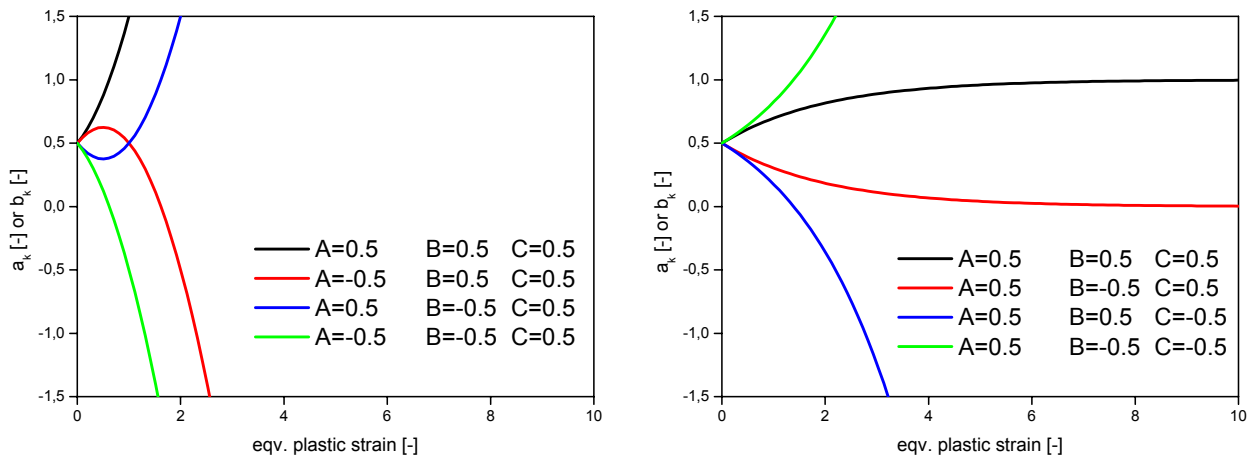


Figure 7.4: Comparison of the evolution functions: polynomial (left) and exponential functions (right)

7.3.2. CaBaExpo4ten

The optimised yield loci with the exponential evolution are shown in Figure 7.5. Unlike the yield loci shown in Figure 7.3, the isostrain contours are drawn by the yield strength in shear obtained

from the tensile test in ED only as given in Equation (2.27). Hence, better results with respect to the hardening in tension are obtained.

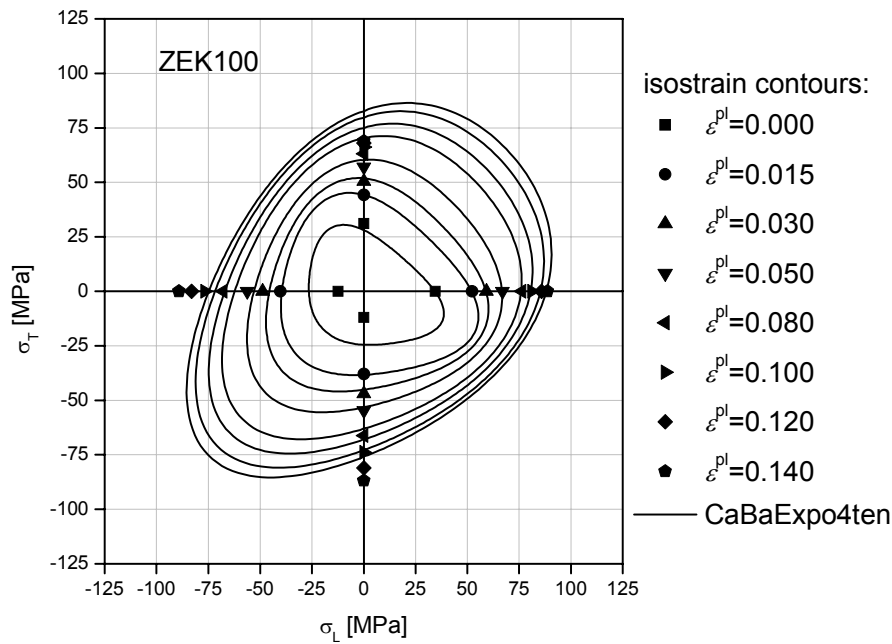


Figure 7.5: Optimised yield loci with parameters labelled as *CaBaExpo4ten* for ZEK100

The third quadrant in stress space is more important because the stress state during extrusion is mainly compressive. Besides this, the strain rate and temperature dependent yielding were characterised with the help of compression tests in *Chapter 6*. The simulation of extrusion trials with *CaBaExpo4ten* was consequently unsuccessful.

7.3.3. CaBaExpo2

It is difficult to meet the experimental results from the first isostrain values represented by square symbols in Figure 7.3 and Figure 7.5, because the genetic algorithm is forced to satisfy the constraints described in *Chapter 3* and the hardening in both tension and compression are quite different. An example of optimisation yield loci shown in Figure 7.6 is based only on the compression test results. Since the compression tests represent 2 main axes in the stress space and the exponential evolution was used, the parameters are called as *CaBaExpo2*. Figure 7.6 illustrates good agreements with the experimental data. In compression tests, there is no necking which limits uniform deformation as in the case of tensile tests. The yield loci for higher strains are shown in Figure 7.6.

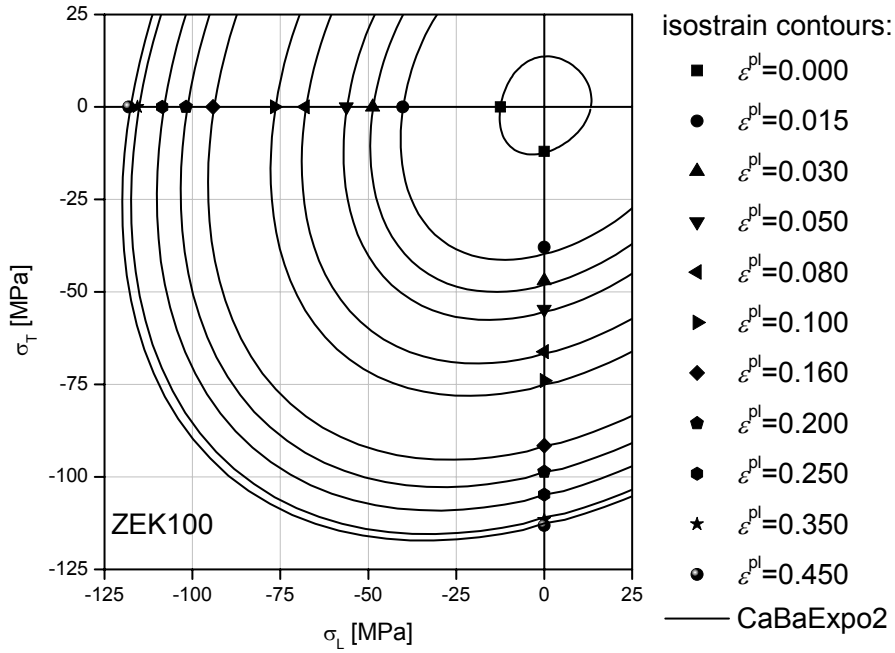


Figure 7.6: Optimised yield loci with parameters labelled as *CaBaExpo2* for ZEK100

7.3.4. CaBaExpo4

Figure 7.7 shows the yield loci drawn for ZE10 and ZEK100, respectively. The yield strength in shear was calculated from the compression test in ED. The respective set of model parameters is labelled as *CaBaExpo4* and used for the simulations of extrusion like *CaBaExpo2*. The shapes of yield loci in Figure 7.7 are different than the ones shown in Figure 7.6 since the tensile tests results were taken into account in the identification procedure. The simulation results with *CaBaExpo4* are presented later in *Chapter 8*, because of having more information on the experiments, hence being more realistic.

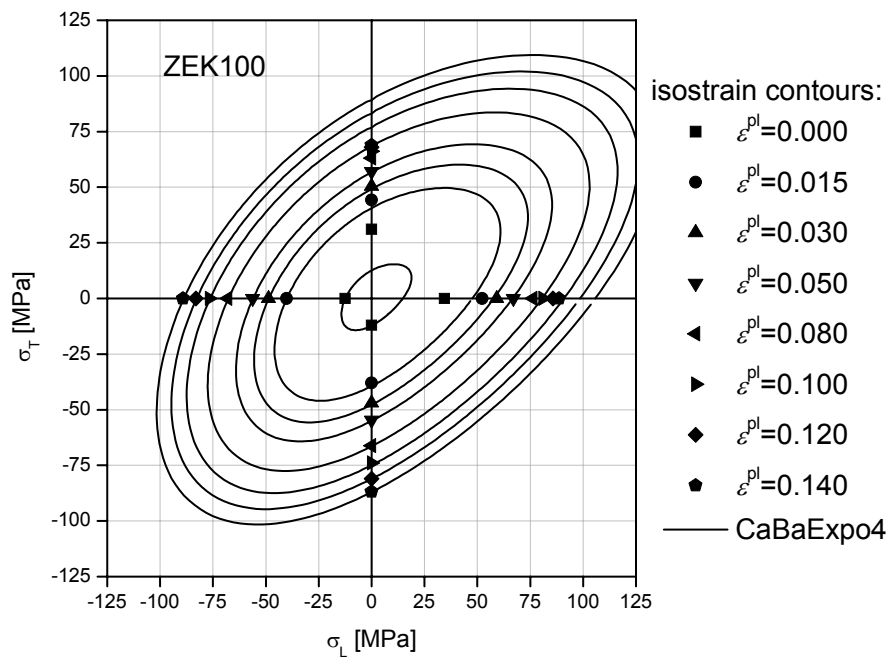
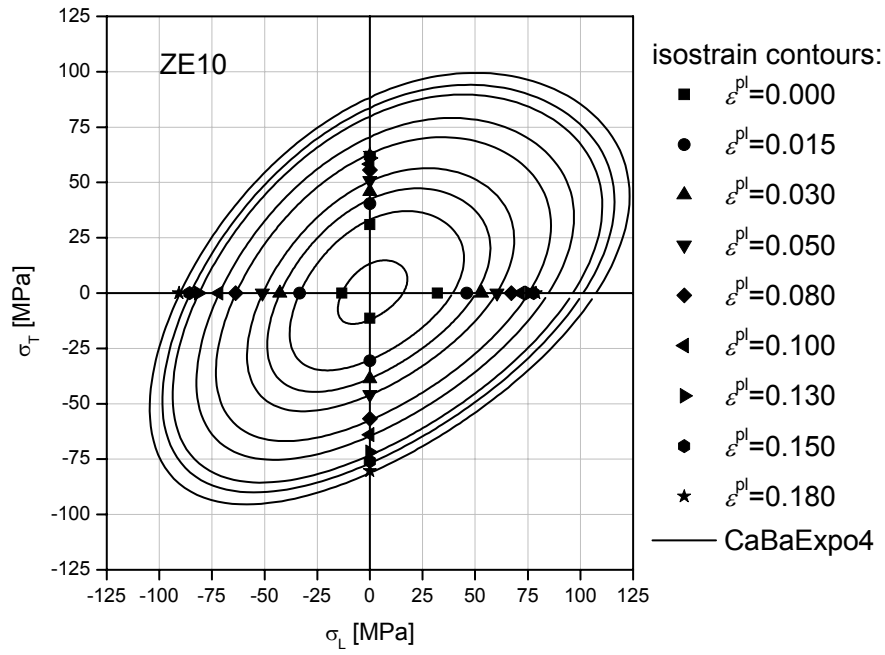


Figure 7.7: Optimised yield loci with parameters labelled as *CaBaExpo4* for ZE10 (top) and ZEK100 (bottom)

The corresponding parameters are given in the Table 7.1.

<i>ZE10</i>	a_1	a_2	a_3	b_1	b_2	b_3	b_4
A	0.65573	0.91849	0.56748	0.12685	0.47683	0.34511	0.16916
B	0.7118	0.76138	0.28211	0.5566	0.84393	0.1566	0.62522
C	0.9834	0.84685	0.37261	0.40517	0.67611	0.14484	0.36544

<i>ZEK100</i>	a_1	a_2	a_3	b_1	b_2	b_3	b_4
A	0.98064	0.98340	0.70129	0.03761	0.97996	0.19449	0.03490
B	0.57824	0.60743	0.32369	0.29932	0.63357	0.34510	0.02834
C	0.72570	0.78810	0.68276	0.24968	0.98679	0.15502	0.33420

Table 7.1: Optimised parameters *CaBaExpo4* for ZE10 and ZEK100

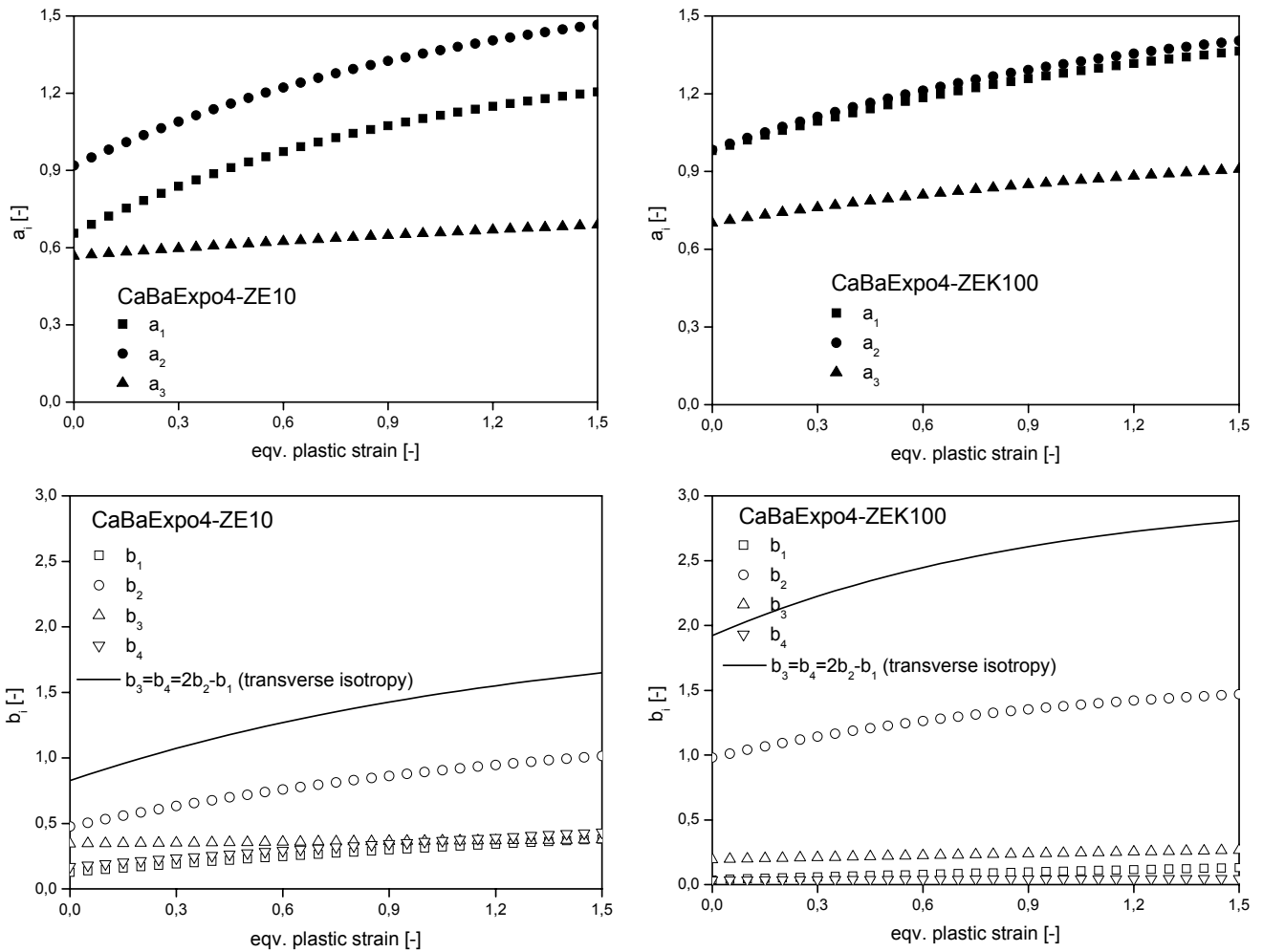


Figure 7.8: Evolution of the parameters: *CaBaExpo4* for ZE10 (left) and ZEK100 (right)

The evolution of the parameters can be seen in Figure 7.8. The respective sets were generated with the saturated exponential function drawn as a black line in Figure 7.4 which means all the parameters in the function, i.e. A_i , B_i and C_i , are assumed as positive. The difference between the transverse isotropy and plane stress assumptions on the yield function is also illustrated in Figure 7.8. The respective formulations were given in *Chapter 2*. The symmetry conditions in the transverse isotropy provide some restrictions on the parameters a_i and b_k as given in Equations (2.21) and (2.23), respectively. The restriction, $b_3 = b_4 = 2b_2 - b_1$, calculated from the parameters of *CaBaExpo4* identified with the plane stress assumption is plotted as a solid line in Figure 7.8. The values of b_3 and b_4 for both alloys are quite comparable to each other but not equal to $2b_2 - b_1$. Another restriction, $a_1 = a_2$, is satisfied only in the case of ZEK100. The rest of the restrictions are not possible to check because of being uncommon for both formulations.

7.4. Simulations

Simulations of tensile and compression tests were performed on ZE10 and ZEK100 billet materials by neglecting temperature and strain rate effect on deformation. The parameter set *CaBaExpo4* was used for the simulations. Due to the symmetry of the specimens, a quarter of the specimen was meshed with axisymmetric continuum elements having 4 nodes, CAX4R, for materials prepared from ED. Since the directions of the applied load and the yield stress coincide, anisotropic deformation in the simulations of ED is not crucial. On the other hand, the simulations performed on TD were executed on a mesh composed of 3D continuum elements with 8 nodes, C3D8R, where the symmetry boundary conditions were applied. The material properties used for the simulations can be seen in Table 6.1.

7.4.1. Tensile tests

The tensile test simulations were considered as displacement controlled. The displacement was applied to the upper edge of both geometries. The reaction forces acting on nodes where the displacement is applied were summed in order to get the resulting force. The stress was calculated with respect to initial cross sectional area. The simulation results for ZE10 and ZEK100 are plotted in Figure 7.9. In the beginning of the tensile test, there is a good agreement between the simulation and experimental results. However, this is not valid throughout the tensile tests due to the less accurate hardening behaviour in tension as seen in Figure 7.7 and the damage observed in the specimens. Failure of ductile metals is the result of micromechanical mechanisms, basically characterised by nucleation, growth and coalescence of voids or microcracks. The modelling of

ductile damage requires a theory of plasticity including internal damage quantity. This can be realised mainly via micromechanical models based on homogenisation by representative volume elements (e.g. (Gurson, 1975) and (Tvergaard and Needleman, 1984)) or via continuum damage mechanics postulating thermodynamics potentials (e.g. (Rousselier, 1987)). The softening observed in the experiments cannot be realised with the simulation presented here due to lack of any modelling issues concerning damage.

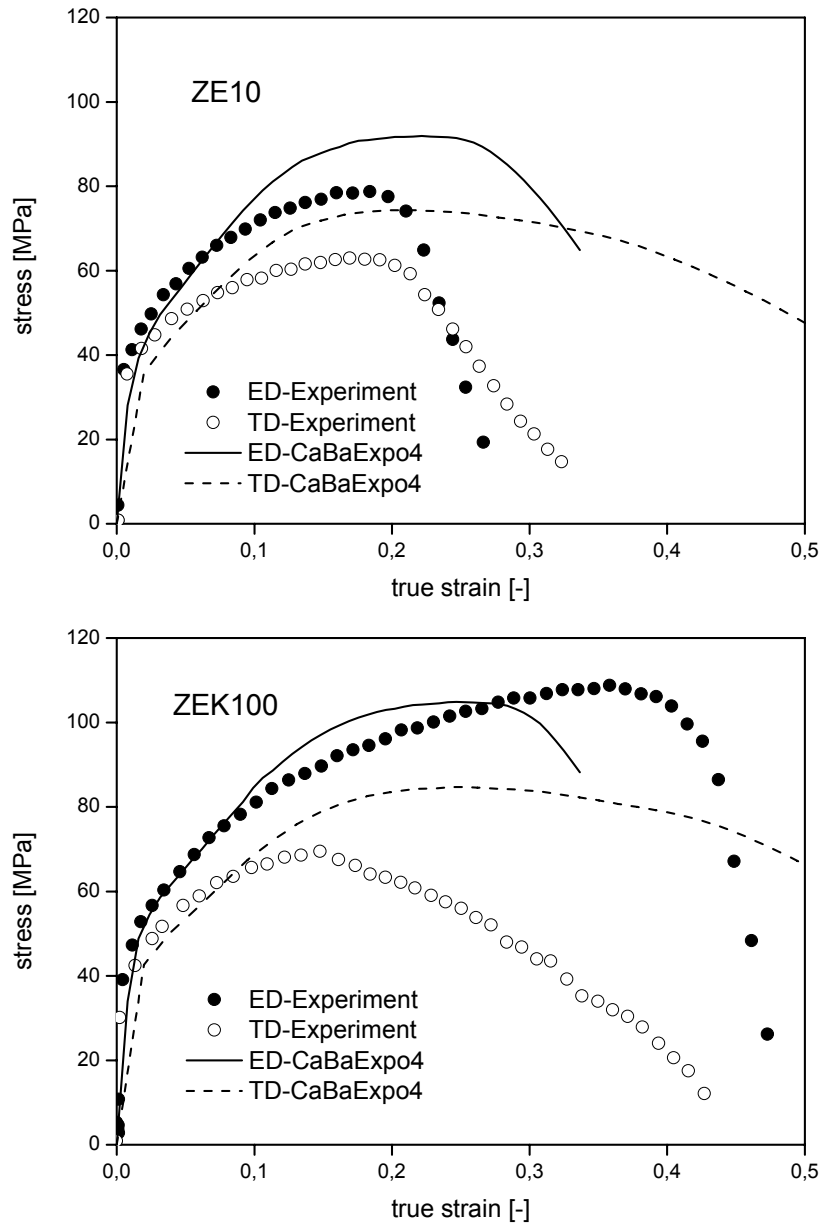


Figure 7.9: Simulation results of tensile tests performed with *CaBaExpo4* for ZE10 (top) and ZEK100 (bottom)

7.4.2. Compression tests

The simulation of compression tests were performed as described in *Chapter 6.3*. The simulation results obtained from billets of ZE10 and ZEK100 are illustrated in Figure 7.10. Unlike Figure 7.9, Figure 7.10 illustrates a better coincidence of simulations and experiments due to the better capture of hardening in compression than in tension as seen in Figure 7.7.

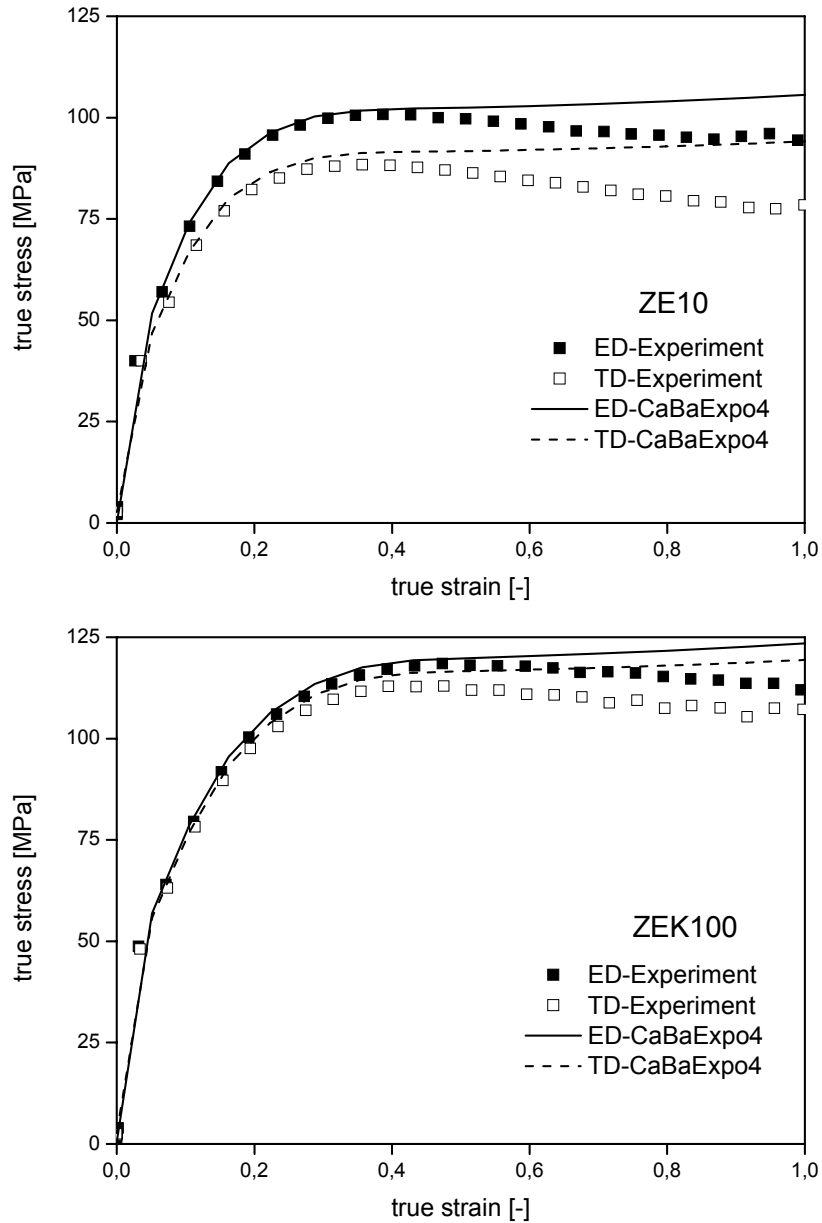


Figure 7.10: Simulation results of compression tests performed with *CaBaExpo4* for ZE10 (top) and ZEK100 (bottom)

For both cases, the predicted results are in good agreement with the experiments until the peak stress. Since the softening due to dynamic recrystallisation and recovery is not considered in the model, some deviations from the experiments are obviously present.

Chapter 8

Extrusion:

Experiments & Simulations

8.1. Introduction

Extrusion (Wagoner and Chenot, 2001) is a metal forming process in which a block of metal (billet) is forced to flow by compression through a die in order to produce profiles with a constant cross section. The main classification of extrusion processes is done with respect to direction of the metal flow, namely direct and indirect extrusion. In direct extrusion, the billet is placed in the container and pushed through the die by the ram pressure so that the direction of metal flow is in the same direction as the ram travels. In indirect extrusion, the die at the front end of the hollow stem moves relative to the container to produce metal flow opposite to the motion of the ram. Another classification of metal forming processes is performed based on temperature so that they are divided into 2 groups, hot and cold working, respectively. The hot working is carried out at a temperature higher than the recrystallisation temperature – the minimum temperature at which reformation of the crystals (i.e. recrystallisation) occurs. A crude estimate for a hot working temperature is that it should be greater than half of the melting point. Above the recrystallisation temperature, the kinetic

energy of atoms increases and therefore atoms are able to attach themselves to newly formed nuclei which begin to grow into crystals. This process continues until all the distorted crystals have been transformed. As a result, hot working results in grain refining (Dieter, 1988).

An undesirable output of the extrusion is the occurrence of hot cracking (known also as hot shortness). This surface defect is originated from incipient melting of material due to excessive temperature rise. Some studies in literature such as (Atwell and Barnett, 2007; Letzig et al., 2008) show that the phenomenon is extrusion speed, temperature and alloy dependent. The extrusion experiments in the present study were executed successfully without any surface defects.

8.2. Experiments

For each alloy, 3 billets were machined down to a diameter of 93 mm and a length of 300 mm for extrusion experiments. Hot indirect extrusion was carried out at a constant billet temperature of 300°C to produce round bars with a diameter of 17 mm from a container with 95 mm diameter.

Extrusion ratio, R , is defined as the ratio of initial cross sectional area of the billet, A_o , to the final cross section area, A_f :

$$R = \frac{A_o}{A_f}. \quad (8.1)$$

As a result, the geometry of billet and profile used in the experiments approximately corresponds to an extrusion ratio of 30:1.

Only the extrusion rate was varied using ram speeds of 0.5, 5.5 and 11 mm/s. This roughly corresponds to a profile speed of 1, 10 and 20 m/min since profile speed, v_p , is calculated by volume constancy, which means that the volume of the billet in the container is equal to the volume of the extruded material:

$$v_p = \frac{v_R A_o}{A_f}, \quad (8.2)$$

where v_R is the ram speed.

Figure 8.1 shows the applied force and the profile temperature during the whole extrusion experiments performed for both alloys.

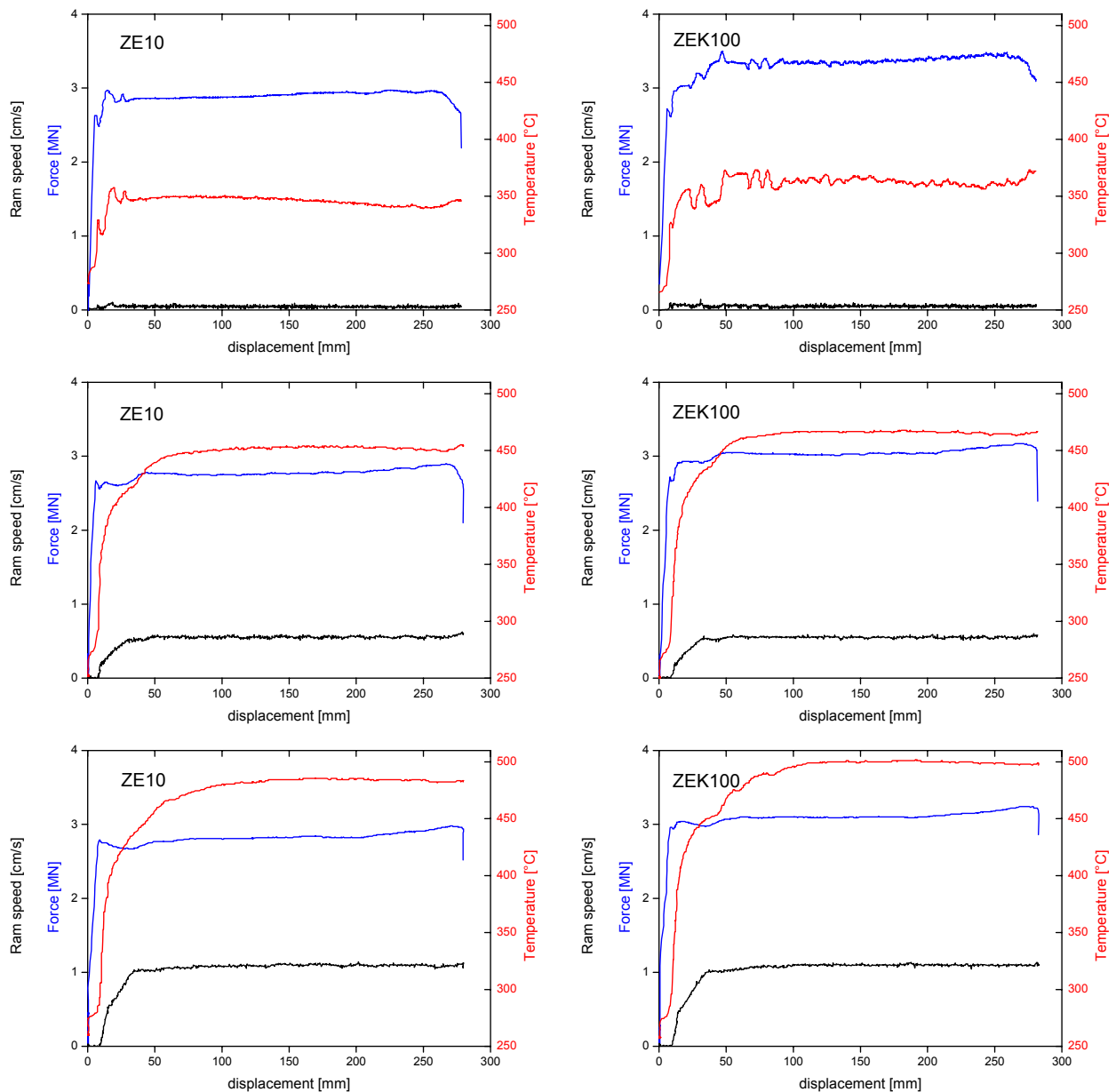


Figure 8.1: Experimental results of ZE10 and ZEK100 at different ram speeds

It is observed that there is an increase of the applied force up to the point where steady-state is reached. No pronounced peak pressure is observed. The die was equipped with a thermocouple at the inner surface so that the temperature of the passing profile could be measured. The profile temperature increases from the initial temperature to a steady-state equilibrium condition. In the beginning of the experiment, the thermocouple measures an arbitrary temperature since the die was not filled by the profile yet and the temperature was thus measured lower than 300°C.

The resulting force and temperature in steady-state are plotted in Figure 8.2. The temperature developed in extrusion increases with increasing ram speed. This is due to the fact that the strain rate is directly proportional to the ram speed and the magnitude of the generated heat is related with strain rate as given in Equation (4.3). Due to a finer microstructure of ZEK100 in comparison to ZE10, a higher force is observed for ZEK100 than for ZE10. Moreover, the applied force for both alloys first decreases with increasing ram speed due to predominant temperature softening and then increases slightly again because strain rate hardening is more pronounced than temperature softening.

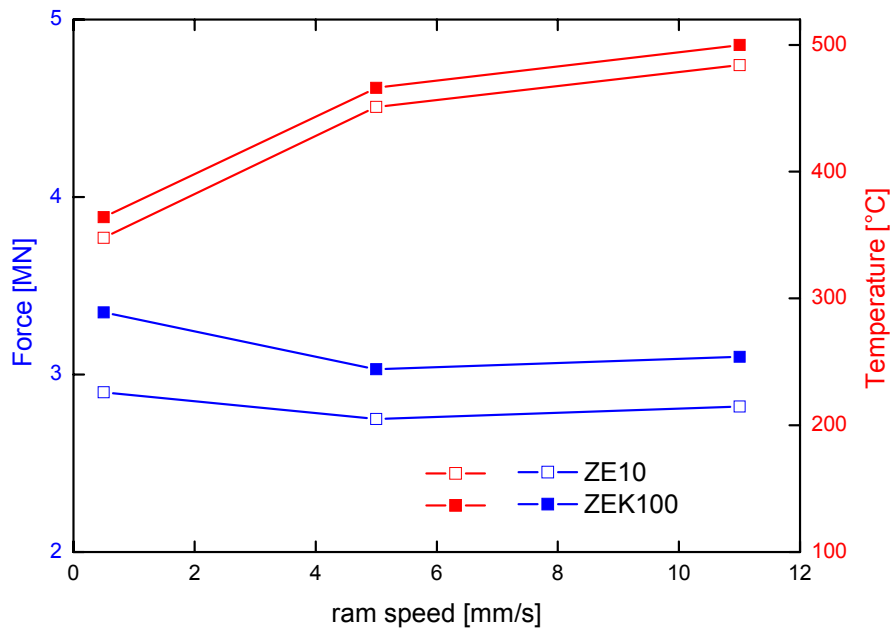
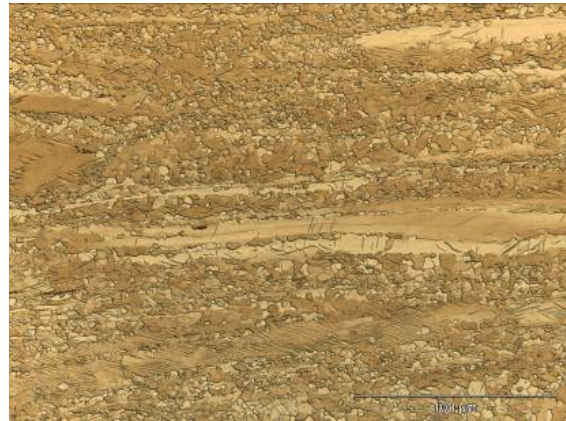


Figure 8.2: Summary of experimental extrusions for both alloys

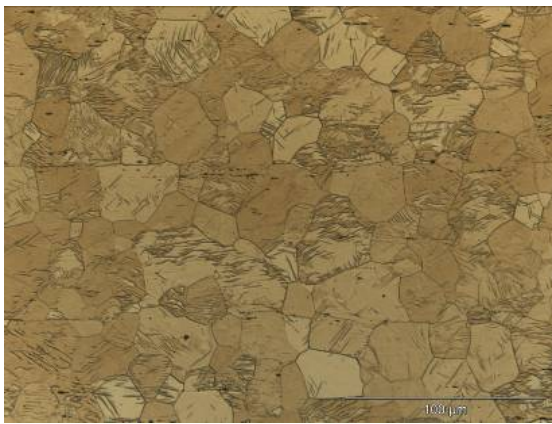
Micrographs taken from longitudinal sections of the profiles reveal the microstructures of the extruded profiles in Figure 8.3. The microstructures illustrate significantly smaller grains compared to the original cast billet as shown in Figure 6.3. The profiles extruded at the slowest profile speed of 1 m/min are partially recrystallised and show elongated structures in extrusion direction (horizontal). The characteristics of the cast microstructures are not visible any more at higher extrusion rates where well recrystallised microstructures are exposed.



ZE10 – 1m/min



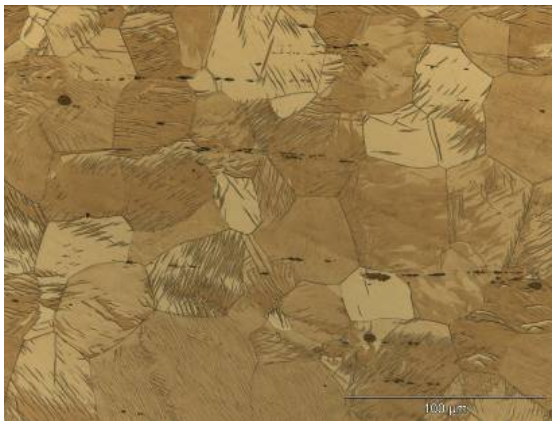
ZEK100 – 1m/min



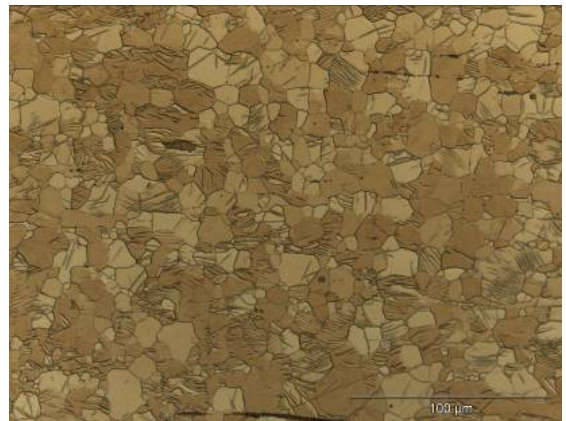
ZE10 – 10m/min



ZEK100 – 10m/min



ZE10 – 20m/min



ZEK100 – 20m/min

Figure 8.3: Micrographs of profiles obtained by different profile speeds

An increase of the average grain size determined using a computer aided linear intercept method is observed with increasing extrusion rate which results in higher temperature. The grain growth plotted in Figure 8.4 is significantly more pronounced for ZE10 than for ZEK100 which contains Zr

as a grain refinement agent. Therefore, the average grain sizes of ZEK100 profiles in all cases are found to be smaller than ZE10.

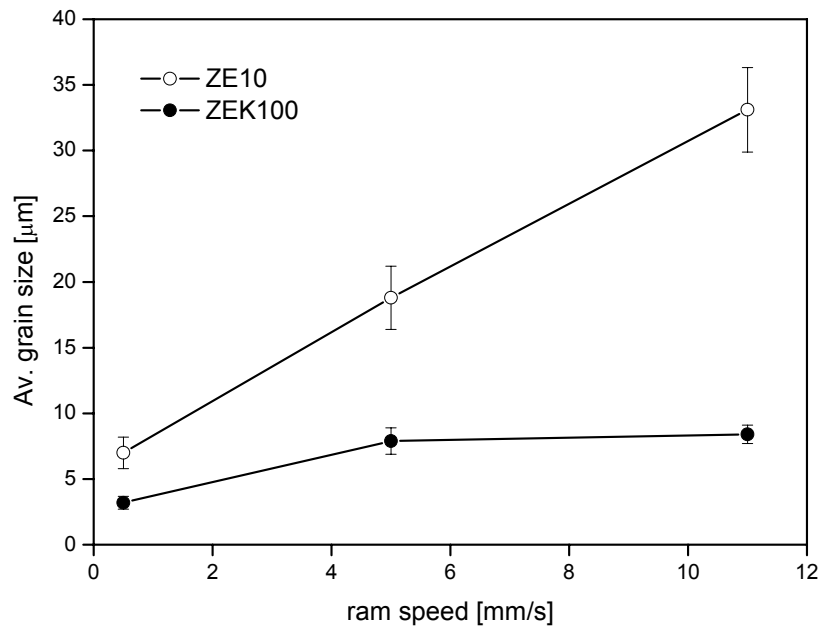


Figure 8.4: Average grain size of profiles obtained by different ram speeds

The microstructural development during the extrusion experiment becomes evident by investigating an extrusion remainder under optical microscopy. Figure 8.5 shows a macrograph from a longitudinal section of the remainder extruded at a ram speed of 5 mm/s. The microstructural changes as a result of metal flow are observed near the die outlet of the extruded profile.



Figure 8.5: Longitudinal section of the extrusion remainder (ZE10) at ram speed of 5 mm/s

8.3. Simulations

The extrusion remainder shows symmetry as seen in Figure 8.5 so that the representative mesh was generated with axisymmetric continuum elements having 4 nodes with reduced integration, CAX4R and CAX4RT namely, seen in Figure 8.6.

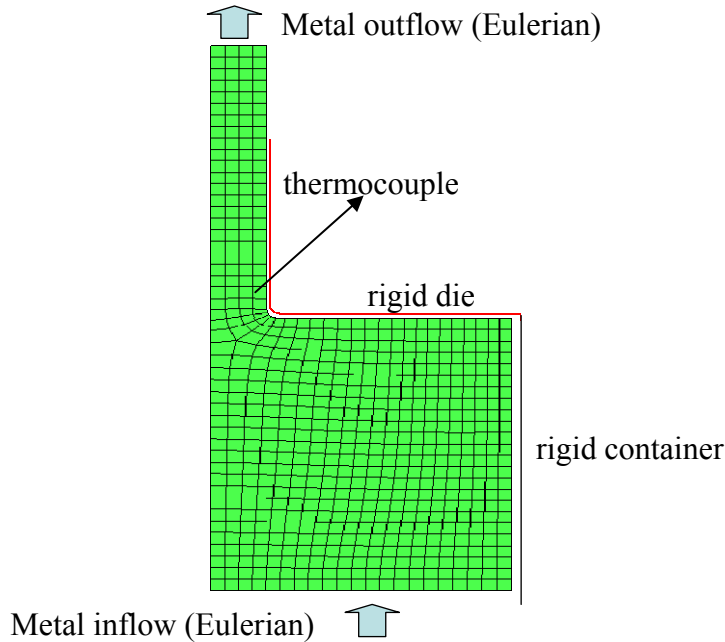


Figure 8.6: FE mesh used in the simulations

In the simulations, a so-called Arbitrary Lagrangian-Eulerian (ALE) (Abaqus, 2006a) formulation was used since a steady-state was reached in the experimental extrusion trials as seen in Figure 8.1. In the Lagrangian (material) description, a material point is focussed, whereas a stationary spatial reference frame is observed during deformation in the Eulerian (spatial) formulation (Khan and Huang, 1995). The combination of both limits forms ALE. This eliminates the problems of mesh distortions that can occur in a pure Lagrangian approach. The metal flow was considered via Eulerian boundary condition as seen in Figure 8.6. On the other hand, Lagrangian boundary conditions were applied to the die and the container. The tracer particles, which move with integration points in the FE mesh, are helpful to monitor the computed fields since the mesh in the Eulerian approach is spatially fixed and not attached to the material points.

The material properties for both alloys were given in Table 6.1. Beside this, Table 6.2 and Figure 6.7 show the model parameters regarding rate and temperature dependent yielding. The set of coefficients, i.e. a_k and b_j , labelled as *CaBaExpo4*, were used to describe the anisotropy and asymmetry (see Table 7.1). The set, labelled as *von Mises*, corresponds to von Mises plasticity.

In order to have reasonable computational costs, the container and the die were considered as analytical rigid surfaces, hence no deformation or temperature fields can be monitored on these surface. Since there is no relative displacement between the billet and the container, friction between the billet and the container does not exist in indirect extrusion. Therefore, the contact between the billet and the container was established without friction. The contact area with the die, on the other hand, was described with the Coulomb friction as described in *Chapter 6*. It is rather difficult to estimate the friction coefficient in Equation (6.7) during the extrusion process. The friction coefficient found in literature varies between 0.1 and 1 for different metallic materials (Lof, 2001), (Arentoft et al., 2000), (Lapovok et al., 2004). In this study, it was assumed as 0.5. However, the temperature predictions discussed below were performed by reducing the friction coefficient to 0.1, since the simulations with a friction coefficient of 0.5 under adiabatic assumptions, especially in the case of $\eta = 0.9$, predict a temperature of the region close to the die wall far above the melting temperature of magnesium alloys.

8.3.1. Parameter identifications

Since temperature and flow stress are coupled regardless of the type of analysis, the proper prediction of the temperature field is crucial. As explained before, calculations of temperature in two separately implemented VUMATs were handled with two different approaches, i.e. adiabatic and fully coupled temperature-displacement analysis, respectively. Parametric studies with von Mises plasticity were performed with both approaches in order to get proper temperature fields. The billets of ZEK100 were simulated till the half way of the ram displacement because of the achievement of steady-state conditions.

8.3.1.1. Adiabatic analysis

Parametric studies with different inelastic heat fractions as Equation (4.3) (i.e. $\eta = 0.5$, 0.7 and 0.9 respectively) under the assumption of adiabatic analysis were performed. The simulation results for different ram speeds are plotted in Figure 8.7. In the case of $v_p=1\text{m/min}$, all temperature predictions seem overestimated as compared with the experimental results. The corresponding resulting force, hence, appeared underestimated. This indicates that the billets were extruded so slowly that heat transfer took place. However, it is possible to predict temperature precisely with a proper selection of inelastic heat fraction for other extrusion trials. For example, $\eta = 0.7$ gives acceptable temperature predictions for the profile speed of 20m/min. This can not be applied for the profile

speed of 10 m/min because of the fact that the lower strain rate, the lower heat input. As a conclusion, adiabatic analysis is not a proper method to predict temperatures measured in extrusion experiments with a common inelastic heat fraction.

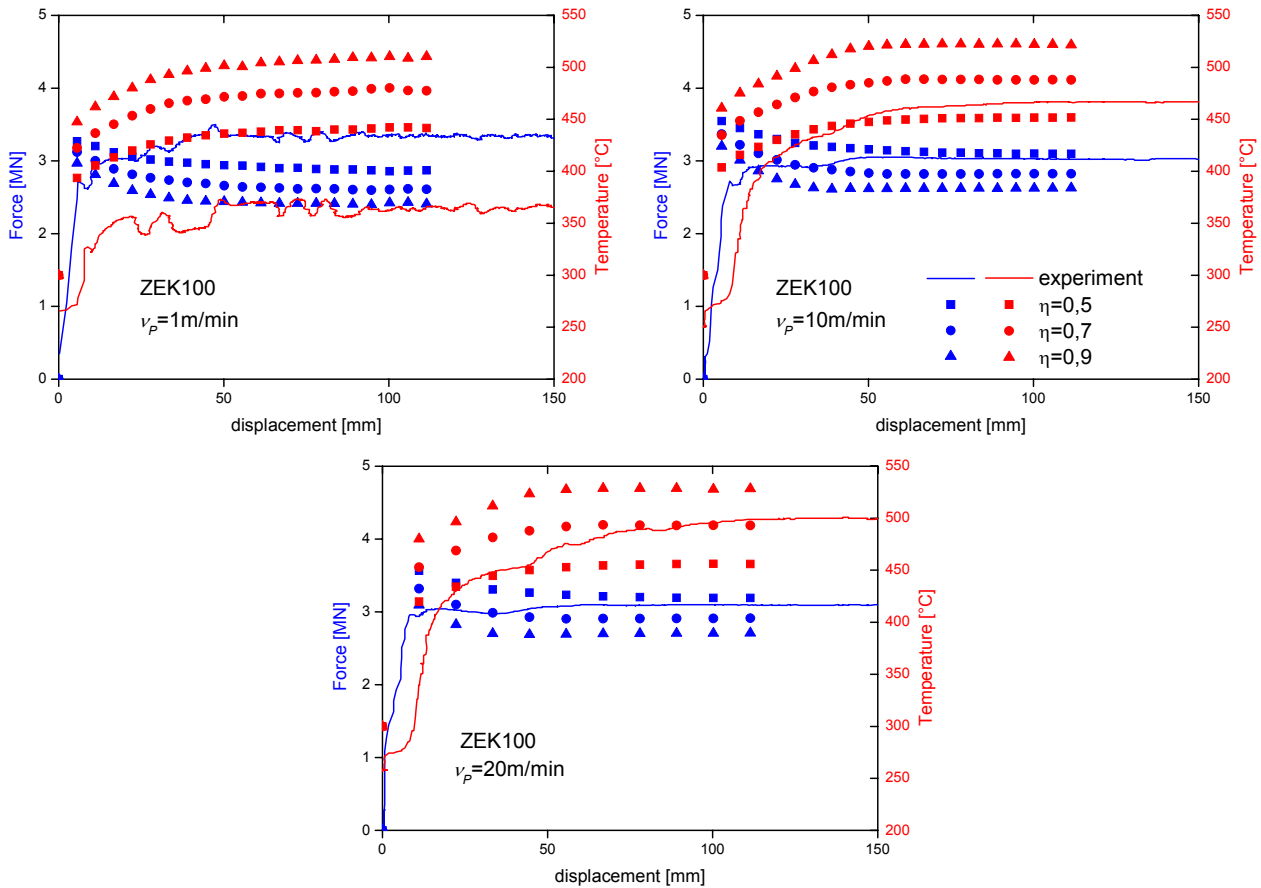


Figure 8.7: Effect of inelastic heat fractions under adiabatic assumption

8.3.1.2. Fully coupled temperature-displacement analysis

The heat flow out of the contact surfaces between the billet and the die and additionally between the billet and the container were applied. The inelastic heat coefficient was chosen as 0.9, which means that 90% of plastic deformation energy is transformed into heat. The parametric studies with fully coupled analysis were performed by setting different film coefficients of convection as described before (see Equation (4.5)).

Figure 8.8 shows the effect of film coefficients used in the simulations on temperature. Increasing the film coefficient results in lower temperature predictions and thus higher resulting force. Heat transfer conditions with film coefficient of 5 were selected to use for further simulations, providing reasonable results with a common parameter for all profile speeds.

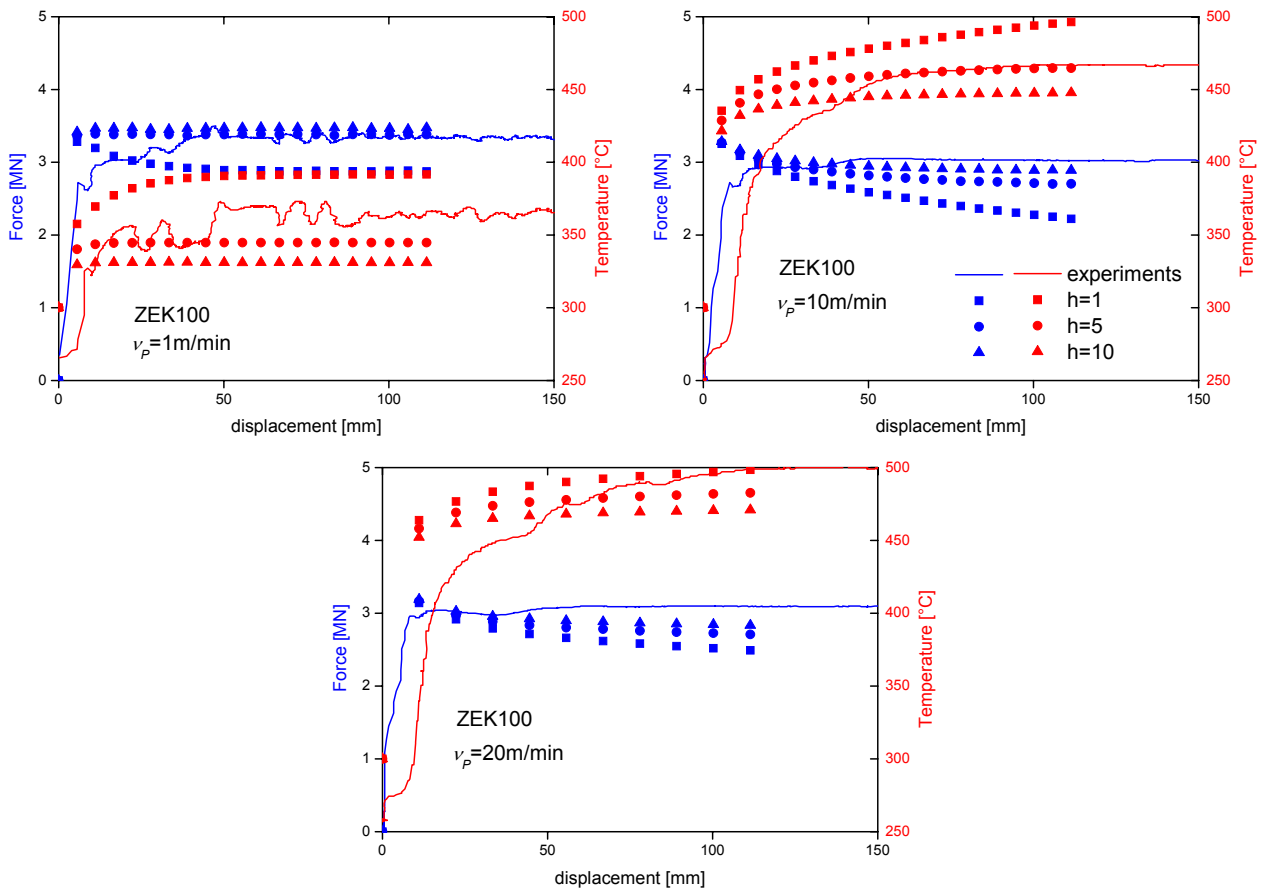


Figure 8.8: Effect of film coefficients used in fully coupled analysis

8.3.2. Prediction results

The material properties for both alloys, provided in Table 6.1, Table 6.2 and Figure 6.7, respectively, were used in the simulations. The deformation behaviour of the billet was characterised by the model parameters *CaBaExpo4* as described before. For comparison, von Mises plasticity was applied as well. The simulation results obtained with the sets *CaBaExpo4* and *von Mises* in comparison with the experimental results are plotted in Figure 8.9. Slight differences exist in the temperature predictions by both models. A better agreement with the experimental results in the case of force using the proposed model with set *CaBaExpo4* compared to von Mises model was obtained for the profile speeds of 10 and 20 m/min. On the other hand, the simulation with *CaBaExpo4* overestimates the reaction force for the profile speed of 1 m/min which causes partial recrystallisation as shown in Figure 8.3, since any effect of partial recrystallisation is not concerned in the proposed model.

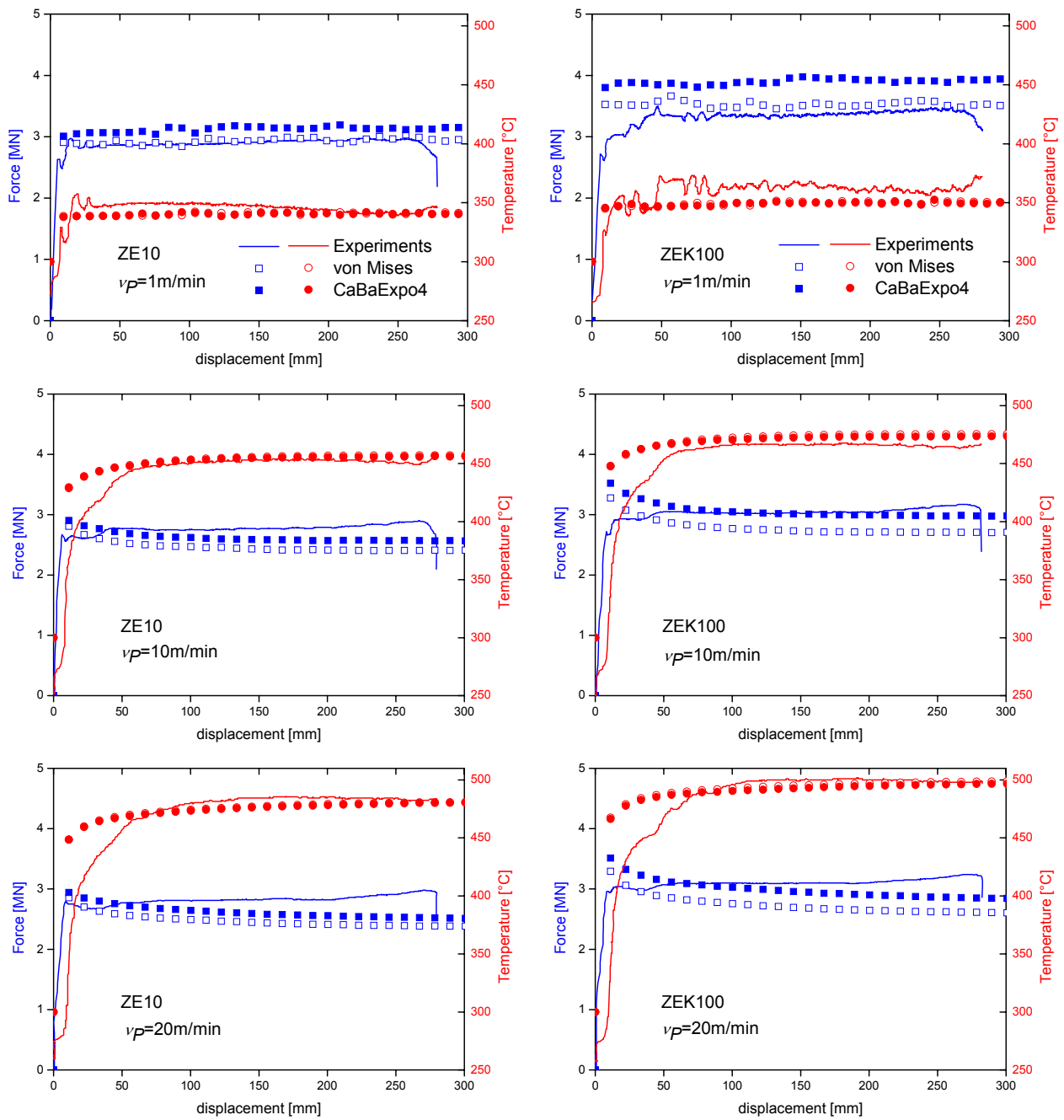
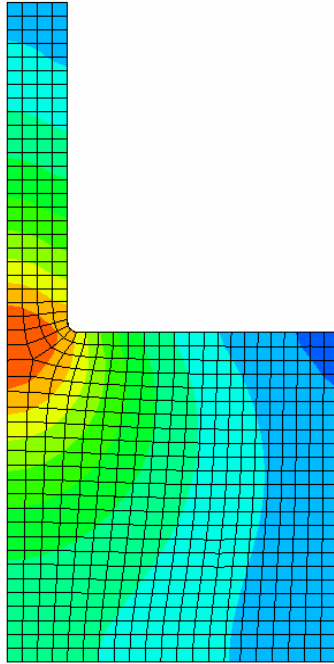
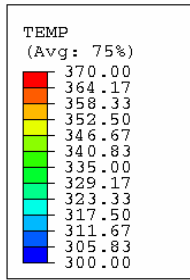
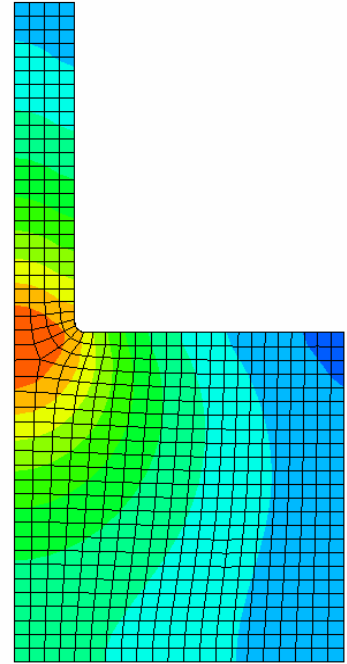
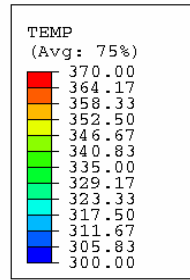


Figure 8.9: Simulation results with *von Mises* & *CaBaExpo4* in comparison with experiments

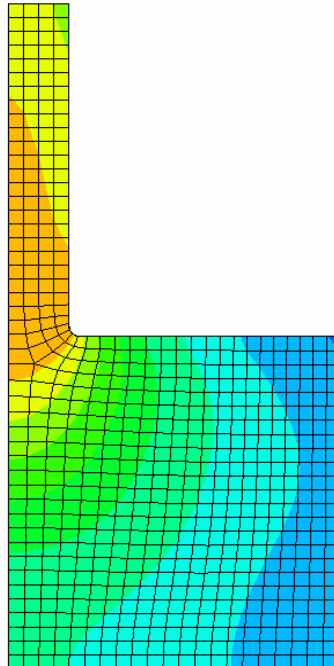
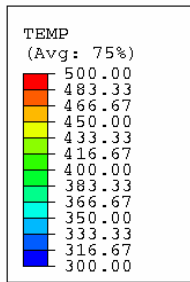
Figure 8.10 shows the distribution of the temperature with respect to profile speeds. The temperature distributions obtained by *von Mises* are not shown here due to being practically the same as the ones with *CaBaExpo4*.



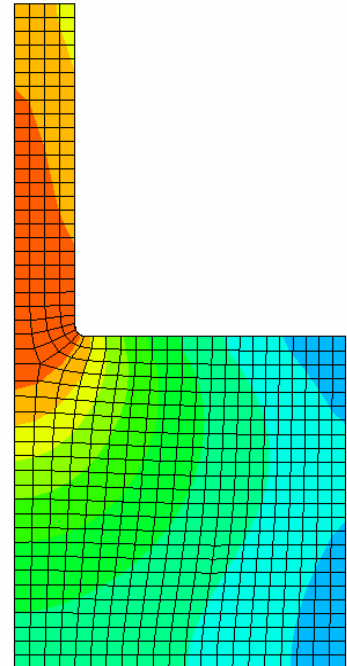
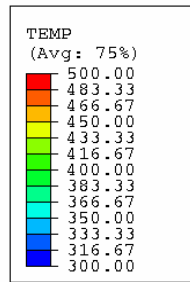
ZE10 – 1m/min



ZEK100 – 1m/min



ZE10 – 10m/min



ZEK100 – 10m/min

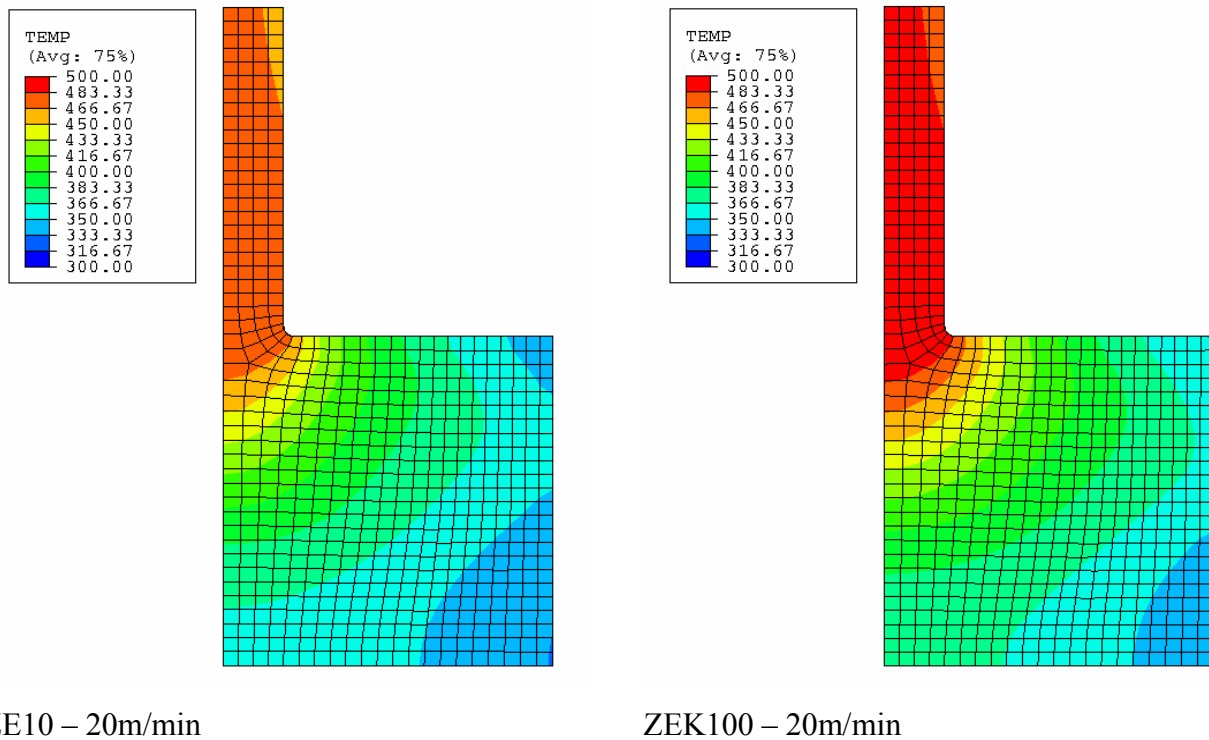
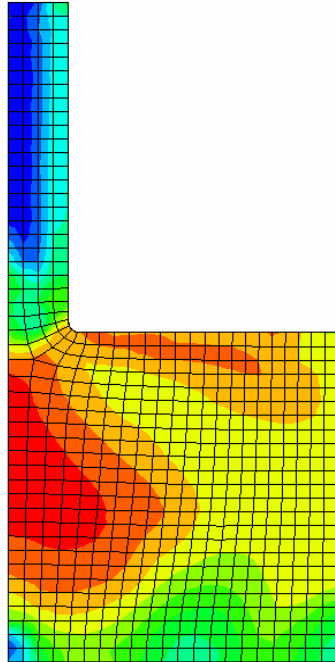
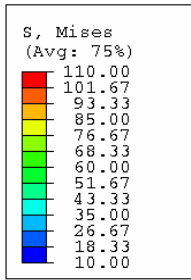


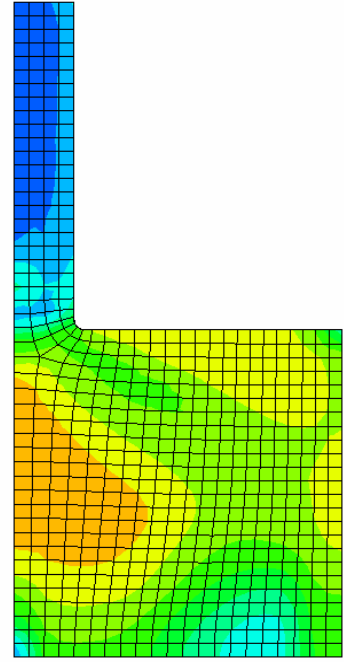
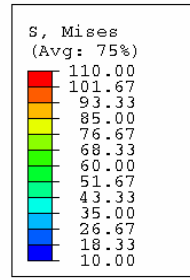
Figure 8.10: Temperature [°C] distributions with *CaBaExpo4* at profile speeds of 1, 10 and 20 m/min

The temperature developed during extrusion increases with increasing ram speed which is consistent with the experimental observations. For all cases, the highest temperature is located at the die opening where large deformation occurs. On the other hand, the heat transfer in the region close to the container causes cooling down of the extrudates.

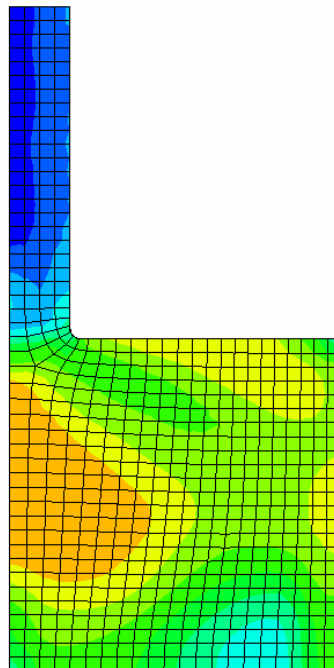
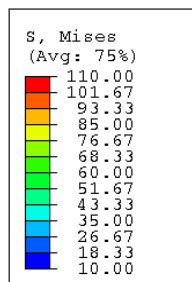
As the temperature distributions are qualitatively identical for the two alloys as seen in Figure 8.10, the following figures present only the result of ZE10. The von Mises equivalent stress distributions in ZE10 extrusion remainders are illustrated in Figure 8.11. The distributions for all trials are qualitatively similar. However, the remainder extruded with the profile speed of 1 m/min shows the most red-coloured regimes corresponding to the highest stress values due to the minimum temperature rise. The maximum stress is observed in the middle of the billet by the die opening. The region close to the container wall perpendicular to the extrusion direction experiences higher stress due to the presence of friction. The stresses occurring in the profiles, however, are small since there is no further deformation taken place after the die.



ZE10 – 1m/min



ZE10 – 10m/min



ZE10 – 20m/min

Figure 8.11: von Mises equivalent stress [MPa] distributions ZE10 with *CaBaExpo4* at profile speeds of 1, 10 and 20 m/min

Figure 8.12 shows the velocity distributions of ZEK100. Homogenous distributions of the velocities in the profiles with $v_p=10$ and 20 m/min indicate that the profiles are extruded at constant speeds which was traced in Figure 8.1, as well.

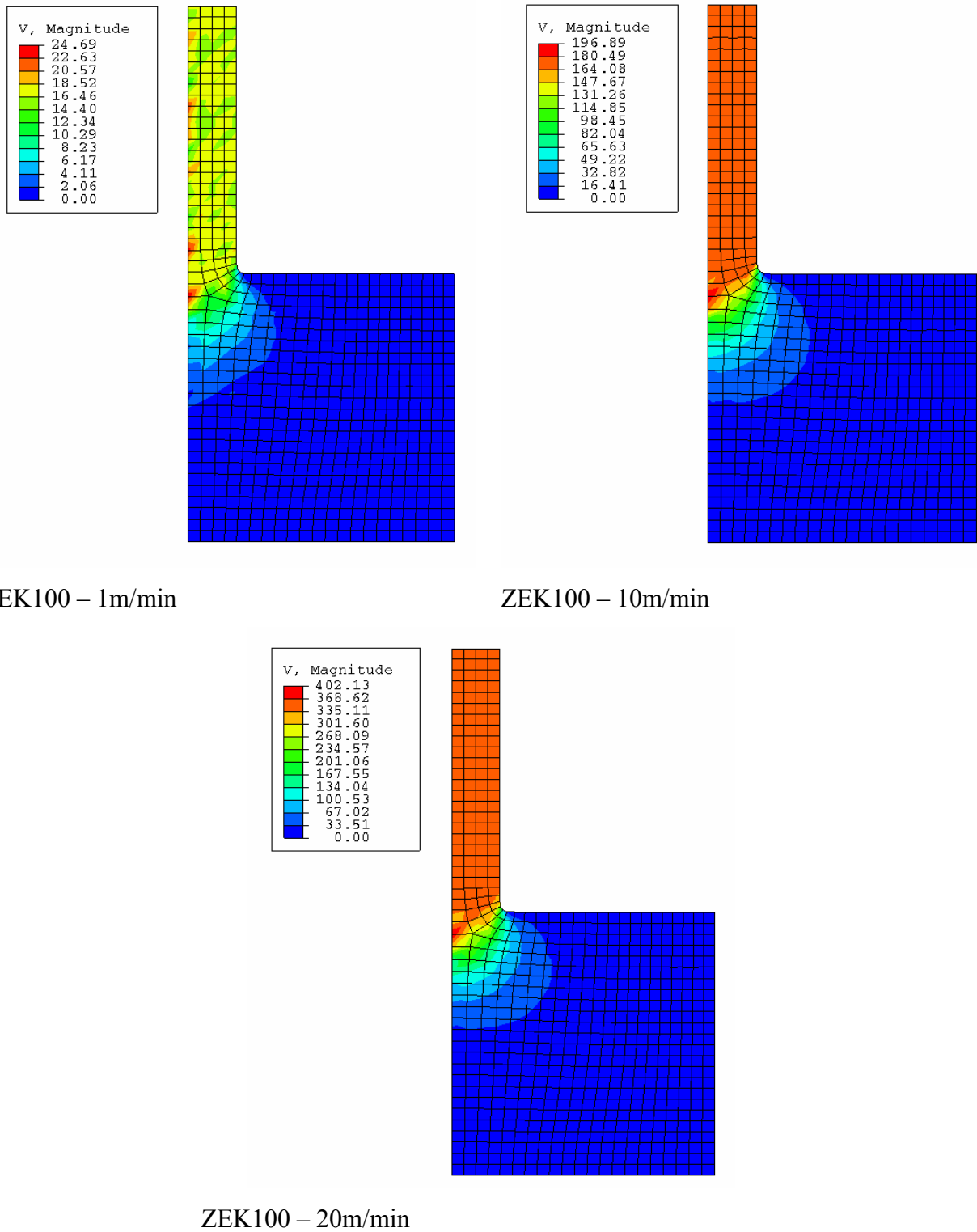


Figure 8.12: Velocity [mm/s] distributions ZEK100 with *CaBaExpo4* at profile speeds of 1, 10 and 20 m/min

Flow prediction in ZE10 billets extruded with 20 m/min as profile speed is demonstrated in Figure 8.13 together with the metallograph of the corresponding extrusion remainder. The arrows indicate the direction of the metal flow during the extrusion. The size of the arrows is assigned to their magnitude. The observed and predicted metal flow patterns are qualitatively similar.

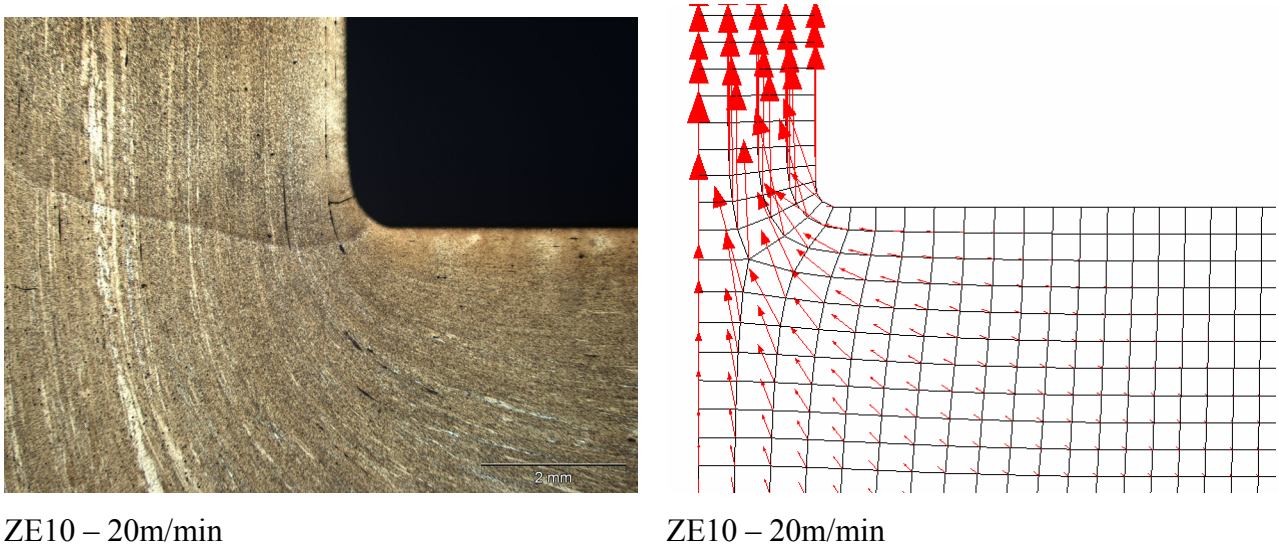


Figure 8.13: Flow predictions of ZE10 with *CaBaExpo4* at profile speed of 20 m/min with the corresponding metallographic examination

Figure 8.14 shows the metal flow during the extrusion with the help of tracer particles seen at different ram displacements.

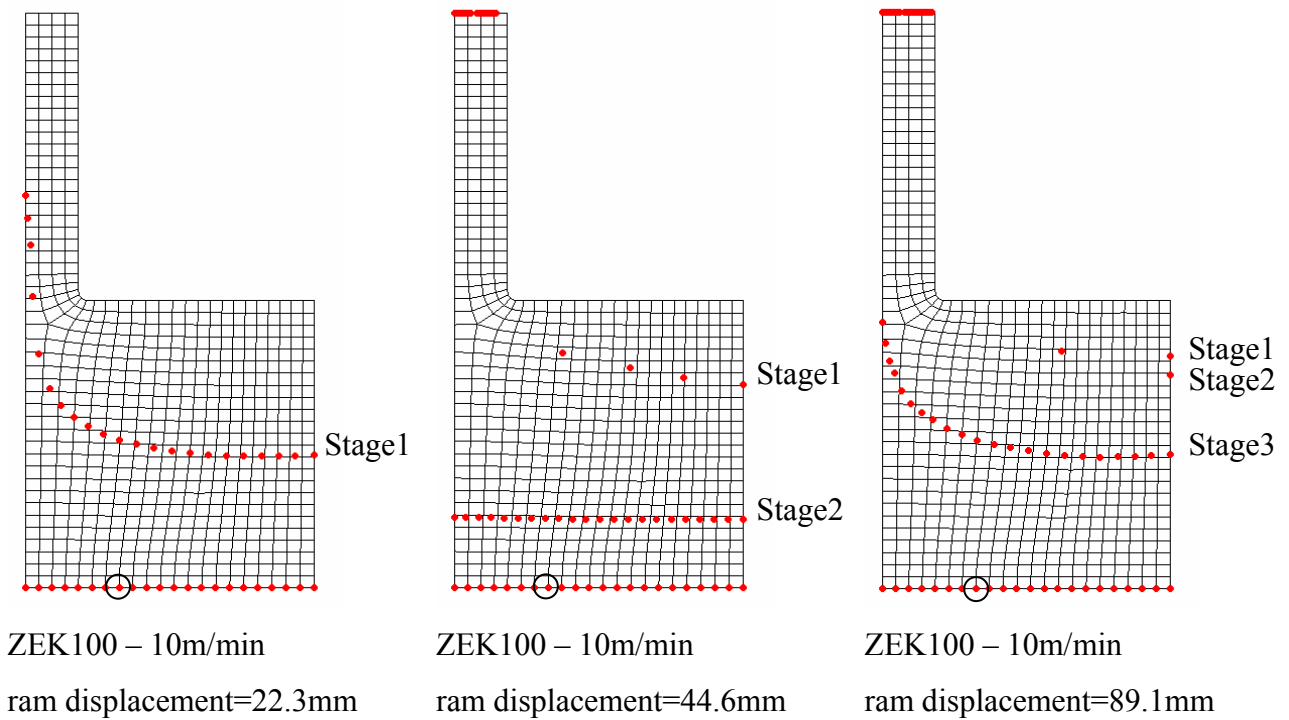


Figure 8.14: Flow predictions ZEK100 by tracer particles with *CaBaExpo4* at profile speed of 10 m/min

As mentioned before, the tracer particles follow the material points and hence visualise the material flow. The trajectory of the tracer particles was assigned as emission in 10 periodic stages. Some of the tracer particles from Stage 1 leave the mesh at 44.6 mm where the tracer particles belonging to Stage 2 are already emitted and thus visible as seen in Figure 8.14. Some of the tracer particles especially near to the container form the dead metal zone as illustrated in Figure 8.14.

The tracer particles can be also used for monitoring the predicted fields such as temperature. Figure 8.15 shows the response coming from one distinct tracer circled in Figure 8.14 with respect to its emission stages.

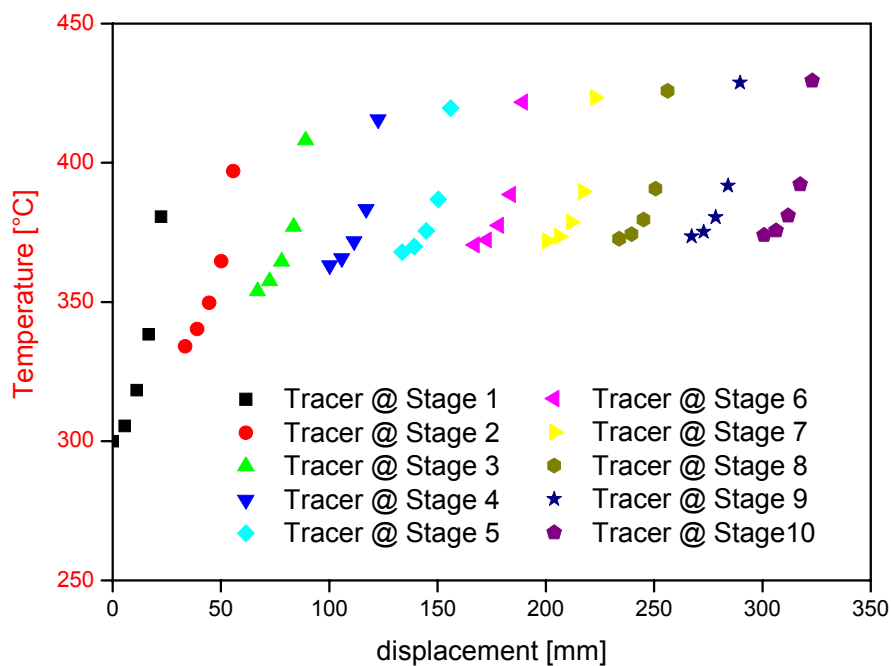


Figure 8.15: Temperature predictions of tracer particles of ZEK100 with *CaBaExpo4* at profile speed of 10 m/min

The temperature prediction is monitored in Figure 8.15 until the tracers from different stages leave the mesh. Although the initial location of the particles emitted in the mesh is the same for all stages, the initial temperatures of these particles increase because of the difference in their emission time. Since the particles become hotter since they approach the die, the temperature of each particle increases during the extrusion simulation.

Chapter 9

Summary & Conclusion

Magnesium alloys are strong candidates to cover a great demand in transportation industry for reduction of weight owing to low density. Wrought magnesium products are especially preferred due to their enhanced mechanical properties over cast parts. An example of manufacturing method is extrusion where temperature and strain rate play important roles on product quality. Magnesium alloys show unusual mechanical behaviour such as deformation anisotropy and asymmetry in tension and compression. In order to estimate metal flow behaviour of magnesium alloys during extrusion, a proper phenomenological model was proposed. The modified version of the Cazacu and Barlat model accounting for strain rate hardening and temperature dependent yielding was described in *Chapter 2*. The details of the parameter identification for the yield function were given in *Chapter 3*. The temperature calculations and the implementations of the corresponding model for adiabatic and fully coupled thermo-mechanical analyses were covered in *Chapter 4* and *Chapter 5*, respectively.

Chapter 6 deals with characterisation of billets by compression test, which is a common test for measuring the flow stress for metal working applications. Compression tests were executed to describe material behaviour with respect to strain rate and temperature. ZEK100 shows higher strength due to its finer microstructure. Increasing test temperature under a constant strain rate leads to thermal softening. On the other hand, an increase in strain rate under a constant temperature results in hardening. The rate and temperature dependencies of ZE10 and ZEK100 magnesium alloys were captured numerically with the help of simulation of compression tests. Adiabatic and fully coupled analyses provide very similar results because the compression tests were carried out so fast that heat transfer was not significant. It was found that the strain rate dependency depends on temperature. As a result, the model parameters accounting for rate dependency were identified with a variation of temperature to capture the overall behaviour observed in the experiments.

The anisotropy/asymmetry in yielding was quantified by tensile and compression tests of specimens as-cast from different directions, i.e. ED and TD, as described in *Chapter 7*. The experimental results show a variation of yielding behaviour in tension and compression with respect to loading directions. The identification of model parameters accounting for the anisotropy and asymmetry in yielding was done with respect to the experimental results. Since it is not possible to identify the model parameters of a yield potential for a transverse isotropic material with the help of experiments providing lack of information on the symmetry conditions as given in *Chapter 2*, the yield function was assumed as plane stress case. The model parameters were identified by a genetic algorithm satisfying the constraints such as convexity as described in *Chapter 3*. The set of parameters having the minimum error with respect to the experimental results was assigned as the optimised solution. The hardening of the alloys was defined with two different evolution laws, the exponential and polynomial functions, respectively. The hardening with the saturating exponential function provides better results in the extrusion simulations.

The information obtained from different means of the material characterisation was taken as input for simulations of extrusion experiments. The experiments and simulations of indirect extrusion of ZE10 and ZEK100 billets were presented in *Chapter 8*. The extrusion trials of ZE10 and ZEK100 show steady state. Increase in ram speed results in higher temperature. It is observed that a competition between temperature softening and strain rate hardening on force takes place. Arbitrary Lagrangian-Eulerian formulation was used in the simulations. The metal flow was considered via Eulerian boundary condition. On the other hand, Lagrangian boundary conditions were applied to the die and the container. The heat flow out of the contact surfaces between the billet and the die

and additionally between the billet and the container were applied to predict temperature measured by the thermocouple located in the die. Due to the symmetry of profiles manufactured in extrusion trials, the representative mesh was generated with axisymmetric continuum elements. Adiabatic analysis was not a proper method to predict the temperature measured in the extrusion experiments with a common inelastic heat fraction. On the other hand, the temperature predictions by fully coupled analysis demonstrated more better results with a common heat transfer parameter for all profile speeds. The simulations of extrusion with the proposed model provide a better agreement with experiments than von Mises yield criterion. The results of the approach adopted in this study appeared to be successful showing promising predictions of the experiments and thus may be used for other hcp metals rather than magnesium.

It would be of a great interest for a future work to improve the proposed model to account for dynamic recrystallisation (DRX), since the results indicate their importance on deformation behaviour. Consequently, this would allow predicting the microstructures of extruded profiles and hence permit more understanding of the mechanisms observed in magnesium alloys during extrusion process. The empirical relationships between microstructural features (e.g. grain size) and processing parameters (e.g. temperature and strain rate) are established by analysing the compression test results with so-called Zener-Hollomon parameter (Zener and Hollomon, 1944). This approach is recently extended to some magnesium alloys (Lee et al., 2007; Liu et al., 2008). However, modelling of DRX in conjunction with anisotropy is not realised in literature at all.

Another crucial aspect to be considered is to improve the identification of parameters for the yield potential. Torsion test results can be utilised as an additional source of input to the optimisation procedure because this material characterisation method provides a high extent of information as the deformation behaviour with respect to strain. Some contributions such as (Spigarelli et al., 2007) show the importance of the torsion test executed on specimens of AZ31 magnesium alloy. Instead of using experimental results, the model parameters can be calibrated referring to computed biaxial test simulations based on crystal plasticity models (e.g. (Graff, 2007)). The computational effort to fit the numerous material parameters such as activity of different deformation modes required by the micromechanical modelling would limit this approach.

References

- Abaqus, 2006a. ABAQUS Analysis User's Manual.
- Abaqus, 2006b. ABAQUS User Subroutines Reference Manual.
- Arentoft, M., Gronostajski, Z., Niechajowicz, A. and Wanheim, T., 2000. Physical and mathematical modelling of extrusion processes. *Journal of Materials Processing Technology*, 106: 2-7.
- Atwell, D.L. and Barnett, M.R., 2007. Extrusion Limits of Magnesium Alloys. *Metallurgical and Materials Transactions A*, 38A: 3032-3041.
- Barlat, F., Lege, D.J. and Brem, J.C., 1991. A six-component yield function for anisotropic materials. *International Journal of Plasticity*, 7(7): 693-712.
- Barlat, F. et al., 1997. Yield function development for aluminum alloy sheets. *J. Mech. Phys. Solids*, 45: 1727-1763.
- Barnett, M.R., 2007a. Twinning and the ductility of magnesium alloys: Part I: "Tension" twins. *Materials Science and Engineering: A*, 464(1-2): 1-7.
- Barnett, M.R., 2007b. Twinning and the ductility of magnesium alloys: Part II. "Contraction" twins. *Materials Science and Engineering: A*, 464(1-2): 8-16.
- Bettles, C.J. and Gibson, M.A., 2005. Current wrought magnesium alloys: strengths and weaknesses. *Journal of the Minerals, Metals and Materials Society*, 57(5): 46-49.
- Bohlen, J., Nürnberg, M.R., Senn, J.W., Letzig, D. and Agnew, S.R., 2007. The texture and anisotropy of magnesium–zinc–rare earth alloy sheets. *Acta Materialia*, 55: 2101-2112.
- Bron, F. and Besson, J., 2004. A yield function for anisotropic materials: Application to aluminium alloys. *Int. J. Plast.*, 20(4-5): 937-963.
- Burth, K. and Brocks, W., 1992. *Plastizität. Grundlagen und Anwendungen fuer Ingenieure*. Braunschweig - Wiesbaden, Vieweg.
- Cazacu, O. and Barlat, F., 2004. A criterion for description of anisotropy and yield differential effects in pressure-insensitive metals. *International Journal of Plasticity*, 20(11): 2027-2045.
- Cowper, G.R. and Symonds, P.S., 1957. Strain hardening and strain-rate effects in the impact loading of cantilever beams, Brown University.
- Dieter, G.E., 1988. *Mechanical Metallurgy*. McGraw-Hill.

- Drucker, D.C., 1949. Relation of experiments to mathematical theories of plasticity. *J. Appl. Mech.*: 349-357.
- Drucker, D.C., 1964. On the postulate of stability of material in the mechanics of continua. *Journal de Mécanique*, 3(2): 235-249.
- Ertürk, S., Steglich, D., Bohlen, J., Letzig, D. and Brocks, W., 2008. Modelling and Simulation of Extrusion of Magnesium Alloys. *International Journal of Material Forming*.
- Ertürk, S., Steglich, D., Bohlen, J., Letzig, D. and Brocks, W., 2009. Thermo-mechanical Modelling of Indirect Extrusion Process for Magnesium Alloys *International Journal of Material Forming*.
- Graff, S., 2007. *Micromechanical Modeling of Deformation in hcp Metals*, Technische Universität, Berlin, D.
- Graff, S., Brocks, W. and Steglich, D., 2007. Yielding of magnesium: From single crystal to polycrystalline aggregates. *International Journal of Plasticity*, 23(12): 1957-1978.
- Gurson, A.L., 1975. *Plastic flow and fracture behaviour of ductile materials incorporating void nucleation, growth and interaction*, Brown University.
- Hill, R., 1948. A theory of the yielding and plastic flow of anisotropic metals. *Proc. Roy. Soc. London A*, 193: 281-297.
- Hill, R., 1990. Constitutive modelling of orthotropic plasticity in sheet metals. *J. Mech. Phys. Solids*, 38: 405-417.
- Holland, J.H., 1992. *Adaptation in Natural and Artificial Systems*. MIT Press, MA.
- Hosford, W.F., 1972. Generalized Isotropic Yield Criterion. *Journal of Applied Mechanics*, 39(2): 607-609.
- Hosford, W.F., 1993. *The Mechanics of Crystals and Textured Polycrystals*. Oxford University Press.
- Hosford, W.F., 2005. *Mechanical Behavior of Materials*. Cambridge University Press.
- Hossain, F., 2007. *Optimisation of yield surfaces for Magnesium*, TU Braunschweig.
- Johnson, G.R. and Cook, W.H., 1983. A constitutive model and data for metals subjected to large strains, high strain rates and high temperatures. *Proc. 7th International Symposium on Ballistics*: 541–547.
- Johnson, G.R. and Cook, W.H., 1985. Fracture Characteristics of Three Metals Subjected to Various Strains, Strain rates, Temperatures and Pressures. *Engineering Fracture Mechanics*, 21(1): 31–48.
- Kainer, K.U., 2003. *Magnesium alloys and their applications*. Wiley-VCH, Weinheim.

- Kaiser, F. et al., 2003. Influence of Rolling Conditions on the Microstructure and Mechanical Properties of Magnesium Sheet AZ31. *Advanced Engineering Materials*, 5(12): 891-896.
- Karafillis, A.P. and Boyce, M.C., 1993. A general anisotropic yield criterion using bounds and a transformation weighting tensor. *Journal of the Mechanics and Physics of Solids*, 41(12): 1859-1886.
- Khan, A.S. and Huang, S., 1995. *Continuum Theory of Plasticity*. Wiley.
- Lapovok, R.Y., Barnett, M.R. and Davies, C.H.J., 2004. Construction of extrusion limit diagram for AZ31 magnesium alloy by FE simulation. *Journal of Materials Processing Technology*, 146(3): 408-414.
- Lebensohn, R.A. and Tomè, C.N., 1993. A self-consistent anisotropic approach for the simulation of plastic deformation and texture development of polycrystals: application to zirconium alloys, 41, p., 1993. *Acta Metallurgica et Materialia*, 41(9): 2611-2624.
- Lee, B.H., Reddy, N.S., Yeom, J.T. and Lee, C.S., 2007. Flow softening behavior during high temperature deformation of AZ31Mg alloy. *Journal of Materials Processing Technology*, 187-188: 766-769.
- Letzig, D., Swiostek, J., Bohlen, J., Beaven, P. and Kainer, K.U., 2008. Wrought magnesium alloys for structural applications. *Mat. Sci. Techn.*, 24(8): 991-996.
- Li, L., Zhou, J. and Duszczuk, J., 2006. Determination of a constitutive relationship for AZ31B magnesium alloy and validation through comparison between simulated and real extrusion. *Journal of Materials Processing Technology*, 172(3): 372-380.
- Liu, G., Zhou, J. and Duszczuk, J., 2007. Prediction and verification of temperature evolution as a function of ram speed during the extrusion of AZ31 alloy into a rectangular section. *Journal of Materials Processing Technology*, 186(1-3): 191-199.
- Liu, J., Cui, Z. and Li, C., 2008. Modelling of flow stress characterizing dynamic recrystallization for magnesium alloy AZ31B. *Computational Materials Science*, 41(3): 375-382.
- Lof, J., 2001. Elasto-viscoplastic FEM simulations of the aluminium flow in the bearing area for extrusion of thin-walled sections. *Journal of Materials Processing Technology*, 114: 174-183.
- Ottosen, N.S. and Ristinmaa, M., 2005. *The Mechanics of Constitutive Modeling*. Oxford Pub.
- Peirce, D., Asaro, R.J. and Needleman, A., 1983. Material rate dependence and localized deformation in crystalline solids. *Acta Metall.*, 31(12): 1951-1976.
- Polmear, I., 2006. *Light Alloys: From Traditional Alloys to Nanocrystals*. Elsevier-Butterworth Heinemann.

- Rechenberg, I. (Editor), 1994. Evolutionsstrategie '94. Werkstatt Bionik und Evolutionstechnik. Frommann-Holzboog Verlag, Stuttgart.
- Rockafellar, R.T., 1972. Convex analysis. Princeton University Press.
- Rousselier, G., 1987. Ductile fracture models and their potential in local approach of fracture. Nucl. Eng. Des., 105: 97-111.
- Schwefel, H.-P., 1977. Numerische Optimierung von Computer-Modellen mittels der Evolutionsstrategie : mit einer vergleichenden Einführung in die Hill-Climbing- und Zufallsstrategie. Interdisciplinary systems research. Birkhäuser, Basel.
- Simo, J.C. and Hughes, T.J.R., 1998. Computational Inelasticity. Springer Inc.
- Spigarelli, S. et al., 2007. Analysis of high-temperature deformation and microstructure of an AZ31 magnesium alloy: International Symposium on Physics of Materials, 2005. Materials Science and Engineering: A, 462(1-2): 197-201.
- Steinberg, D.J., Cochran, S.G. and Guinan, M.W., 1980. A constitutive model for metals applicable at high-strain rate. J. Appl. Phys., 51(3): 1498–1504.
- Steinberg, D.J. and Lund, C.M., 1989. A constitutive model for strain rates from 0.0001 to 1000000/s. J. Appl. Phys., 65(4): 1528–1533.
- Tresca, H., 1864. Mémoire sur l'écoulement des corps solides soumis à de fortes pressions. C.R. Acad. Sci. Paris, 59: 754-758.
- Tvergaard, V. and Needleman, A., 1984. Analysis of the cup-cone fracture in a round tensile bar. Acta Metall., 32(1): 157-169.
- von Mises, R., 1928. Mechanik der plastischen Formänderung von Kristallen. ZAMM, 8(3): 161-185.
- Wagoner, R.H. and Chenot, J.-L., 2001. Metal Forming Analysis. Cambridge University Press.
- Yoo, M.H., 1981. Slip, twinning, and fracture in hexagonal close-packed metals. Metall. Trans. A, 12A: 409-418.
- Zener, C. and Hollomon, J.H., 1944. Effect of strain rate upon the plastic flow of steel J. Appl. Phys., 15: 22-27.
- Zhang, Y., Zeng, X., Lu, C. and Ding, W., 2006. Deformation behavior and dynamic recrystallization of a Mg-Zn-Y-Zr alloy. Materials Science and Engineering: A, 428(1-2): 91-97.

Appendix

A.1. Header of VUMAT interface

```
      subroutine VUMAT (  
C Read only variables  
      *      nblock, ndir, nshr, nstatev, nfieldv, nprops, lanneal,  
      *      stepTime, totalTime, dt, cmname, coordMp, charLength,  
      *      props, density, strainInc, relSpinInc,  
      *      tempOld, stretchOld, defgradOld, fieldOld,  
      *      stressOld, stateOld, enerInternOld, enerInelasOld,  
      *      tempNew, stretchNew, defgradNew, fieldNew,  
C Write only variables  
      *      stressNew, stateNew, enerInternNew, enerInelasNew )  
C  
      include 'vaba_param.inc'  
C  
      dimension coordMp(nblock,*), charLength(nblock), props(nprops),  
1      density(nblock), strainInc(nblock,ndir+nshr),  
2      relSpinInc(nblock,nshr), tempOld(nblock),  
3      stretchOld(nblock,ndir+nshr),  
4      defgradOld(nblock,ndir+nshr+nshr),  
5      fieldOld(nblock,nfieldv), stressOld(nblock,ndir+nshr),  
6      stateOld(nblock,nstatev), enerInternOld(nblock),  
7      enerInelasOld(nblock), tempNew(nblock),  
8      stretchNew(nblock,ndir+nshr),  
9      defgradNew(nblock,ndir+nshr+nshr),  
1     fieldNew(nblock,nfieldv),  
2     stressNew(nblock,ndir+nshr), stateNew(nblock,nstatev),  
3     enerInternNew(nblock), enerInelasNew(nblock),  
      character*80 cmname  
C  
      do 100 k=1, nblock  
        user coding  
100 continue  
      return  
      end
```

A.2. Variables used in VUMAT and their descriptions

VUMAT Variables	Short descriptions
ndir	General information
nshr	
nblock	
nstatev	
nprops	
nfieldv	
props (nprops)	
coordMP (nblock, *)	
charLength (nblock)	
stressNew (nblock, ndir+nshr)	
stressOld (nblock, ndir+nshr)	
stateNew (nblock, nstatev)	State variables
stateOld (nblock, nstatev)	
fieldNew (nblock, nfieldv)	User defined field variables
fieldOld (nblock, nfieldv)	
enerInternNew (nblock)	Internal energy
enerInternOld (nblock)	
enerInelasNew (nblock)	Dissipated inelastic energy
enerInelasOld (nblock)	
strainInc (nblock, ndir+nshr)	Strain tensor
tempNew (nblock)	Temperature
tempOld (nblock)	
defgradNew (nblock, ndir+2nshr)	Deformation gradient
defgradOld (nblock, ndir+2nshr)	
relSpinInc (nblock, nshr)	Rotation & stretch
stretchNew (nblock, ndir+nshr)	
stretchOld (nblock, ndir+nshr)	
stepTime	Time
totalTime	
dt	

Acknowledgments

The thesis work has been carried out during my stay in GKSS Research Centre, Geesthacht. The project has been realised as a cooperation of the departments of Simulation of Solids and Structures (WMS) and Wrought Magnesium Alloys (WZW) at GKSS Research Centre.

I would like to express my deepest gratitude to Prof. Wolfgang Brocks without whose guidance and supervision this thesis would not have been possible.

I like to extend my kind gratefulness to Dr. Dirk Steglich for his spectacular support, continuous motivation and brilliant suggestions, which definitely improved the quality of this work.

Special thanks to Dr. Jan Bohlen for his excellent support and constructive discussions on experimental issues. Appreciation is also extended to Dr. Dietmar Letzig for his invaluable comments.

I wish to express my gratefulness to Dr. Sören Müller and Dr. Hans-Michael Mayer from Technische Universität Berlin for their technical supports on mechanical testing and extrusion experiments.

I wish to thank also Mr. Mintesnot Nebebe for his productive ideas and discussions, especially on the optimisation algorithm.

Furthermore, I would like to extend my thanks to Dr. Ingo Scheider, Prof. Jörn Mosler and Mr. Malek Homayonifar who always kept their doors open for any kind of suggestions and constructive ideas.

I would like to thank the ex- and current staff of WMS and WZW for being friendly and their moral support during my stay in GKSS Research Centre.

I greatly acknowledge the financial support of the German Research Foundation (DFG).

Last, but not least, I am very grateful to my family and my friends for their encouragement and support, which motivated me during the thesis.

Serkan Ertürk

Geesthacht, June 2009

Curriculum Vitae

Personal Data:

Name	Serkan Ertürk
Date - place of birth	03.04.1980, Ankara, Turkey
Citizenship	Turkish
Address	Schiller Str. 49, D-21502, Geesthacht, Germany

Experiences:

(06.2006 – present)	Doctoral Scientific Assistant (*) , Department of Simulation of Solids and Structures and Department of Wrought Magnesium Alloys , GKSS Research Centre, Geesthacht, Germany
(09.2005 – 05.2006)	Project-employee (**) , Chair of Mechanics , Department of Mechanical Engineering, University of Dortmund, Dortmund, Germany
(05.2005 – 09.2005)	M.Sc. Student , Department of Simulation of Solids and Structures , GKSS Research Centre, Geesthacht, Germany
(10.2004 – 04.2005)	Teaching Assistant , Centre of Material Analysis , Faculty of Engineering, Christian-Albrechts-University of Kiel, Kiel, Germany
(10.2003 – 04.2005)	Research Assistant , Chair of General Materials Science , Faculty of Engineering, Christian-Albrechts-University of Kiel, Kiel, Germany

Education:

(2003 – 2005)	M.Sc. Degree (***) Department of Material Science and Engineering , Christian-Albrechts-University of Kiel, Kiel, Germany <i>CGPA of 1.4 / 5.0 (German Grading System - 1.0 is the best)</i>
(2002 – 2005)	Distance Education (****) Department of Business Administration, Anadolu University , Eskisehir, Turkey
(2001 – 2003)	Minor – B.Sc. Degree (***) Department of Mechanical Engineering , Middle East Technical University, Ankara, Turkey <i>CGPA of 2.75 / 4.00 (US Grading System - 4.00 is the best)</i>
(1999 – 2003)	Major – B.Sc. Degree (***) Department of Metallurgical and Materials Engineering , Middle East Technical University, Ankara, Turkey <i>CGPA of 3.33 / 4.00 (US Grading System - 4.00 is the best)</i>

(*): supported by German Research Foundation (DFG)

(**): scholarship awarded by Federal State of North Rhine-Westphalia, Germany

(***): curriculum taught in English

(****): could not be finished due to being in Germany